



HAL
open science

A Numerical Model to Predict Train Induced Vibrations and Dynamic Overloads

Riccardo Ferrara

► **To cite this version:**

Riccardo Ferrara. A Numerical Model to Predict Train Induced Vibrations and Dynamic Overloads. Mechanical engineering [physics.class-ph]. Université Montpellier II - Sciences et Techniques du Languedoc; Università degli studi mediterranea (Reggio de Calabre, Italie), 2013. English. NNT : 2013MON20101 . tel-00842993v2

HAL Id: tel-00842993

<https://theses.hal.science/tel-00842993v2>

Submitted on 10 Jul 2014

HAL is a multi-disciplinary open access archive for the deposit and dissemination of scientific research documents, whether they are published or not. The documents may come from teaching and research institutions in France or abroad, or from public or private research centers.

L'archive ouverte pluridisciplinaire **HAL**, est destinée au dépôt et à la diffusion de documents scientifiques de niveau recherche, publiés ou non, émanant des établissements d'enseignement et de recherche français ou étrangers, des laboratoires publics ou privés.

UNIVERSITY OF REGGIO CALABRIA
DEPARTMENT OF CIVIL, ENERGY, ENVIRONMENT AND
MATERIALS ENGINEERING

Joint supervision with

UNIVERSITY MONTPELLIER 2
MECHANICAL AND CIVIL ENGINEERING LABORATORY

PhD. THESIS

Presented for the degree of Doctor of Philosophy of the University of Reggio Calabria and the University Montpellier 2

by

Riccardo Ferrara

A NUMERICAL MODEL TO PREDICT TRAIN INDUCED VIBRATIONS AND DYNAMIC OVERLOADS

Presented on May 21, 2013, to the jury:

Mr. FELICE ARENA	University of Reggio Calabria - DICEAM	(Coordinator)
Mr. FRANCK JOURDAN	University of Montpellier 2 - LMGC	(Director)
Mr. GIOVANNI LEONARDI	University of Reggio Calabria - DICEAM	(Director)
Mr. FRANCESCO MACCHIONE	University of Cosenza - UNICAL	(Examiner)
Mr. ROBERTO TOMASICCHIO	University of Salento - Lecce	(Reviewer)
Mr. ALFONSO VULCANO	University of Cosenza - UNICAL	(Reviewer)

ABSTRACT

A numerical model to predict train induced vibrations is presented. The dynamic computation considers mutual interactions in vehicle/track coupled system by means of a finite and discrete elements method. The vehicle is modeled by 7 bi-dimensional rigid elements representing: the body, the two bogies and the four wheels. The railway is discretized as finite Timoshenko beam elements. Axial deformation is assumed insignificant. The substructure is made-up of: rail-pads, sleepers, ballast, and background. Rail-pads are modeled as spring/damper couples without mass and sleepers are modeled as rigid elements. The rail-sleeper contact is assumed extended to a connection-area, rather than a single point assumption. To model this area many spring/damper couples are disposed along the length of sleepers. The ballast is modeled as blocks of mass made-up of rigid elements, connected to sleeper by spring/damper couples. To allow the transmission of vibrations in longitudinal direction too, spring/damper couples connect ballast elements horizontally. The dynamic interaction between the wheel-sets and the rail is accomplished by using the non-linear Hertzian model with hysteresis damping. The rail defects and the case of out-of-round wheels are considered too.

A modal analysis of supporting structure is done to validate the substructure model comparing it to experimental data. Comparisons between numerical results of our model, experimental data and numerical results of others literature models are done on contact-force, rail accelerations and sleepers accelerations to validate the coupled vehicle/track system. Moreover a modal analysis of the coupled vehicle/track system is done to analyse the relationship between resonance frequencies, train velocities and ballast displacements. A sensitivity analysis is done to evaluate the variables more affecting the maintenance costs. The parameters more conditioning the ballast maintenance costs are the ballast modulus and the train mass. The effects of train velocity on the ballast displacements are analysed in relationship with substructure properties.

A new formulation to evaluate the railway toll connected to ballast wear is introduced. A new interpretation of the critical velocity in the range $100 - 300 \text{ km h}^{-1}$ is proposed.

Keywords: critical speed, railway toll, contact-force, vehicle/track, sensitivity analysis, ballast settlement, receptance.

RÉSUMÉ

Ces dernières années les états membres de la communauté européenne ont entrepris une campagne dont l'objectif est le développement du réseau ferroviaire européen. Les plus grands changements induits par cette campagne sont la libéralisation du marché du trafic ferroviaire, l'interopérabilité des infrastructures et la création d'un réseau de transport transeuropéen (RTE-T). Selon la classification européenne tous les trains qui dépassent la vitesse de 250 km h^{-1} sont considérés "à grande vitesse". Durant les cinquante dernières années le développement technologique du train et des infrastructures ferroviaires ainsi que la rapide augmentation des vitesses en ligne ont provoqué une forte augmentation du besoin d'outils numériques pour la conception des infrastructures et des véhicules.

Les objectifs principaux de nos travaux sont de deux ordres. Le premier est de contribuer à faire progresser les méthodes numériques, en développant un outil rapide et simple, capable de simuler les principaux comportements physiques. Le second est d'étudier, de comprendre et de décrire deux phénomènes particuliers : la vitesse critique et le tassement du ballast.

La thèse est composée de deux parties. Dans la première partie on montre le modèle numérique adopté pour simuler le système véhicule/infrastructure. Les premiers chapitres sont dédiés, chacun, à la modélisation d'un composant du système véhicule/infrastructure : le véhicule, le rail, les attaches, les traverses et le ballast. Chaque chapitre se présente selon le schéma suivant. Au début on présente l'état de l'art des modèles utilisés pour décrire le composant introduit. Ensuite on présente les équations du mouvement pour chaque corps assemblés sous forme matricielle. Enfin on discute le choix des paramètres physiques adoptés. Un chapitre est dédié à la modélisation des défauts des roues et du rail. Enfin, le dernier chapitre de la première partie propose deux algorithmes finalisés pour résoudre les équations du mouvement.

Le véhicule est modélisé par 7 éléments rigides bi-dimensionnels représentant : La caisse, les deux bogies, et les quatre roues. La Figure 1 représente un schéma du modèle du véhicule.

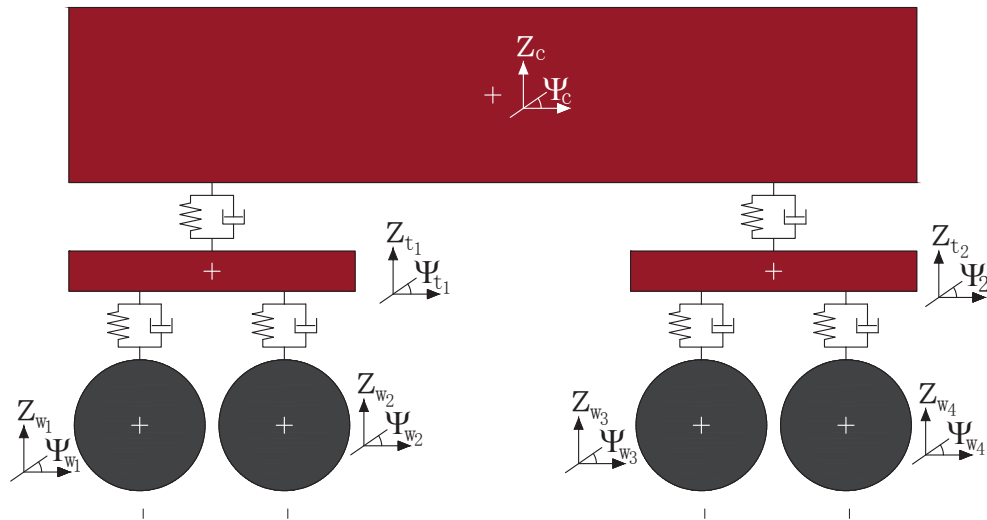


Figure 1 – *Modèle véhicule.*

Le rail est discrétisé par des éléments finis de type Timoshenko pour tenir compte des effets du cisaillement ; la déformation axiale est considérée négligeable. Des éléments à deux et à trois nœuds ont été testés numériquement en comparant les modes de vibrations avec des résultats analytiques.

Les attaches sont modélisées par des couples ressort/amortisseur sans masse et les traverses sont modélisées par des éléments rigides avec masse. À la différence des modèles présents dans la littérature, ces fixations rail/traverse sont modélisées par des contacts surfacique au lieu de contacts ponctuels. En effet, cette liaison est bien plus proche de la réalité, en permettant des configurations du rail déformé très différentes de celles du cas d'une liaison ponctuelle (Figure 2). Le ballast est modélisé par des blocs rigides

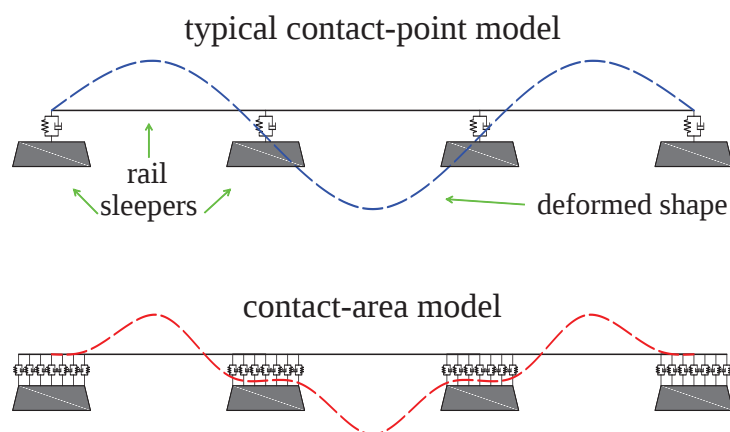


Figure 2 – *Schéma de la déformation du rail dans le cas d'une liaison rail/attache ponctuel et le cas d'une liaison répartie sur une surface de contact.*

massiques connectés aux traverses par des couples ressort/amortisseur. Les coefficients de rigidité et d'amortissement du ballast ont été évalués en considérant la partie de volume intéressée par les contraintes transmises par les traverses (Figure 3(a)). En effet

on peut prévoir, avec une bonne approximation, que les contraintes se propagent dans le milieu du ballast selon un volume trapézoïdale dont l'angle d'incidence respecte le rapport de Poisson [82]. Des couples ressort/amortisseur sont disposés horizontale-

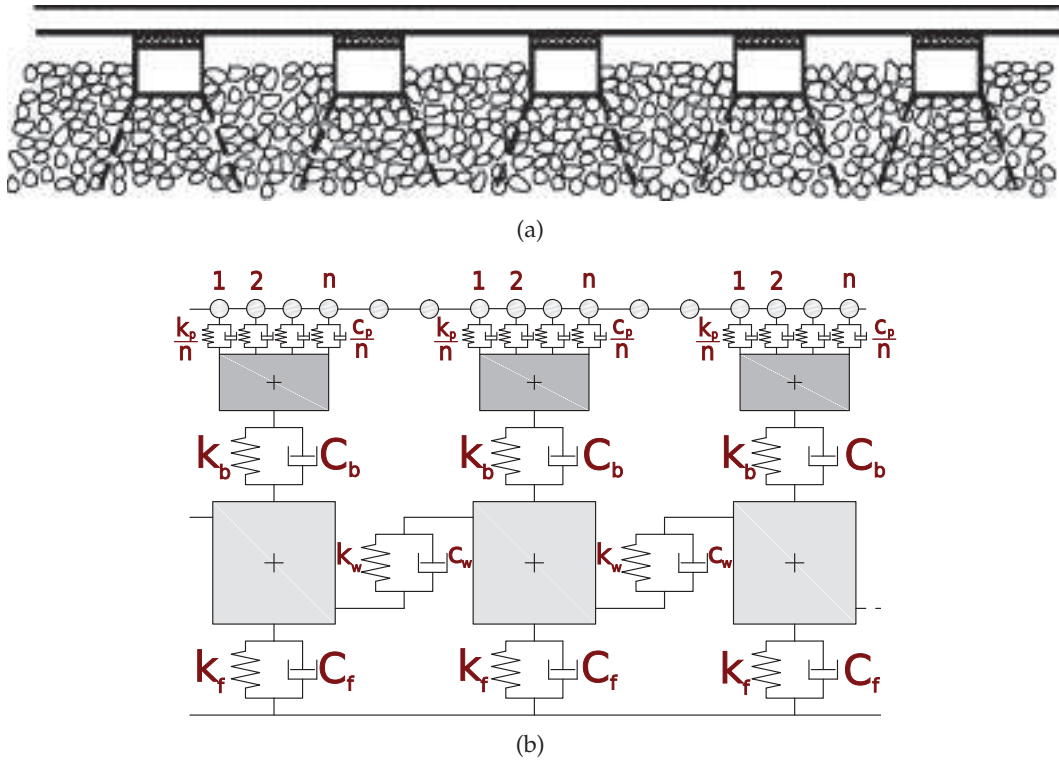


Figure 3 – L'infrastructure : (a) distribution simplifiée des contraintes dans le ballast [82] (b) représentation du modèle.

ment pour permettre aussi la transmission longitudinale des vibrations. La Figure 3(b) montre une représentation du modèle de l'infrastructure. La masse des blocs du ballast a été évalué selon le même principe en considérant un volume théorique vibrant (Figure 3(b)). Le modèle du véhicule et de l'infrastructure sont couplés par le contact

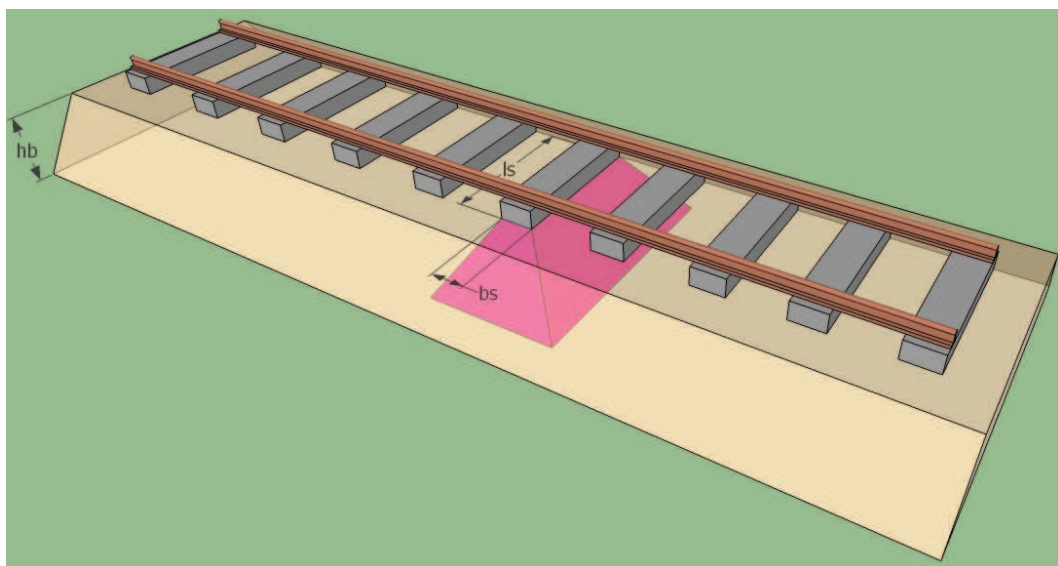


Figure 4 – Volume théorique vibrant du ballast.

roue/rail. La force de contact est modélisée par la théorie non linéaire de Hertz avec un amortisseur à hystérésis.

Pour tenir compte des irrégularités de la surface de contact du rail et des roues, causés par l'usure due au frottement présent à l'interface, des "fonctions défauts" sont implémenté dans le modèle. Trois modèles différents sont utilisés selon les cas étudiés. Le premier est celui indiqué par la norme *EN ISO 3095 : 2004 standard*. L'Organisation International pour la Standardisation reporte le spectre des fréquences des irrégularités du rail. En partant du spectre des fréquences le profil du rail est évalué en 1/3 des bandes d'octave en discrétisant chaque bande par 50 longueurs d'ondes. Le second modèle, utilisé par l'Association Ferroviaire Américain *AAR (Association of American Railways)*, permet de simuler le vieillissement de l'infrastructure en variant le degré d'intensité des irrégularités. Le troisième modèle consiste à construire une fonction de défaut équivalente appliqué au rail pour simuler la variation de forme du profil de roues due aux freinages brusques.

Les innovations fondamentales introduites dans cette première partie de la thèse résident dans le modèle de liaison entre les attaches et le rail, et dans le nouvel algorithme proposé pour résoudre la non linéarité du problème. En effet la distance entre deux traverses varie entre 60 et 70 cm ; la longueur d'une attache, mesurée dans la direction du rail, varie entre 17 et 26 cm. Si on compare ces deux longueurs entre elles, on peut constater que la modélisation de cette liaison avec un point de contact se révèle excessive. L'étude des fréquences naturelles de l'infrastructure, présentée dans la deuxième partie de cette thèse, révèle l'importance de cette hypothèse en montrant que les amplitudes de la première fréquence naturelle, déterminées dans le cas du modèle de liaison ponctuelle, amènent des importants erreurs d'estimation. En effet dans le cas d'excitation du rail à mi-portée (entre deux traverses) l'amplitude est surestimée de 400% ; et dans le cas d'excitation du rail en correspondance d'une traverse l'amplitude est sous-estimée de 150% (Figures 5 et 6).

La deuxième innovation consiste dans l'algorithme de résolution proposé pour résoudre les équations du mouvement. Le problème consiste à résoudre les deux systèmes des équations : un pour le véhicule et l'autre pour l'infrastructure. Ces deux systèmes d'équations sont couplés par les forces de contact roue/rail. En effet la force de contact est à la fois dépendante des déplacements des roues et des nœuds du rail. Le problème est non linéaire à cause du modèle Hertzien utilisé pour évaluer la force de contact. La méthode du point fixe a été utilisée pour coupler les deux systèmes entre eux. Pour chaque pas de temps les itérations de la méthode du point fixe consistent à fixer les déplacements du véhicule et à résoudre le système associé à l'infrastructure en calculant la force de contact avec les valeurs de déplacements de l'infrastructure calculées dans l'itération précédente ; Ensuite, dans le même pas de temps, les déplacements de l'infrastructure sont fixés et le système associé au véhicule est résolu jusqu'à la convergence de la solution. Afin de rendre plus rapide la résolution, la méthode du point fixe a été couplée avec la méthode de Newton Raphson. En effet la résolution du système associé au véhicule est faite en considérant la partie de la non-linéarité de la force de contact liée aux déplacements des roues et le système est résolu avec la méthode de Newton Raphson. De cette manière la partie de la non-linéarité associé au véhicule est résolue pour chaque itération de point fixe et le nombre total d'itérations de point fixe est réduit. Enfin la méthode de Newton Raphson est appliquée uniquement au système des 10 équations du véhicule. De cette façon la factorisation et la résolution du système des équations du mouvement sont des opérations qui occupent un temps tout à fait négligeable comparés aux avantages apportés.

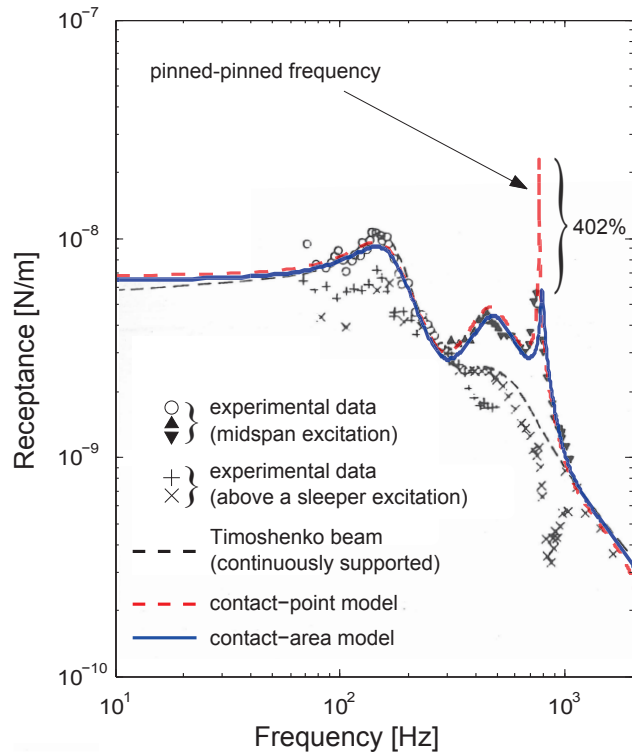


Figure 5 – Comparaison des analyses modales de l'infrastructure évaluées dans le cas de : contact ponctuel, contact surfacique et résultats expérimentaux [42] ; excitation à mi-portée de l'entraxe entre deux traverses.

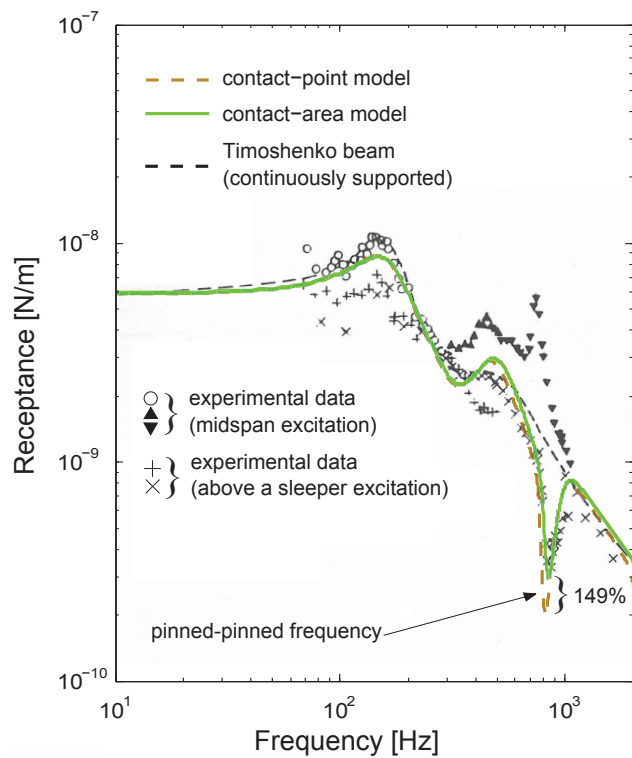


Figure 6 – Comparaison des analyses modales de l'infrastructure évaluées dans le cas de : contact ponctuel, contact surfacique et résultats expérimentaux [42] ; excitation en correspondance d'une traverse.

La deuxième partie de la thèse est consacrée à la présentation des résultats numériques obtenus. Le comportement du modèle a été testé en trois étapes. Dans la première étape l'infrastructure a été excitée par une force impulsive. Ce procédé a permis la calibration des paramètres du modèle et la correction des erreurs présentes dans le logiciel. Généralement l'analyse modale représente l'outil utilisé dans la littérature scientifique pour valider les modèles de l'infrastructure. Nos analyses ont été comparées avec des résultats expérimentaux et d'autres modèles numériques. Les Figures 5 et 6 montrent que le modèle de contact surfacique est bien plus proche des résultats expérimentaux que le modèle de contact ponctuel. Dans la deuxième étape le véhicule a été ajouté au modèle. Des simulations ont été effectuées pour étudier les accélérations des traverses et du rail générées par le passage d'une locomotive. En comparant les résultats numériques avec ceux expérimentaux, cette étape a permis la calibration : des irrégularités de surface, du modèle du véhicule, et de la méthode de couplage véhicule/infrastructure. Pendant cette étape l'efficacité et la précision du modèle ont été évaluées. Dans la troisième étape une analyse de sensibilité du modèle a été menée. Les paramètres de contrôle choisis pour réaliser l'analyse sont le coefficient d'amplification dynamique δ_{dyn} et la déflexion élastique d'une traverse z_{sl} . Les Figures 7 et 8 montrent les résultats de l'analyse.

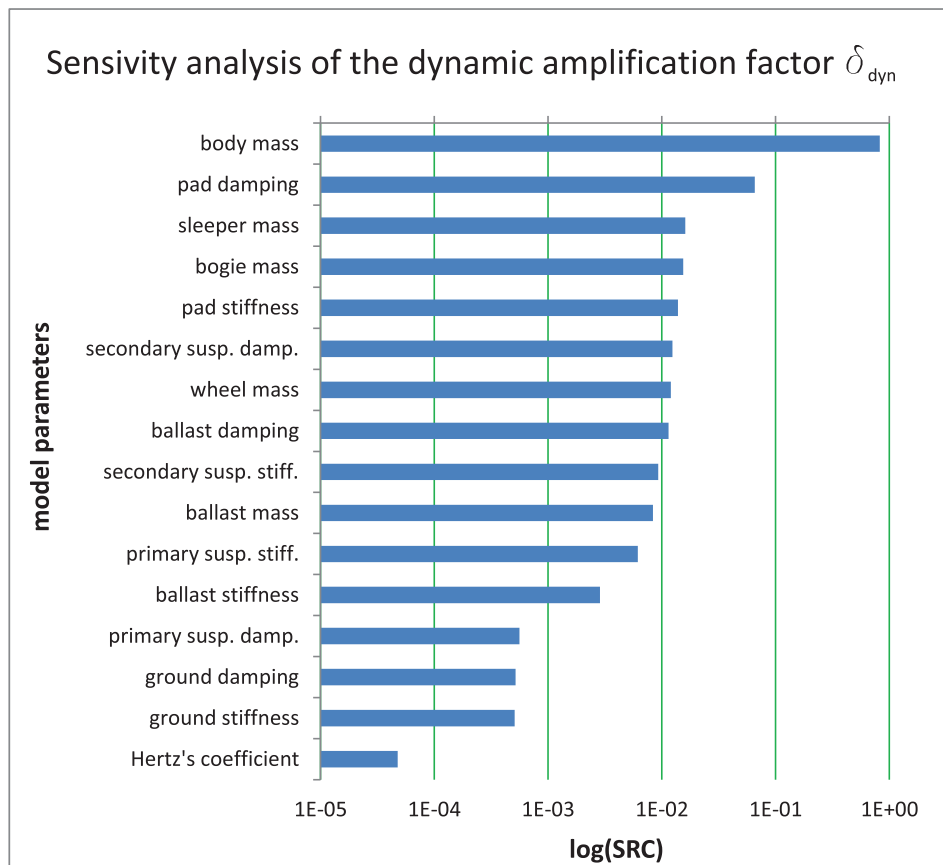


Figure 7 – Analyse de sensibilité pour le coefficient d'amplification dynamique.

Pendant cette dernière étape, les résultats des simulations ont été utilisés pour la compréhension et la description de l'origine de la vitesse critique et des effets du train sur le tassement du ballast.

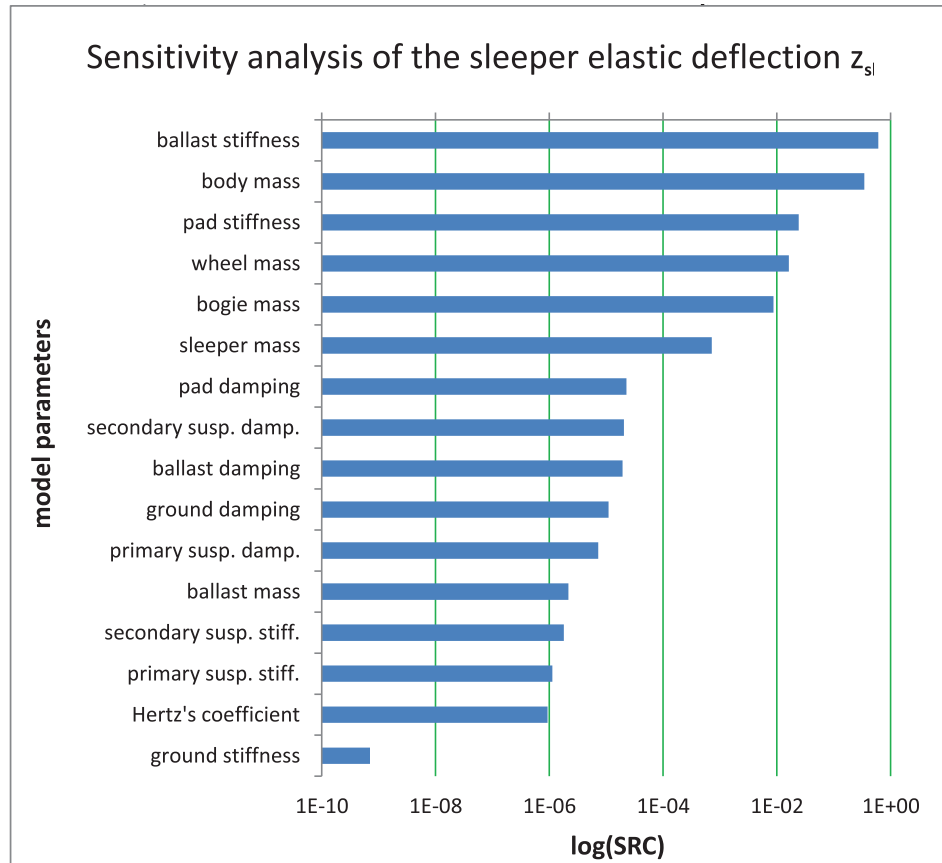


Figure 8 – Analyse de sensibilité pour la déflexion d'une traverse.

La vitesse critique peut être définie comme une certaine valeur de vitesse que provoque un fort incrément des vibrations et des déplacements verticaux et latéraux de l'infrastructure. Pour les valeurs de vitesses plus grandes ou plus petites que cette valeur critique, les effets sont mineurs. Ce phénomène a été étudié par plusieurs équipes [69, 43, 31, 19, 57] et a été attribué à un effet de résonance comparable au phénomène aérodynamique du mur du son : "Mach effect". Quand un mobile atteint la vitesse du son dans un fluide, il se produit un phénomène de concentration de l'onde de surpression qui provoque une onde de choc. Cet effet se produit car le mobile rejoint les vagues sonores qu'il produit lui-même. De la même façon le train produit des vagues de déformation sur l'infrastructure. La vitesse de ces vagues, nommé "vitesse de Rayleigh", dépend principalement des caractéristiques du ballast et du sol. Quand le train rejoint la vitesse des vagues de déformation qu'il produit, une amplification des vibrations apparaît. Les études s'accordent sur l'existence de deux vitesses critiques. La première peut être assimilée à la vitesse de Rayleigh du sol, la deuxième, assez proche de la première, est influencée par la rigidité flexionnelle et par la masse du système rail/talus. Des observations et des résultats expérimentaux [53, 70, 61, 30] ont confirmé ce phénomène dans l'intervalle des vitesses $100 - 300 \text{ km h}^{-1}$. Plusieurs méthodes ont été développées afin de prévoir la réponse de l'infrastructure aux passages des trains roulant à la vitesse critique : Fonction de Green [43, 74, 75], vaguelette [46], éléments finis de frontière et éléments finis classiques, même avec des maillages adaptatifs qui bougent avec le train [21]. Dimitrovová and Varandas [19] ont estimé la vitesse critique, pour quatre différents types de sols, appartenir à un intervalle entre 702 et 1200 km h^{-1} . En effet la vitesse des vagues de Rayleigh estimée pour des sols

typiques dans le domaine des infrastructures ferroviaires dépasse les 500 km h^{-1} , soit une vitesse bien supérieure aux vitesses typiques adoptées en ligne (maximum environ 350 km h^{-1}). Ainsi le phénomène étudié en correspondance de ces vitesses n'a qui un intérêt de type académique. En effet même si l'effet "Mach" est physiquement plausible pour ces conditions, les trains n'atteignent pas, pour le moment, ces vitesses. De plus, même en présence de sols très flexibles comme des couches de tourbe, où la vitesse de Rayleigh est dans l'intervalle $320 - 400 \text{ km h}^{-1}$, des résultats expérimentaux ont permis l'observation du phénomène de la vitesse critique pour des trains roulant à la vitesse de 135 km h^{-1} (nombre Mach proche à 0.4). Donc, pour le moment, il n'y a ni estimation exacte ni explication physique de la vitesse critique dans l'intervalle inférieur à la vitesse de Rayleigh.

Dans cette thèse une nouvelle explication a été proposée. La cause majeure d'excitation de la force de contact est la variation de rigidité due à la présence des traverses. La distance entre deux traverses (environ 0.65 m) peut donc être assimilée à la longueur d'onde de la fonction d'excitation. Cette considération lie la vitesse du train à la fréquence d'excitation :

$$V = 3.6 \cdot 0.65 \cdot f \text{ [km h}^{-1}\text{]}, \quad (1)$$

avec la fréquence f exprimés en Hz. Plusieurs auteurs ont mis en relation les fréquences naturelles de l'infrastructure avec la vitesse du train. En réalité la masse du train et les suspensions ont une influence non négligeable qui modifie la réponse du système en termes de modes de vibration. Pour cette raison, il est nécessaire de lier les fréquences d'excitation, et donc la vitesse du train (Équation 1), avec les modes de vibration du système couplé véhicule/infrastructure. Des comparaisons entre les analyses modales du système couplé et la déflexion de la traverse en fonction de la vitesse du train ont été menées.

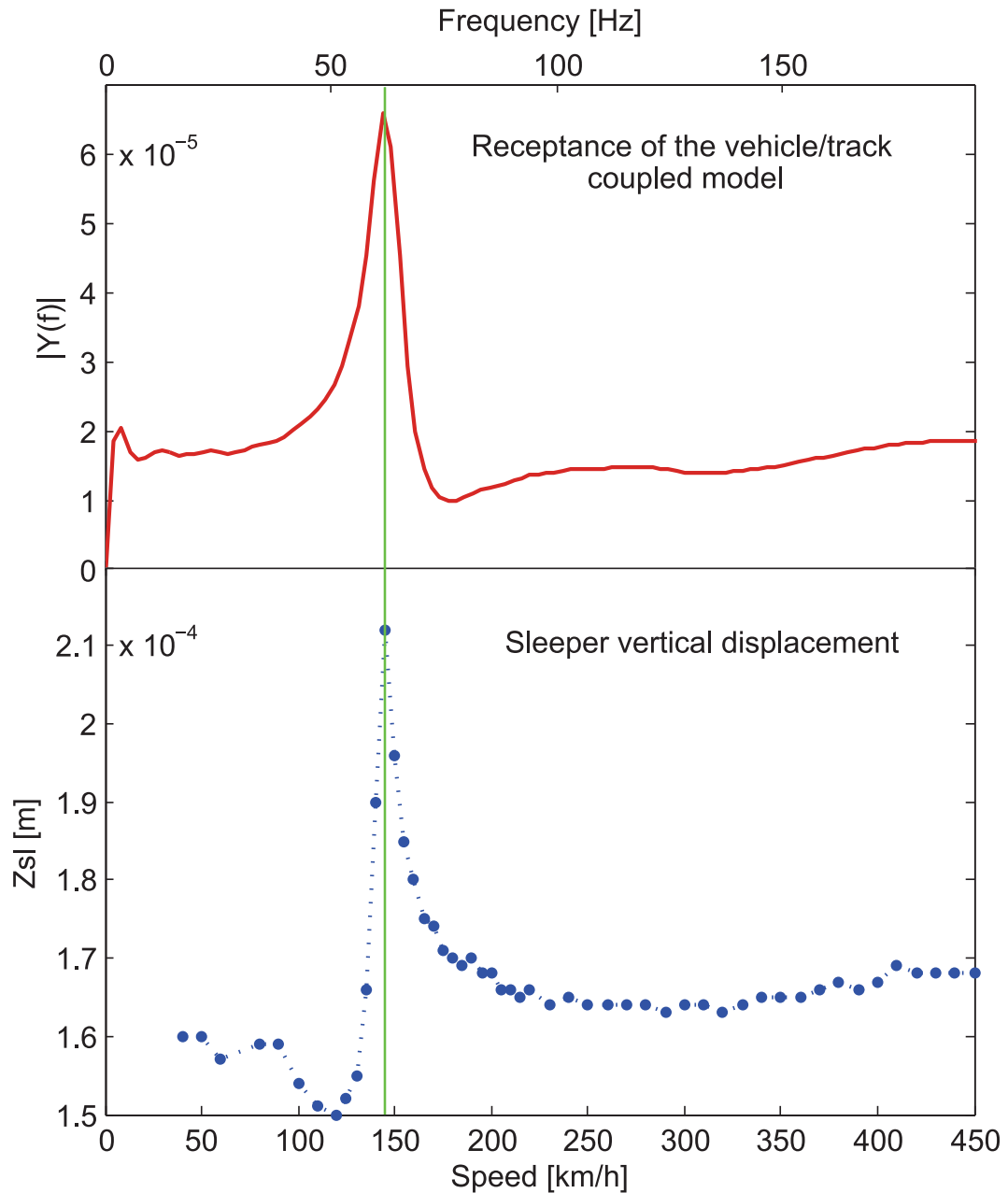


Figure 9 – Comparaison entre la analyse modale du système couplé et la déflexion de la traverse en fonction de la vitesse du train

La Figure 9 montre un des résultats de cette comparaison. Le système couplé véhicule/infrastructure présente un mode de vibration très prononcé en correspondance d'environ 60 Hz. Lorsque la vitesse du train, qui excite le système suite au passage des traverses, rejoint la valeur critique d'environ 150 km h^{-1} , un phénomène de résonance s'observe. En conséquence les études sur la vitesse critique ne peuvent pas être menées en analysant seulement les caractéristiques de l'infrastructure en le considérant isolé, mais il est nécessaire de tenir compte du système couplé avec le véhicule. De plus, cette étude donne une explication aux phénomènes des vitesses critiques trouvés expérimentalement dans l'intervalle ($100\text{--}300 \text{ km h}^{-1}$) et qui ne peut pas être interprété par la théorie de "Mach-Rayleigh".

La deuxième étude développée concerne les coûts des entretiens liés au tassement du ballast. Le but est de trouver une fonction de coûts liés aux caractéristiques et aux variables du véhicule, et de proposer une nouvelle méthode pour calculer la partie du péage ferroviaire lié au tassement du ballast (50 % environ du coût total). Plusieurs auteurs [14, 27] ont trouvé une relation de linéarité entre le tassement du ballast et le nombre de cycle de charge (nombre de passages des axes du véhicule). Il se trouve aussi que le coefficient angulaire de cette relation est une fonction exponentielle de la déflexion subit par le ballast pour chaque cycle de charge. En conséquence, en calculant la déflexion du ballast grâce au modèle présenté dans cette thèse, il est possible d'évaluer l'effet de chaque véhicule sur le tassement. Une fois calculé le coût total d'un certain

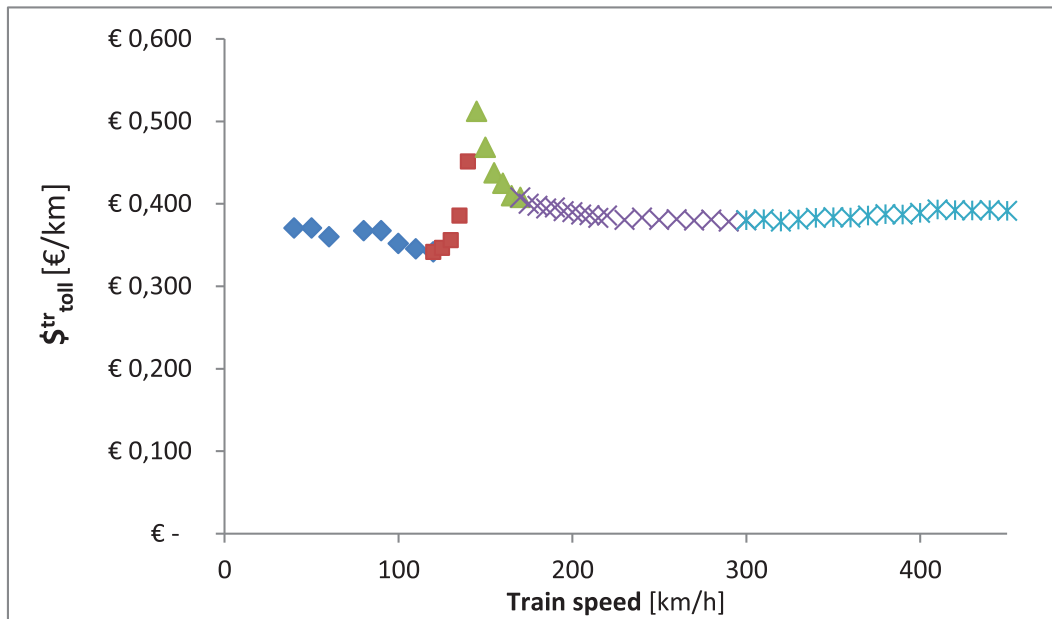


Figure 10 – Coût du tassement en fonction de la vitesse du véhicule.

type de ligne, lié à un certain seuil d'intervention (somme des interventions des bourrages plus la substitution totale du ballast), il est possible d'évaluer le coût de chaque passage de train et de le lier à toutes les variables du modèle. La Figure 10 montre le coût du passage d'une locomotive en fonction de sa vitesse.

CONTENTS

CONTENTS	xvii
LIST OF FIGURES	xvii
1 INTRODUCTION	1
1.1 INTRODUCTION	1
1.2 LITERATURE REVIEW	2
1.2.1 The vehicle/track models	2
1.2.2 The ballast settlement models	3
1.2.3 The critical speed phenomenon	3
1.3 THE PLAN OF THE THESIS	4
I The Numerical Model	5
2 THE VEHICLE MODEL	9
2.1 THE MODEL	9
2.2 ASSEMBLED MOTION EQUATIONS FOR THE VEHICLE MODEL	9
2.3 THE MANCHESTER BENCHMARK	12
2.4 THE WHEEL-RAIL CONTACT MODEL	13
3 THE RAIL MODEL	15
3.1 SOME OTHER MODELS	15
3.2 THE REASONS WHY A NEW RAIL MODEL IS PROPOSED	16
3.3 THE NEW PROPOSED RAIL MODEL	17
3.3.1 The stiffness and mass matrices for the two node Timoshenko element:	18
3.3.2 The stiffness and mass matrices for the three node Timoshenko element:	21
3.3.3 The damping matrix	23
3.3.4 The equivalent element nodal forces	24
3.4 ASSEMBLED MOTION EQUATIONS FOR THE RAIL MODEL	25
3.5 A TEST OF THE RAIL MODEL	27
3.6 THE RAIL PARAMETERS	30
4 THE RAIL-PADS, SLEEPERS AND BALLAST MODEL	33
4.1 INTRODUCTION	33
4.2 THE RAIL-PADS MODEL	33
4.2.1 The rail-pad parameters	33
4.3 THE BALLAST MODEL	34
4.3.1 The ballast parameters	36
4.4 ASSEMBLED MOTION EQUATIONS FOR THE SUBSTRUCTURE	37
5 THE RAIL CORRUGATION	41

5.1	INTRODUCTION	41
5.2	THE <i>ISO</i> 3095 MODEL	41
5.3	THE AMERICA RAILWAY STANDARD MODEL	43
5.4	THE RAIL EQUIVALENT CORRUGATION IN THE CASE OF OUT-OF-ROUND WHEELS	44
6	SOLVING EQUATIONS	47
6.1	INTRODUCTION	47
6.2	THE DISCRETIZATION	47
6.3	FIRST METHOD OF RESOLUTION	48
6.3.1	The Newton-Raphson method	48
6.3.2	The derivation of the R matrix components to evaluate the Jacobian . .	49
6.3.3	Computational time-costs	50
6.4	SECOND METHOD OF RESOLUTION	51
6.4.1	Combination of Newton and Fixed point methods	51
6.4.2	The derivation of the R matrix components to evaluate the Jacobian . .	51
6.4.3	Computational time-costs	53
II	The Results	57
7	THE ANALYSIS OF TRACK RECEPTANCE	61
7.1	INTRODUCTION	61
7.2	THE CURVE FITTING	62
7.3	THE IMPORTANCE OF THE CONNECTION-AREA MODEL	64
8	SIMULATIONS WITH MOVING TRAIN	67
8.1	THE SCENARIOS STUDIED	67
8.2	CASE 1 - CORRUGATED RAIL (AMERICAN RAILWAY STANDARD [45]) - COMPARISON WITH EXPERIMENTAL RESULTS	67
8.3	CASE 2: OUT-OF-ROUND WHEELS - COMPARISON WITH EXPERIMENTAL RESULTS AND OTHER NUMERICAL MODELS	69
8.4	CASE 3: CORRUGATED RAIL (<i>ISO</i> 3095 [15]) - COMPARISON WITH OTHER NUMERICAL MODELS	73
9	THE SENSITIVITY ANALYSIS	77
9.1	INTRODUCTION	77
9.2	THE INPUT VARIABLES	77
9.3	THE OUTPUT PARAMETERS	78
9.4	THE OFAT METHOD	79
9.5	THE RESULTS	80
9.6	THE INFLUENCE OF TRAIN SPEED ON SLEEPER ELASTIC DEFLECTION AND DYNAMIC AMPLIFICATION FACTOR	83
10	A NEW FORMULATION TO EVALUATE THE RAILWAY TOLLS	87
10.1	INTRODUCTION	87
10.2	THE ITALIAN SCENARIO	87
10.3	THE BALLAST SETTLEMENT PHENOMENON	92
10.4	THE COST OF SETTLEMENT: A NEW FORMULATION FOR THE RAILWAY TOLL	94
11	A RECEPTANCE ANALYSIS FOR THE COUPLED VEHICLE/TRACK SYSTEM	99

11.1	INTRODUCTION	99
11.2	TRAIN AT THE CENTER OF TRACK	99
11.3	THIRD WHEEL AT THE CENTER OF TRACK	102
11.3.1	Scenario 1	104
11.3.2	Scenario 2	105
11.3.3	Scenario 3	106
11.3.4	Scenario 4	107
11.4	CONCLUSIONS	108
12	A NEW POSSIBLE EXPLANATION OF THE CRITICAL SPEED PHENOMENON	109
12.1	INTRODUCTION	109
12.2	THE PHENOMENON	109
12.2.1	A new explanation of the critical speed	115
	Conclusions	121
	Annexes	123
A	ANNEXES	123
A.1	THE ONE THIRD OCTAVE BAND	125
A.2	BALLAST INTERVENTIONS TYPE	126
	BIBLIOGRAPHY	129

LIST OF FIGURES

1	Modèle véhicule.	viii
2	Schéma de la déformation du rail dans le cas d'une liaison rail/attache ponctuel et le cas d'une liaison répandue sur un surface de contact.	viii
3	L'infrastructure : (a) distribution simplifiée des contraintes dans le ballast [82] (b) représentation du modèle.	ix
4	Volume théorique vibrant du ballast.	ix
5	Comparaison des analyses modales de l'infrastructure évaluées dans le cas de : contact ponctuel, contact surfacique et résultats expérimentaux [42] ; excitation à mi-portée de l'entraxe entre deux traverses.	xi
6	Comparaison des analyses modales de l'infrastructure évaluées dans le cas de : contact ponctuel, contact surfacique et résultats expérimentaux [42] ; excitation en correspondance d'une traverse.	xi
7	Analyse de sensibilité pour le coefficient d'amplification dynamique.	xii
8	Analyse de sensibilité pour la déflexion d'une traverse.	xiii
9	Comparaison entre la analyse modale du système couplé et la déflexion de la traverse en fonction de la vitesse du train	xv
10	Coût du tassement en fonction de la vitesse du véhicule.	xvi

2.1	A draft of the vehicle model	10
2.2	A draft of suspension types	13
3.1	timoshenko beam model of the rail [80]	15
3.2	Generalised beam element for the track structure [45]	16
3.3	Draft of rail deformed shape in the case of the connection-point model and connection-area model.	17
3.4	Local shape functions for 3-node element [72]	21
3.5	Scheme of forces applied on a beam.	24
3.6	The four type of stiffness matrices for the rail	25
3.7	Cantilever beam and its transversal section	27
3.8	first six modes shapes of a cantilever beam	30
3.9	A section of the rail type 60E1 [3]	31
4.1	[38] Rail pad specimens: (a) HDPE classic and (b) studded.	34
4.2	A draft of rail pad model	34
4.3	The substructure: (a) load distribution region in continuous granular ballast [82] (b) a draft of the substructure model.	35
4.4	Theoretical vibrating ballast region.	35
4.5	The 3D load distribution region under a sleeper.	37
5.1	Limit spectrum of rail roughness given by <i>EN ISO 3095 : 2004 standard</i>	42
5.2	Rolling of a wheel with an idealized flat [77].	44
5.3	Difference between center and contact point position [77].	45
5.4	Wheel flat geometry from equation 5.13, $r = 460\text{mm}$ $d = 2, 15\text{mm}$ and $l = 150\text{mm}$; continuous line: irregularity on the railhead, dashed line: wheel center trajectory.	45
6.1	Algorithm of resolution.	52
6.2	Computational time for a generic simulation.	54
6.3	Computational time of simulations at varying the total number of DOF.	54
6.4	Interface of the software.	55
7.1	receptance simulation: midspan excitation	61
7.2	receptance simulation: on-sleeper excitation	62
7.3	receptance experience with the impact hammer: on-sleeper excitation [18]	62
7.4	The influence of the more important parameters to the receptance chart	63
7.5	Comparison between receptances of the railway in the case of: the connection-point model, the connection-area model and experimental data [42]; case of midspan excitation.	65
7.6	Comparison between receptances of the railway in the case of: the connection-point model, the connection-area model and experimental data [42]; case of on-sleeper excitation.	65
7.7	Waves propagation in time and in space due to a midspan excitation.	66
8.1	A picture of a ALN668 Locomotive at the Train Station	68
8.2	Comparison between: (a) experimental data [25] and (b) numerical results of the rail vertical acceleration in the case 1.	69
8.3	Comparison between: (a) experimental data [25] and (b) numerical results of the sleeper vertical acceleration in the first case.	70
8.4	Comparison between experimental data [80] and numerical results for the case 2: (a) not including rail defects; (b) including rail defects.	71

8.5	Numerical results of: (a) Sun and Dhanasekar[80]; (b) Fermer and Nielsen[22].	72
8.6	Comparison between A. Johansson and J.C.O. Nielsen [36] model and the proposed one in case of ISO3095 [15] based corrugation.	74
9.1	Variational range of each input variable.	78
9.2	An example for the determination of the average dynamic amplification factor.	79
9.3	Standard regression coefficients of input variables sorted by parts.	80
9.4	Standard regression coefficients of input variables sorted by type.	80
9.5	Sensitivity analysis of: (a) the dynamic amplification factor; (b) the sleeper elastic deflection.	81
9.6	Standard regression coefficients of input variables for the dynamic amplification factor ordered by importance.	82
9.7	Standard regression coefficients of input variables for the sleeper deflection ordered by importance.	83
9.8	The influence of train speed on: (a) the sleeper elastic deflection; (b) the dynamic amplification factor.	84
10.1	Wear weight cost W_{wear} in function of z , and z_{sub} in function of speed.	90
10.2	Wear weight cost W_{wear} in function of speed V	91
10.3	Settlement of ballast.	93
10.4	Scheme of ballast interventions.	94
10.5	Settlement of ballast caused by the pass of the train tr	95
10.6	Example of toll in function of train speed.	96
11.1	Type of excitation for the receptance simulation: (a) centered train, midspan excitation; (b) centered train, on-sleeper excitation.	100
11.2	Analysis of receptance of the coupled system for different combinations: (a) centered train, midspan excitation; (b) centered train, on-sleeper excitation.	101
11.3	Waves propagation in time and in space in the case of centered train, on-sleeper excitation.	102
11.4	Type of excitation for the receptance simulation: (a) centered third wheel, midspan excitation; (b) centered third wheel, on-sleeper excitation.	103
11.5	Waves propagation in time and in space in the case of centered third wheel, on-sleeper excitation.	104
11.6	Vertical displacement for the receptance analysis in the scenario 1.	105
11.7	Comparison between: (a) the receptance considering all time-steps and (b) the receptance considering stabilized part in the scenario 1.	105
11.8	Vertical displacement for the receptance analysis in the scenario 2.	106
11.9	Comparison between: (a) the receptance considering all time-steps and (b) the receptance considering stabilized part in the scenario 2.	106
11.10	Vertical displacement for the receptance analysis in the scenario 3.	107
11.11	Comparison between: (a) the receptance considering all time-steps and (b) the receptance considering stabilized part in the scenario 3.	107
11.12	Vertical displacement for the receptance analysis in the scenario 4.	108
11.13	Comparison between: (a) the receptance considering all time-steps and (b) the receptance considering stabilized part in the scenario 4.	108
12.1	Dynamic contact force in function of time at 50 km h^{-1}	110

12.2	Dynamic contact force in function of time at 100 km h ⁻¹	110
12.3	Dynamic contact force in function of time at 130 km h ⁻¹	111
12.4	Dynamic contact force in function of time at 160 km h ⁻¹	111
12.5	Dynamic contact force in function of time at 190 km h ⁻¹	112
12.6	Scenario 3: (a) sleeper vertical displacement and (b) dynamic amplification factor in function of train speed	113
12.7	Scenario 4 (a) Sleeper vertical displacement and (b) dynamic amplification factor in function of train speed	114
12.8	Scenario 5: (a) sleeper vertical displacement and (b) dynamic amplification factor in function of train speed	115
12.9	Scenario 3: comparison between critical speed and resonance frequency	117
12.10	Scenario 4: comparison between critical speed and resonance frequency	118
12.11	Scenario 5: comparison between critical speed and resonance frequency	119
A.1	Octave band and 1/3 octave band frequencies.	125
A.2	Tamping sequence [6]	126
A.3	Stoneblowing sequence [6]	127

INTRODUCTION

1.1 INTRODUCTION

The transport by train of freight and passengers is one of the oldest type of transport and yet a continual improvement process get this service better and better. In these days, with the arrival and developing of high speed trains, the operational range of railways can surround distances in a very short time. This fact had produced a competition even with airplane for some type of segments. The principal directs benefits perceived by passengers are evidently connected to the time and the cost of displacements. Even if the nett duration of displacement by airplane is still lesser than ones by train (due to the difference of speeds), in some cases the total time can results more convenient for the train displacements. Indeed to evaluate the total time that separates the point of origin of the displacement to the point of destination many parameters must to be considered such that: the distance from infrastructure to the point of origin, the time to access to the vehicle, waiting lines, the time spent for passengers control, the time spent to wait luggages, the distance from the arrival infrastructure to the point of destination. Considering all of these parameters, in many cases, even if the airplane is speeder than train, the total time of displacement results lesser by train. This reason and others (such as the continual increasing of petrol cost or pollution) have incited the states to support this development. In particular, member states of EU have begun in last years a real campaign to promote the railways Infrastructure expansion. The principal effects of this campaign, among others, are the deregulation of rail transport, the interoperability of Infrastructure, the creation of Trans-European Networks. All railway lines with an operating speed greater than 250 km h^{-1} are classified In Europe as high-speed line. The necessity to benefit from computer tools had grown up exponentially in last 50 years with the increasing of the operating speed and train development. The numerical models are, in our days, valuable tools for the designing of vehicles, mechanism and structures, to study the wear of the infrastructure, to predict the behaviors of system, the vibrations and the stress exchanged between vehicle and substructure. The objectives of this work are principally two. First this thesis aims to contribute to the advancement of methods, developing a simple and fast numerical method able to simulate the main physical behaviors. The second purpose is, with the support of the tool proposed, to understand and describe two phenomenon: the critical speed and the effect of train and track variables on the ballast settlement. In following paragraphs a resume of main numerical models developed by other authors is done.

1.2 LITERATURE REVIEW

1.2.1 The vehicle/track models

The modern numerical methods used to simulate the behavior of train/track system take advantages from many theories: multi-body systems, finite element (FE), discrete element (DE) and analytical methods. The most authors have focused the attention on vehicle behavior or track behavior (including rail, rail-pads, sleeper, ballast and ground). Only few of them have treated the coupled system studying the interaction between vehicle and track. The methods used to model vehicle, rail, rail-pads, sleepers, ballast and ground can be summarized here:

- method adopted to model the vehicle: 2D or 3D multi-body systems;
- method adopted to model the rail: analytical model (Euler-Bernoulli or Timoshenko), 2D or 3D FEM;
- rail-pads: FE models, simple connection (spring/damper couple), analytical models;
- sleepers: FE models, rigid elements connected by spring/damper couple, analytical models;
- ballast: FE models, DE models, analytical models, rigid elements connected by spring/damper couple;
- ground: FE models, analytical models, rigid elements connected by spring/damper couple.

Often, when the track is the object of studies, the vehicle is represented by a load with sinusoidal excitation or moving load simulating the contact force. Similarly, when the vehicle is the object of studies, the track is represented by a rigid structure. The multi-body methods allow to model the dynamic behavior of train principally. This methods are very common and many authors [71, 28, 79, 58, 44, 45, 47] have used it to model train vehicles. They have modeled the train coach, or locomotive, with seven two-dimensional rigid elements representing: the body, the two bogies and the four wheels. The bogies are suspended on the wheels by primary suspensions represented by a spring-damper couple. Similarly, the vehicle body is linked with bogies by secondary suspensions. The common 2D or 3D models consider 10, 17 or 27 DOF (degrees or freedom). In 2D models (as in [45, 47]) the 10 DOF considered are the vertical displacement of vehicle body, bogies and wheels; the pitch of bogies and vehicle body. In 3D models (as in [44]) the 7 additional DOF represent the roll movement of: two bogies, vehicle body and four wheel-axis. If the lateral displacement and the yaw movement of each element are considered too, 10 additional DOF are considered (as in [28, 79]). Guo et al. [28] have presented a coupled vehicle/track model to study the behavior of the Shinkansen train passing on a bridge. Xu and Ding [79] have studied the effect of cross-winds on the vehicle/track interaction. Pombo et al. [58] have studied the effect of wear of the rail-head on the dynamic behavior of vehicle. Additionally the motion during way curves is treated with a 3D model. Kumaran et al. [44] have presented a 3D FE model of track structure and a multi-body model of train. They have focused the attention on sleeper stress. Other authors [64, 16, 40] have treated the propagation of

vibrations through the ground. Cai et al. [16] have studied the response of pavement systems subjected to a moving traffic load. They have simulated the traffic loads as four rectangular load pressures, and the rigid and flexible pavement systems have been regarded as an infinite plate resting on a poroelastic half-space soil medium. A similar model has been presented by Karlström [40]. He has modeled the ground as a stratified half-space with linearly viscoelastic layers. A rectangular embankment supporting the rails and the sleepers has been placed on the top of the ground. Salvador et al. [65] have presented an analytical method with two layers: the first one representing the track and ballast, and the second one representing the subgrade and soil. They have modeled the train as a moving load. Johansson and Nielsen [36] have presented a study of rail corrugation growth. They have focused the study on the influence of powered wheel-sets with wheel tread irregularities. Jens C.O. Nielsen [35] has proposed a model to predict wheel-rail contact forces. He has focused the attention on frequency analysis of contact force comparing it to experimental measurements and studying the relation with rail-head corrugation. Ricci et al. [63] have presented a discrete/continuum double layer model to simulate track behavior. They have modeled the train as a moving load. The ballast has been modeled with discrete elements representing the ballast grains.

1.2.2 The ballast settlement models

Many authors [14, 56, 68, 27, 8, 9, 33?] show how the ballast vertical settlement is proportional to the elastic deflection caused by each wheel pass and the number of applied wheel loads. Bodin-Bourgoin et al. [14] and Guerin [27] have proposed a linear proportion between settlement and number of load cycles. Moreover they have studied a relationship between the grow rate of settlement and the elastic deflection of ballast at every load cycle doing tests on scale models. Paderno [56] has accomplished tests on a 1 : 1 model. She has studied the influence of ballast interventions and traffic on settlement and ballast aging. Abdelkrim [8] has proposed an analytical numerical method to study the phenomenon.

1.2.3 The critical speed phenomenon

Field observations and measurements have shown an increasing of vibrations and vertical displacements when trains reach a specific speed. Many authors [69, 43, 31, 19, 57] have studied this phenomenon calling it "Critical Train Speed". This "mysterious" critical condition is described as the resonance between the moving train and the Rayleigh wave traveling in the soil embankment (analogous to the "Mach" effect caused by flying objects breaking through the sound barrier) [43]. It has been found that track should have two critical speeds, one equal to the Rayleigh wave velocity of the ground, and other, fairly close, controlled by the bending stiffness and mass of the rail/embankment "beam" in addition to the ground properties [49]. The experimental data [53, 70, 61, 30] have indicated the appearing of this phenomenon in the speed range $100 - 300 \text{ km h}^{-1}$. Green's functions [43, 74, 75], wavelets [46], boundary and finite elements, even with the element net moving with the train [21], have been applied trying to predict track response to trains passing at speeds around the critical value [49]. Huang and Chrismer [31] have developed a 3D dynamic track model to investigate the track performance and ballast settlement under freight and trains moving at critical speed. Varying the speed between 20 and 100 m s^{-1} , they found a critical speed at almost 90 m s^{-1} (324 km h^{-1}). Dimitrovová and Varandas [19] have analyzed the transient dynamic response of a beam supported on a foundation with sudden stiffness change and subjected to a

force moving with constant velocity. They have studied the effect of loads, moving at critical velocities on four different types of foundations. The range of critical velocity studied is between 702 and 1200 km h⁻¹. Anyway at this velocity range, even if the phenomenon caused by the "Mach" effect is possible and physically plausible, it has only academic interests.

Therefore an explanation and a accurate calculation of critical speed perceived under the Rayleigh wave velocity seems to remain a problem unresolved. Indeed the Rayleigh wave velocity of typical grounds (more than 500 km h⁻¹) is very higher if compared to train operative maximum speeds (almost 350 km h⁻¹). Moreover, even in the case of soft ground, as peat layer, where the Railegh wave velocity is in the range 320 – 400 km h⁻¹, measurements [57] allow to observe the phenomenon for trains moving at 135 km h⁻¹ (Mach number close to 0.4).

1.3 THE PLAN OF THE THESIS

The thesis is divided in two parts. The draft of the manuscript reflects the developing of the work conducted in chronological order. In part I, the model of the train/track coupled system is presented. In first chapters the model adopted for the train, the rail model, and the rail-pads, sleeper and ballast model are described separately. Then, in last chapter, the methods adopted to couple the vehicle and the track systems and to solve the motion equation are shown. The results of simulations carried out with the present model are shown in the part II. First, results have been compared to experimental data and literature results to validate the efficacy and efficiency of the model presented. Then the work has been focused on two topics: the railway toll functions related to ballast wear, and the phenomenon of the critical speed.

Part I

The Numerical Model

IN this part, the numerical model adopted to simulate the vehicle/track system is presented. The first chapters are centered on modeling of vehicle, rail, rail-pads, sleepers and ballast. Each chapter is presented following the same framework. first a literature review of common models used is shown for the component of vehicle/track introduced. Consequently, the model adopted is presented. Then its motion equations for each DOF are shown and assembled in matrix form. Finally the values of model parameters adopted are discussed. The last chapter is dedicated to present the methods of resolution adopted to solve motion equations.

THE VEHICLE MODEL

2

2.1 THE MODEL

The aim of this thesis is to find a solution to reduce the dynamic overload. So, the worst effects caused by trains pass have been considered. The locomotive is the heavier vehicle, indeed it contains the engine and all the components needed for the train motion. It can be assumed that locomotive effects are the worst. For this reason in the present model only the locomotive effects are considered. Often in new high-speed trains the motor bogies are present in many train coaches (normally the first and the last one). At this conditions, the stress in vehicles connection is reduced and moreover the power weight ratio increases. Weight per axle of power unit (M) and trailers (T) for some trains are reported in table 2.1 Anyway in this work the attention will be focused on the part

Weight and max speed for some high speed trains				
	x2000	ETR500	AVE-T350	
max speed	275.7	300	330	Km h ⁻¹
weight per axle (M)	18	17	22.5	tonn
weight per axle (T)	12.2	10.5	14.8 – 17	tonn

Table 2.1 – Values taken from [5, 55, 4, 26, 2].

of substructure more charged by each axle; therefore the volume of ballast under every wheel. In this case the effects produced by other train bogies are negligible. the vehicle is modeled as seven discrete elements in accordance to [80, 81, 47, 25, 23, 24, 34]. There are seven two-dimensional rigid elements representing: the body, the two bogies and the four wheels. The problem is solved under the assumption of symmetry, so all the masses are considered as half of their values. The bogies are suspended on the wheels by primary suspensions represented by a spring-damper couple. Similarly, the vehicle body is linked with bogies by secondary suspensions. Ten degrees of freedom are considered: the vertical displacement of vehicle body, bogies and wheels; the pitch of bogies and vehicle body. A draft of the vehicle model is shown in figure 2.1.

2.2 ASSEMBLED MOTION EQUATIONS FOR THE VEHICLE MODEL

The set of DOF (degrees of freedom) are represented in figure 2.1 and is governed by the following system of motion equations 2.1.

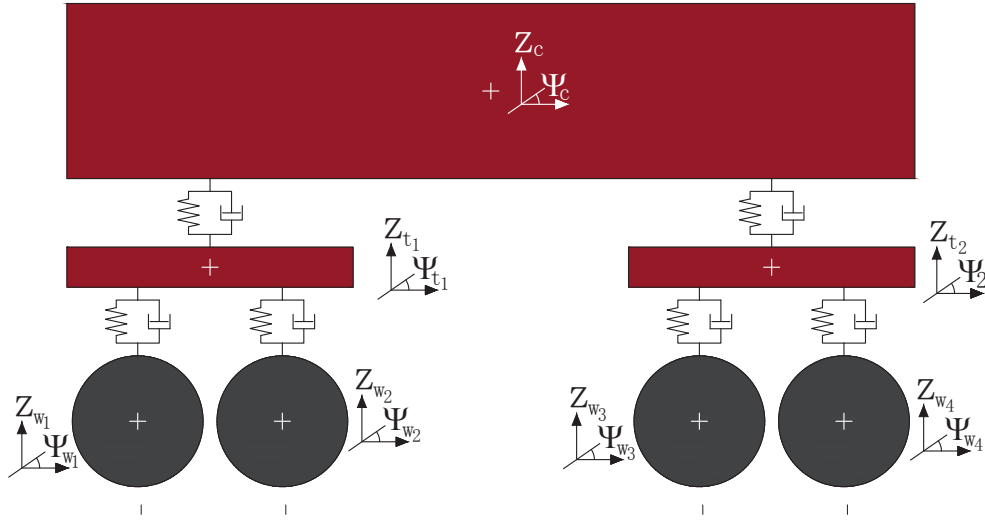


Figure 2.1 – A draft of the vehicle model

$$\begin{aligned}
 z_c : \quad & m_c \ddot{z}_c + c_2(\dot{z}_c - \dot{z}_{t1}) + c_2(\dot{z}_c - \dot{z}_{t1}) + k_2(z_c - z_{t1}) + k_2(z_c - z_{t1}) = m_c g \\
 \Psi_c : \quad & J_c \ddot{\Psi}_c + c_2(\dot{\Psi}_c - \dot{\Psi}_{t1})l_t + c_2(\dot{\Psi}_c - \dot{\Psi}_{t1})l_t + k_2(\Psi_c - \Psi_{t1})l_t + k_2(\Psi_c - \Psi_{t1})l_t = 0 \\
 z_{t1} : \quad & \ddot{z}_{t1}m_{t1} + c_2(\dot{z}_{t1} - \dot{z}_c) - c_2\dot{z}_{t1}l_t + c_1(\dot{z}_{t1} - \dot{z}_{w1}) + c_1(\dot{z}_{t1} - \dot{z}_{w2}) + \\
 & + k_2(z_{t1} - z_c) - k_2z_{t1}l_t + k_1(z_{t1} - z_{w3}) + k_1(z_{t1} - z_{w4}) = m_{t1}g \\
 \Psi_{t1} : \quad & \ddot{\Psi}_{t1}J_{t1} + c_1(\dot{\Psi}_{t1}l_w - \dot{z}_{w1})l_w + c_1(\dot{\Psi}_{t1}l_w - \dot{z}_{w2})l_w + \\
 & + k_1(\Psi_{t1}l_w - z_{w1})l_w + k_1(\Psi_{t1}l_w - z_{w2})l_w = 0 \\
 z_{t2} : \quad & \ddot{z}_{t2}m_{t2} + c_2(\dot{z}_{t2} - \dot{z}_c) - c_2\dot{z}_{t2}l_t + c_1(\dot{z}_{t2} - \dot{z}_{w1}) + c_1(\dot{z}_{t2} - \dot{z}_{w2}) + \\
 & + k_2(z_{t2} - z_c) - k_2z_{t2}l_t + k_1(z_{t2} - z_{w1}) + k_1(z_{t2} - z_{w2}) = m_{t2}g \\
 \Psi_{t2} : \quad & \ddot{\Psi}_{t2}J_{t2} + c_1(\dot{\Psi}_{t2}l_w - \dot{z}_{w3})l_w + c_1(\dot{\Psi}_{t2}l_w - \dot{z}_{w4})l_w + \\
 & + k_1(\Psi_{t2}l_w - z_{w3})l_w + k_1(\Psi_{t2}l_w - z_{w4})l_w = 0 \\
 z_{w,j=1,2} : \quad & \ddot{z}_{wj}m_{wj} + c_1(\dot{z}_{wj} - \dot{z}_{t1} - \dot{\Psi}_{t1}l_w) + k_1(z_{wj} - z_{t1} - \Psi_{t1}l_w) + R_{r/wj} = m_{wj}g \\
 z_{w,j=3,4} : \quad & \ddot{z}_{wj}m_{wj} + c_1(\dot{z}_{wj} - \dot{z}_{t2} - \dot{\Psi}_{t2}l_w) + k_1(z_{wj} - z_{t2} - \Psi_{t2}l_w) + R_{r/wj} = m_{wj}g
 \end{aligned} \tag{2.1}$$

where $2l_w$ is the wheelbase, $2l_t$ is the distance between the bogies pivot points, g is the gravity and R_{r/w_j} the reaction force of the rail on the wheel j . The system of equations (2.1) can be written in the matrix form:

$$\mathbf{M}_v \ddot{\mathbf{z}}_v + \mathbf{C}_v \dot{\mathbf{z}}_v + \mathbf{K}_v \mathbf{z}_v - \mathbf{f}_{sub/v}(\mathbf{z}_v, \mathbf{z}_{sub}) = -\mathbf{q}_v, \quad (2.2)$$

The displacement vector \mathbf{z}_v , the forces vector $\mathbf{f}_{sub/v}$, the mass matrix \mathbf{M}_v , the stiffness matrix \mathbf{K}_v and the damping matrix \mathbf{C}_v are defined by:

$$\mathbf{z}_v = \begin{bmatrix} z_c \\ \Psi_c \\ z_t \\ \Psi_t \\ z_t \\ \Psi_t \\ z_{w_1} \\ z_{w_2} \\ z_{w_3} \\ z_{w_4} \end{bmatrix}_{10 \times 1}, \quad \mathbf{q}_v = \begin{bmatrix} m_c g \\ 0 \\ m_t g \\ 0 \\ m_t g \\ 0 \\ m_w g \\ m_w g \\ m_w g \\ m_w g \end{bmatrix}_{10 \times 1}, \quad \mathbf{f}_{sub/v} = \begin{bmatrix} 0 \\ 0 \\ 0 \\ 0 \\ 0 \\ 0 \\ -R_{r/w_1} \\ -R_{r/w_2} \\ -R_{r/w_3} \\ -R_{r/w_4} \end{bmatrix}_{10 \times 1}, \quad (2.3)$$

$$\mathbf{M}_v = \text{diag} [m_c \quad J_c \quad m_t \quad J_t \quad m_t \quad J_t \quad m_w \quad m_w \quad m_w \quad m_w]_{10 \times 10}, \quad (2.4)$$

$$\mathbf{K}_v = \begin{bmatrix} 2k_2 & 0 & -k_2 & 0 & -k_2 & 0 & 0 & 0 & 0 & 0 \\ 0 & 2k_2 l_t^2 & -k_2 l_t & 0 & k_2 l_t & 0 & 0 & 0 & 0 & 0 \\ -k_2 & -k_2 l_t & k_2 + 2k_1 & 0 & 0 & 0 & -k_1 & -k_1 & 0 & 0 \\ 0 & 0 & 0 & 2k_1 l_w^2 & 0 & 0 & -k_1 l_w & k_1 l_w & 0 & 0 \\ -k_2 & k_2 l_t & 0 & 0 & k_2 + 2k_1 & 0 & 0 & 0 & -k_1 & -k_1 \\ 0 & 0 & 0 & 0 & 0 & 2k_1 l_w^2 & 0 & 0 & -k_1 l_w & k_1 l_w \\ 0 & 0 & -k_1 & -k_1 l_w & 0 & 0 & k_1 & 0 & 0 & 0 \\ 0 & 0 & -k_1 & -k_1 l_w & 0 & 0 & 0 & k_1 & 0 & 0 \\ 0 & 0 & 0 & 0 & -k_1 & -k_1 l_w & 0 & 0 & k_1 & 0 \\ 0 & 0 & 0 & 0 & -k_1 & -k_1 l_w & 0 & 0 & 0 & k_1 \end{bmatrix}_{10 \times 10} \quad (2.5)$$

$$\mathbf{C}_v = \begin{bmatrix} 2c_2 & 0 & -c_2 & 0 & -c_2 & 0 & 0 & 0 & 0 & 0 \\ 0 & 2c_2l_t^2 & -c_2l_t & 0 & c_2l_t & 0 & 0 & 0 & 0 & 0 \\ -c_2 & -c_2l_t & c_2 + 2c_1 & 0 & 0 & 0 & -c_1 & -c_1 & 0 & 0 \\ 0 & 0 & 0 & 2c_1l_w^2 & 0 & 0 & -c_1l_w & c_1l_w & 0 & 0 \\ -c_2 & c_2l_t & 0 & 0 & c_2 + 2c_1 & 0 & 0 & 0 & -c_1 & -c_1 \\ 0 & 0 & 0 & 0 & 0 & 2c_1l_w^2 & 0 & 0 & -c_1l_w & c_1l_w \\ 0 & 0 & -c_1 & -c_1l_w & 0 & 0 & c_1 & 0 & 0 & 0 \\ 0 & 0 & -c_1 & -c_1l_w & 0 & 0 & 0 & c_1 & 0 & 0 \\ 0 & 0 & 0 & 0 & -c_1 & -c_1l_w & 0 & 0 & c_1 & 0 \\ 0 & 0 & 0 & 0 & -c_1 & -c_1l_w & 0 & 0 & 0 & c_1 \end{bmatrix}_{10 \times 10} \quad (2.6)$$

The displacement vector \mathbf{z}_{sub} contains the displacements of contact points on the rail. Indeed the contact forces R_{r/w_j} , evaluated by the Hertz theory, are non linear functions of the relative displacements.

2.3 THE MANCHESTER BENCHMARK

The Manchester benchmark [34] has been adopted to assign a value to all vehicle model parameters. This study was carried out for the International Workshop "Computer Simulation of Rail Vehicle Dynamics" at Manchester Metropolitan University on June 23rd and 24th 1997. The aim of the project was to provide a standard reference allowing comparison in calculation to assess the effect of the various techniques and approximations made. Two kind of vehicles were presented. Benchmark vehicle 1 is a general passenger coach with two bogies and a simple primary suspension. Benchmark vehicle 2 is a two axle freight vehicle with load dependent friction damping. Both models are as simple as practically possible and further simplifications during the simulation may be carried out by the package operator if desired. All bodies are considered rigid. The Manchester Benchmark gives also parameters for different type of track. Benchmark vehicle model 1 should be run with in the high speed track. Values of benchmark 1 are reported in table 2.2.

Vehicle specification - Benchmark Vehicle 1		
Masses and Inertias		
wheel mass	1813	kg
bogies mass	2615	kg
bogies pitch inertia	1476	kg m ²
body mass	32000	kg
body pitch inertia	1970000	kg m ²
Primary suspension		
stiffness	1220	kN/m
damping	4	kNs/m
damper series stiffness	1000	kN/m
Secondary suspension		
stiffness	1220	kN/m
damping	32	kNs/m
damper series stiffness	6000	kN/m

Table 2.2 – Values taken from [5, 55, 4, 26, 2].

In the vehicle model presented in our work the stiffness is connected in parallel to the damper; any other series stiffness is connected. In this work the damper series stiffness has been considerate as a parallel spring to evaluate an equivalent value of stiffness. A draft of both of the suspension types is shown in figure 2.2

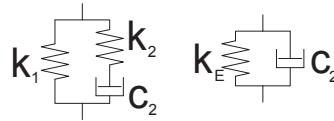


Figure 2.2 – A draft of suspension types

2.4 THE WHEEL-RAIL CONTACT MODEL

The problem of contact between wheel and rail has been abundantly studied by many authors [39, 60, 12, 48, 59]. In our model contact forces between the j^{th} wheel and rail are computed by the non-linear hertz model with hysteresis damping due to Lankarani and Nikravesh [48, 59] as

$$R_{w/r,j} = \begin{cases} k_h \delta^{\frac{3}{2}} + c_h \dot{\delta} & \text{if } \delta > 0, \\ 0 & \text{if } \delta < 0; \end{cases} \quad (2.7)$$

where δ is the total deflection of wheel and rail at the contact point computed as

$$\delta = z_{wj} - z_{rj} - \eta_{rj}, \quad (2.8)$$

in which z_{wj} is the vertical displacement of the j^{th} -wheel, z_{rj} and η_{rj} are the displacement and the vertical defect of rail at j^{th} connection-point respectively; k_h and c_h are the Hertzian and the damping contact coefficient respectively. During the phase of calibration of the model the non dissipative behavior of the Hertz's contact is emerged. So at the end of calibration the damping coefficient c_h has been neglected.

THE RAIL MODEL

3

3.1 SOME OTHER MODELS

Many different approaches have been used to model the rail in recent years. Some works [20, 40, 73] studied the waves propagation through the track-ground system in three dimensions; they modeled rail with Euler-Bernoulli theory as:

$$\frac{\partial z(x, t)}{\partial x^4} + m \frac{\partial^2 z(x, t)}{\partial t^2} + \mu \frac{\partial z(x, t)}{\partial t} + kz(x, t) = Q\delta(x - vt), \quad (3.1)$$

where m is the rail linear mass, μ and k are respectively the linear damping and stiffness of the equivalent winkler foundation, Q is the load, v the train velocity, and δ is the Dirac function. They modeled contact forces as constant or harmonic vertical forces moving along the rail. Others authors [54, 80] studied the coupled train/track system in two dimensions; they modeled rail as a Timoshenko beam connected to pads by singular points as:

$$\begin{cases} \rho A \frac{\partial^2 w_R}{\partial t^2} - GA\chi \left(\frac{\partial^2 w_R}{\partial x^2} - \frac{\partial \phi_R}{\partial x} \right) = - \sum_{i=1}^{N_s} F_{RSi} \delta(x - x_i) + \sum_{j=1}^4 P_{WRj} \delta(x - x_j) \\ \rho I \frac{\partial^2 \phi_R}{\partial t^2} - GA\chi \left(\frac{w_R}{\partial x} - \phi_R \right) - EI \frac{\partial^2 \phi_R}{\partial x^2} = 0 \end{cases}, \quad (3.2)$$

where A is the rail section area, G is the shear modulus, χ is the Timoshenko's coefficient, ρ is the volume density and I is the bending inertia. The other variables are shown in figure 3.1. Still others [45, 47] studied the coupled system modeling rail with

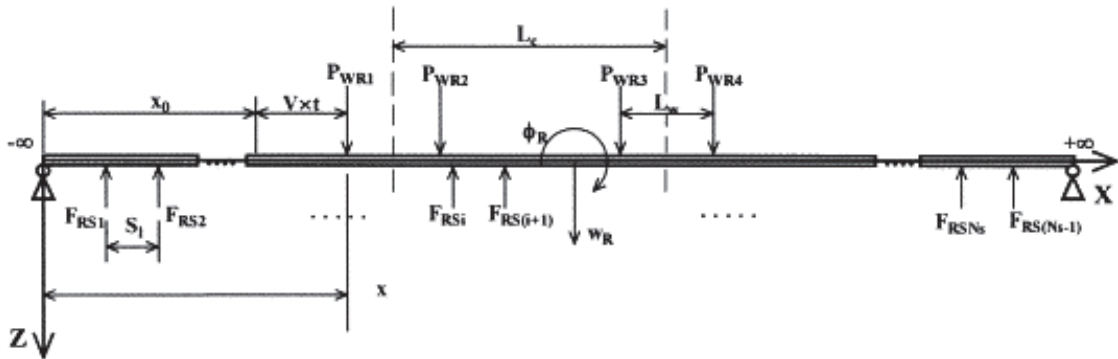


Figure 3.1 – timoshenko beam model of the rail [80]

finite elements connected to pads by singular points; they discretized the rail with a singular finite element for each pair of sleepers. A draft of the singular finite element is shown in figure 3.2. They have expressed the stiffness matrix of an element as:

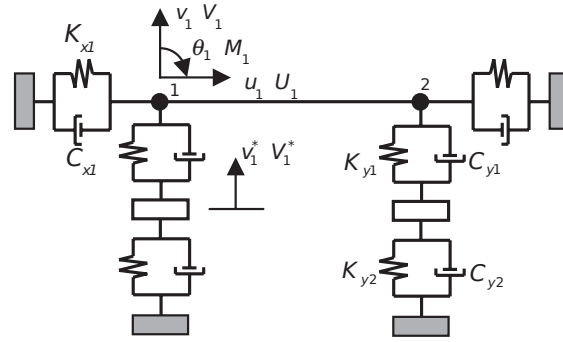


Figure 3.2 – Generalised beam element for the track structure [45]

$$\mathbf{K}_l^e = \mathbf{K}_b^e + \mathbf{K}_e^e, \quad (3.3)$$

where:

$$\mathbf{K}_b^e = \begin{bmatrix} \frac{EA}{l} & 0 & 0 & 0 & -\frac{EA}{l} & 0 & 0 & 0 \\ & \frac{12EI}{l^3} & -\frac{6EI}{l^2} & 0 & 0 & -\frac{12EI}{l^3} & -\frac{6EI}{l^2} & 0 \\ & & \frac{4EI}{l} & 0 & 0 & \frac{6EI}{l^2} & \frac{2EI}{l} & 0 \\ & & & 0 & 0 & 0 & 0 & 0 \\ & & & & \frac{EA}{l} & 0 & 0 & 0 \\ & & & & & \frac{12EI}{l^3} & \frac{6EI}{l^2} & 0 \\ & & & & & & \frac{4EI}{l} & 0 \\ & & & & & & & 0 \\ & & & & & & & 0 \end{bmatrix} \quad (3.4)$$

Symm

and

$$\mathbf{K}_b^e = \begin{bmatrix} K_{x1} & 0 & 0 & 0 & 0 & 0 & 0 & 0 \\ & K_{y1} & 0 & -K_{y1} & 0 & 0 & 0 & 0 \\ & & 0 & 0 & 0 & 0 & 0 & 0 \\ & & & K_{y1} + K_{y2} & 0 & 0 & 0 & 0 \\ & & & & K_{x1} & 0 & 0 & 0 \\ & & & & & K_{y1} & 0 & -K_{y1} \\ & & & & & & 0 & 0 \\ & & & & & & & K_{y1} + K_{y2} \end{bmatrix} \quad (3.5)$$

Symm

3.2 THE REASONS WHY A NEW RAIL MODEL IS PROPOSED

During the processing of this thesis all models shown in the paragraph 3.1 have been implemented. The reasons why an upgrade of the rail model resulted necessary are exposed here.

The Euler-Bernoulli model presents many advantages. It is a simple and diffused model and it results very appropriate to begin tests on model operation. Anyway shear effects are neglected. This is the classical hypothesis assumed for slender beams. The height of the rail section is 148 mm for a 50 *UNI* rail and 172 mm for a 60 *UNI* rail [62]. These values compared to the distance between two sleepers (60–70 cm) are not small enough to allow the slender beam hypothesis.

For this reason the Timoshenko model results better. Anyway in all past models adopting Timoshenko theory the rail is connected to pads by singular points. In truth, the rail is connected to sleepers by a contact zone not negligible if compared to the length of the rail suspended between two consecutive sleepers. Indeed, sleeper base measures between 60 and 70 cm and the pad length along the rail direction measures between 17 and 26 cm.

In the past FEM models [45, 47] three hypothesis have resulted too much restrictive. First, the shear effect cannot be neglected. Afterwards the maximum displacement during vibrations or wheel pass occurs on the midspan point of the rail. These models have discretized the rail with a singular finite element for each pair of sleepers. This kind of discretization cannot represent accurately the real behavior. Finally also in this case the connection-point connection between rail and sleepers results as extreme hypothesis.

3.3 THE NEW PROPOSED RAIL MODEL

A finite element discretization is used to model the rail. Considering insignificant the axial displacement, we discretized the rail with finite beam elements with two degrees of freedom for every node: rotation and vertical displacement. The algorithm allows to choose the number of beam elements between two sleepers and the number of beam elements vertically connected to sleeper by pads. Both 2-nodes and 3-nodes Timoshenko beam elements have been implemented to model rail. Then a comparison between results in both cases have been done to see if the precision rests acceptable with the 2-nodes beams even if the total number of degrees decreases and the computational time too. Following the procedure to evaluate the stiffness, damping and mass matrices of the elements are shown. A draft of the difference between the connection-area and the connection-point model is shown in figure 3.3. It is clear how the deformed shapes could be very different in the different cases.

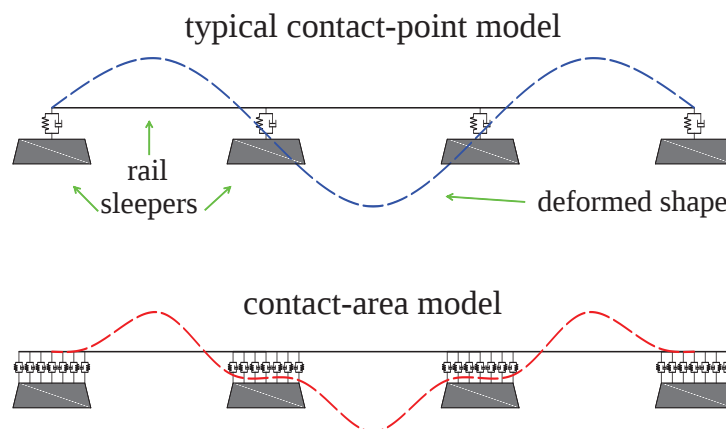


Figure 3.3 – Draft of rail deformed shape in the case of the connection-point model and connection-area model.

3.3.1 The stiffness and mass matrices for the two node Timoshenko element:

The deflection v and the rotation α can be interpolated independently as:

$$\begin{aligned} v &= \mathbf{N} \cdot \mathbf{V} = \begin{bmatrix} n_1 & n_2 \end{bmatrix} \begin{bmatrix} v_1 \\ v_2 \end{bmatrix}, \\ \alpha &= \mathbf{N} \cdot \alpha = \begin{bmatrix} n_1 & n_2 \end{bmatrix} \begin{bmatrix} \alpha_1 \\ \alpha_2 \end{bmatrix}; \end{aligned} \quad (3.6)$$

where the shape function vector N for a 2-node element is:

$$\mathbf{N}^T = \begin{bmatrix} n_1(x) \\ n_2(x) \end{bmatrix} = \begin{bmatrix} 1 - \frac{x}{l} \\ \frac{x}{l} \end{bmatrix}. \quad (3.7)$$

The partial derivatives with respect to x are:

$$\frac{\partial n_1}{\partial x} = -\frac{1}{l} \quad \frac{\partial n_2}{\partial x} = \frac{1}{l}; \quad (3.8)$$

the deformation calculated with the Timoshenko theory are:

$$\begin{aligned} \epsilon_{xx} &= \frac{\partial u}{\partial x} = -y \frac{\partial \alpha_z}{\partial x} \\ \gamma_{xy} &= \frac{\partial v}{\partial x} - \alpha_z \end{aligned} \quad (3.9)$$

Being the vector of degrees of freedom:

$$\mathbf{s}^T = [v_1 \ \alpha_1 \ v_2 \ \alpha_2], \quad (3.10)$$

the deformation ϵ_{xx} and γ_{xy} can be calculated as:

$$\begin{aligned} \epsilon_{xx} &= -y \frac{\partial \alpha}{\partial x} = -y \begin{bmatrix} 0 & \frac{\partial n_1}{\partial x} & 0 & \frac{\partial n_2}{\partial x} \end{bmatrix} \mathbf{s} \\ &= -y \begin{bmatrix} 0 & -\frac{1}{l} & 0 & \frac{1}{l} \end{bmatrix} \mathbf{s} \\ &= \mathbf{b}_{F,1} \mathbf{s}; \end{aligned} \quad (3.11)$$

$$\begin{aligned} \gamma_{xy} &= \frac{\partial v}{\partial x} - \alpha = \begin{bmatrix} \frac{\partial n_1}{\partial x} & 0 & \frac{\partial n_2}{\partial x} & 0 \end{bmatrix} \mathbf{s} - \begin{bmatrix} 0 & n_1 & 0 & n_2 \end{bmatrix} \mathbf{s} \\ &= \begin{bmatrix} -\frac{1}{l} & -n_1 & \frac{1}{l} & -n_2 \end{bmatrix} \mathbf{s} \\ &= \mathbf{b}_{T,1} \mathbf{s}. \end{aligned} \quad (3.12)$$

Now the element stiffness matrix can be calculated as sum of the shear and the bending contribution:

$$\mathbf{K}_1 = \mathbf{K}_{F,1} + \mathbf{K}_{T,1}, \quad (3.13)$$

where:

$$\begin{aligned} \mathbf{K}_{F,1} &= \int_V \mathbf{b}_{F,1}^T \mathbf{E} \mathbf{b}_{F,1} dA dx \\ \mathbf{K}_{T,1} &= \int_V \mathbf{b}_{T,1}^T \mathbf{E} \mathbf{b}_{T,1} dA dx. \end{aligned} \quad (3.14)$$

Being the moment of Inertia $I = \int_A y dA$, the bending contribution of the stiffness matrix can be written as:

$$\begin{aligned}
 \mathbf{K}_{F,1} &= E \int_A y dA \int_l \frac{1}{y} \mathbf{b}_{F,1}^T \mathbf{b}_{F,1} dx \\
 &= EI \int_l \frac{1}{y} \mathbf{b}_{F,1}^T \mathbf{b}_{F,1} dx \\
 &= \frac{EI}{l} \begin{bmatrix} 0 & 0 & 0 & 0 \\ 0 & 1 & 0 & -1 \\ 0 & 0 & 0 & 0 \\ 0 & -1 & 0 & 1 \end{bmatrix};
 \end{aligned} \tag{3.15}$$

and the shear contribution of the stiffness matrix:

$$\begin{aligned}
 \mathbf{K}_{T,1} &= GA\chi \int_l \mathbf{b}_{T,1}^T \mathbf{b}_{T,1} dx \\
 &= \frac{GA\chi}{l} \begin{bmatrix} 1 & \frac{l}{2} & -1 & \frac{l}{2} \\ \frac{l}{2} & \frac{l^2}{3} & -\frac{l}{2} & \frac{l^2}{6} \\ -1 & -\frac{l}{2} & 1 & -\frac{l}{2} \\ \frac{l}{2} & \frac{l^2}{6} & -\frac{l}{2} & \frac{l^3}{3} \end{bmatrix}.
 \end{aligned} \tag{3.16}$$

Anyway, implementing this matrices, a problem has emerged during simulations. Indeed with the shape function shown in equation 3.7 the continuity of rotations is not assured. In this case, during the motion of train, the wheel meets a variation of deflection in correspondence of nodes. This fact adds a noise frequency in the contact-force signal with wavelength equal to length of a beam element l . If the continuity of deflections and rotations are both requested, the order of continuity is C^2 . At this condition the shape functions are polynomial functions of third degree. The shape functions vector due to bending is:

$$\mathbf{N}_b = [n_{b,1} \quad n_{b,2} \quad n_{b,3} \quad n_{b,4}], \tag{3.17}$$

and its components:

$$\begin{aligned}
 n_{b,1} &= \frac{1}{1+\phi} (1 + 2\xi^3 - 3\xi^2 + \phi(1-\xi)) \\
 n_{b,2} &= \frac{l}{1+\phi} \left(\xi + \xi^3 - 2\xi^2 + \frac{\phi}{2}(\xi - \xi^2) \right) \\
 n_{b,3} &= \frac{1}{1+\phi} (-2\xi^3 + 3\xi^2 + \phi\xi) \\
 n_{b,4} &= \frac{l}{1+\phi} \left(\xi^3 - \xi^2 + \frac{\phi}{2}(\xi^2 - \xi) \right).
 \end{aligned} \tag{3.18}$$

The shape functions vector due to rotation is:

$$\mathbf{N}_r = [n_{r,1} \quad n_{r,2} \quad n_{r,3} \quad n_{r,4}], \tag{3.19}$$

and its components:

$$\begin{aligned}
 n_{r,1} &= \frac{6}{(1+\phi)l}(\xi - \xi^2) \\
 n_{r,2} &= \frac{1}{1+\phi}(3\xi^2 - 4\xi + 1 + \phi(1 - \xi)) \\
 n_{r,3} &= \frac{1}{(1+\phi)l}(6\xi - 6\xi^2) \\
 n_{r,4} &= \frac{1}{1+\phi}(3\xi^2 - 2\xi + \phi\xi);
 \end{aligned} \tag{3.20}$$

where:

$$\phi = \frac{12}{l^2} \frac{EI}{GA\chi}. \tag{3.21}$$

The deformation ϵ_{xx} and γ_{xy} can be calculated as:

$$\begin{aligned}
 \epsilon_{xx} &= -y \frac{\partial \alpha}{\partial x} \\
 &= -y \frac{\partial \mathbf{N}_r}{\partial X} \mathbf{S} \\
 &= \mathbf{b}_{F,3} \mathbf{S}
 \end{aligned} \tag{3.22}$$

$$\begin{aligned}
 \gamma_{xy} &= \frac{\partial v}{\partial x} - \alpha \\
 &= \left(\frac{\partial \mathbf{N}_b}{\partial X} - \mathbf{N}_r \right) \mathbf{S} \\
 &= \mathbf{b}_{T,3} \mathbf{S}.
 \end{aligned} \tag{3.23}$$

Then, being:

$$\begin{aligned}
 \mathbf{K}_{F,3} &= \int_V \mathbf{b}_{F,3}^T \mathbf{E} \mathbf{b}_{F,3} dA dx \\
 \mathbf{K}_{T,3} &= \int_V \mathbf{b}_{T,3}^T \mathbf{E} \mathbf{b}_{T,3} dA dx.
 \end{aligned} \tag{3.24}$$

the element stiffness matrix is:

$$\begin{aligned}
 \mathbf{K}_3 &= \mathbf{K}_{F,3} + \mathbf{K}_{T,3} \\
 &= \frac{EI}{l^3(1+\phi)} \begin{bmatrix} 12 & 6l & -12 & -6l \\ 6l & (4+\phi)l^2 & -6l & (2-\phi)l^2 \\ -12 & -6l & 12 & -6l \\ 6l & (2-\phi)l^2 & -6l & (4+\phi)l^2 \end{bmatrix}.
 \end{aligned} \tag{3.25}$$

The mass matrix is:

$$\mathbf{M}_3 = \int_v \rho \mathbf{N}_b^T \mathbf{N}_b dv = \rho A \int_0^l \mathbf{N}_b^T \mathbf{N}_b dv$$

$$= \begin{bmatrix} \frac{13}{35}l + \frac{7}{10}l\phi + \frac{1}{3}l^2\phi^2 & \frac{11}{210}l^2 + \frac{11}{120}l^2\phi + \frac{1}{24}l^2\phi^2 & \frac{9}{70}l + \frac{3}{10}l\phi + \frac{1}{6}l\phi^2 & -\frac{13}{420}l^2 - \frac{3}{40}l^2\phi - \frac{1}{24}l^2\phi^2 \\ \frac{1}{105}l^3 + \frac{1}{60}l^3\phi + \frac{1}{120}l^3\phi^2 & \frac{13}{420}l^2 + \frac{3}{40}l^2\phi + \frac{1}{24}l^2\phi^2 & -\frac{1}{140}l^3 - \frac{1}{60}l^3\phi - \frac{1}{120}l^3\phi^2 \\ \frac{13}{35}l + \frac{7}{10}l\phi + \frac{1}{3}l^2\phi^2 & -\frac{11}{210}l^2 - \frac{11}{120}l^2\phi - \frac{1}{24}l^2\phi^2 & \frac{1}{105}l^3 + \frac{1}{60}l^3\phi + \frac{1}{120}l^3\phi^2 \\ \frac{1}{105}l^3 + \frac{1}{60}l^3\phi + \frac{1}{120}l^3\phi^2 & \frac{1}{105}l^3 + \frac{1}{60}l^3\phi + \frac{1}{120}l^3\phi^2 & \frac{1}{105}l^3 + \frac{1}{60}l^3\phi + \frac{1}{120}l^3\phi^2 \end{bmatrix}$$

symm

(3.26)

3.3.2 The stiffness and mass matrices for the three node Timoshenko element:

The deflection at the generic coordinate can be calculated as function of the deflections of the three nodes as:

$$v = \mathbf{N} \cdot \mathbf{V} = [n_1 \quad n_2 \quad n_3] \begin{bmatrix} v_1 \\ v_2 \\ v_3 \end{bmatrix}, \quad (3.27)$$

where the shape function vector N for a 3-node element in accordance to figure 3.4 is [72]:

$$\mathbf{N}^T = \begin{bmatrix} n_1(\xi) \\ n_2(\xi) \\ n_3(\xi) \end{bmatrix} = \begin{bmatrix} \frac{\xi}{2}(\xi - 1) \\ 1 - \xi^2 \\ \frac{\xi}{2}(\xi + 1) \end{bmatrix}, \quad (3.28)$$

and the partial derivatives with respect to the ξ are:

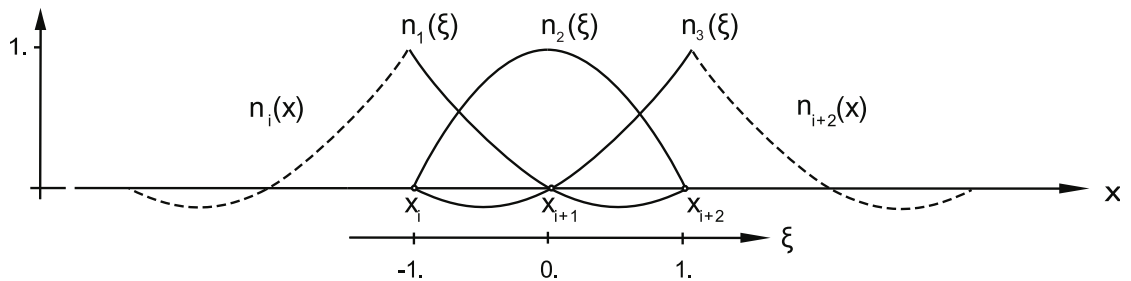


Figure 3.4 – Local shape functions for 3-node element [72]

$$\frac{\partial n_1}{\partial \xi} = -\frac{1}{2} + \xi \quad \frac{\partial n_2}{\partial \xi} = -2\xi \quad \frac{\partial n_3}{\partial \xi} = \frac{1}{2} + \xi ; \quad (3.29)$$

the jacobian is:

$$\mathbf{J} = \mathbf{N} \mathbf{X} = \begin{bmatrix} \frac{\xi}{2}(\xi - 1) & 1 - \xi^2 & \frac{\xi}{2}(\xi + 1) \end{bmatrix} \begin{bmatrix} 0 \\ l/2 \\ l \end{bmatrix}, \quad (3.30)$$

$$\mathbf{J} = \frac{l}{2} \quad \mathbf{J}^{-1} = \frac{2}{l} \quad \det \mathbf{J} = \frac{l}{2},$$

where l is the length of the element, and the reference system for the ξ start from the second node. The deformations are calculated with the Timoshenko theory as seen in equation 3.9. Being the vector of degrees of freedom:

$$\mathbf{s}^T = [v_1 \ \alpha_1 \ v_2 \ \alpha_2 \ v_3 \ \alpha_3], \quad (3.31)$$

the deformation ϵ_{xx} and γ_{xy} can be calculated as:

$$\begin{aligned} \epsilon_{xx} &= -y \frac{\partial \alpha}{\partial x} = -y \begin{bmatrix} 0 & \frac{\partial n_1}{\partial x} & 0 & \frac{\partial n_2}{\partial x} & 0 & \frac{\partial n_3}{\partial x} \end{bmatrix} \mathbf{s} \\ &= -y \mathbf{J}^{-1} \begin{bmatrix} 0 & \frac{\partial n_1}{\partial \xi} & 0 & \frac{\partial n_2}{\partial \xi} & 0 & \frac{\partial n_3}{\partial \xi} \end{bmatrix} \mathbf{s} \\ &= -y \frac{2}{l} \begin{bmatrix} 0 & -\frac{1}{2} + \xi & 0 & -2\xi & 0 & \frac{1}{2} + \xi \end{bmatrix} \mathbf{s} \\ &= \mathbf{b}_{F,2} \mathbf{s}; \end{aligned} \quad (3.32)$$

$$\begin{aligned} \gamma_{xy} &= \frac{\partial v}{\partial x} - \alpha = \begin{bmatrix} \frac{\partial n_1}{\partial x} & -n_1 & \frac{\partial n_2}{\partial x} & -n_2 & \frac{\partial n_3}{\partial x} & -n_3 \end{bmatrix} \mathbf{s} \\ &= \begin{bmatrix} \frac{2}{l} \left(-\frac{1}{2} + \xi \right) & \frac{1}{2}(1 - \xi) & -\frac{4}{l}\xi & -(1 - \xi^2) & \frac{2}{l} \left(\frac{1}{2} + \xi \right) & -\frac{1}{2}\xi(1 + \xi) \end{bmatrix} \mathbf{s} \\ &= \mathbf{b}_{T,2} \mathbf{s}. \end{aligned} \quad (3.33)$$

Now the element stiffness matrix can be calculated as sum of the shear and bending contribution:

$$\mathbf{K}_2 = \mathbf{K}_{F,2} + \mathbf{K}_{T,2}, \quad (3.34)$$

where:

$$\begin{aligned} \mathbf{K}_{F,2} &= \int_V \mathbf{b}_{F,2}^T \mathbf{E} \mathbf{b}_{F,2} dA dx \\ \mathbf{K}_{T,2} &= \int_V \mathbf{b}_{T,2}^T \mathbf{E} \mathbf{b}_{T,2} dA dx. \end{aligned} \quad (3.35)$$

Being the moment of Inertia $I = \int_A y dA$, the bending contribution of the stiffness matrix can be written as:

$$\begin{aligned}
\mathbf{K}_{F,2} &= \frac{2E}{l} \int_A y dA \int_l \frac{l}{2y} \mathbf{b}_{F,2}^T \mathbf{b}_{F,2} dx \\
&= \frac{2EI}{l} \int_l \frac{l}{2y} \mathbf{b}_{F,2}^T \mathbf{b}_{F,2} dx \\
&= \frac{2EI}{l} \begin{bmatrix} 0 & 0 & 0 & 0 & 0 & 0 \\ 0 & \frac{7}{6} & 0 & -\frac{4}{3} & 0 & \frac{1}{6} \\ 0 & 0 & 0 & 0 & 0 & 0 \\ 0 & \frac{4}{3} & 0 & \frac{8}{3} & 0 & -\frac{4}{3} \\ 0 & 0 & 0 & 0 & 0 & 0 \\ 0 & \frac{1}{6} & 0 & -\frac{4}{3} & 0 & \frac{7}{6} \end{bmatrix};
\end{aligned} \tag{3.36}$$

and the shear contribution of the stiffness matrix:

$$\begin{aligned}
\mathbf{K}_{T,2} &= GA\chi \int_l \mathbf{b}_{T,2}^T \mathbf{b}_{T,2} dx \\
&= \frac{GA\chi l}{2} \begin{bmatrix} \frac{7}{3l^3} & \frac{1}{2l^2} & -\frac{8}{3l^3} & \frac{2}{3l^2} & \frac{1}{3l^3} & -\frac{1}{6l^2} \\ \frac{1}{2l^2} & \frac{2}{15l} & -\frac{2}{3l^2} & \frac{1}{15l} & \frac{1}{6l^2} & -\frac{1}{30l} \\ -\frac{8}{3l^3} & -\frac{2}{3l^2} & \frac{16}{3l^3} & 0 & -\frac{8}{3l^3} & \frac{2}{3l^2} \\ \frac{2}{3l^2} & \frac{1}{15l} & 0 & \frac{8}{15l} & -\frac{2}{3l^2} & \frac{1}{15l} \\ \frac{1}{3l^3} & \frac{1}{6l^2} & -\frac{8}{3l^3} & -\frac{2}{3l^2} & \frac{7}{3l^3} & -\frac{1}{2l^2} \\ -\frac{1}{6l^2} & -\frac{1}{30l} & \frac{2}{3l^2} & \frac{1}{15l} & -\frac{1}{(2l^2)} & \frac{2}{15l} \end{bmatrix}.
\end{aligned} \tag{3.37}$$

The lumped mass matrix of the singular finite element is the following diagonal matrix:

$$\mathbf{M}_2 = \frac{1}{6} \rho A l \begin{bmatrix} 1 & 0 & 0 & 0 & 0 & 0 \\ 0 & 0 & 0 & 0 & 0 & 0 \\ 0 & 0 & 4 & 0 & 0 & 0 \\ 0 & 0 & 0 & 0 & 0 & 0 \\ 0 & 0 & 0 & 0 & 1 & 0 \\ 0 & 0 & 0 & 0 & 0 & 0 \end{bmatrix}. \tag{3.38}$$

3.3.3 The damping matrix

In a first time of the present work the damping matrices of the rail beam elements have been evaluated by the Rayleigh's theory as:

$$\mathbf{C}_e = \alpha \mathbf{M}_e + \beta \mathbf{K}_e. \tag{3.39}$$

To choose the Rayleigh's coefficients, Ekevid et al. [20] suggest following values: $\alpha = 0.005$ and $\beta = 0.005$. However during the phase of calibration of the model the non dissipative behavior of the rail has emerged. The dissipation of vibrations occurs entirely through pads, sleepers and ballast. So at the end of calibration the damping matrix of rail beam elements has been neglected.

3.3.4 The equivalent element nodal forces

The wheel/rail contact force can be considered as a concentrated vertical load moving between nodes. Since the contact point moves along the beams, equivalent nodal forces has to be calculated. To build the equivalent nodal loads vector, three terms have to be considered: the gravitation load q'_{ij} , the wheel/rail contact force f''_{ij} and sleeper/rail connection force f'''_{ij} .

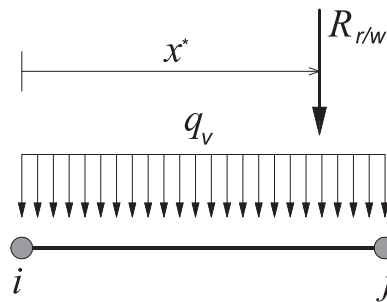


Figure 3.5 – Scheme of forces applied on a beam.

The gravitational term for the generic beam is computed by applying a uniform load q_v (see figure 3.5). The nodal forces vector is:

$$\begin{aligned} \mathbf{q}'_{ij} &= \int_l \mathbf{N}_b(x)^T q_v dl \\ &= \begin{bmatrix} \frac{l}{2} \\ \frac{l^2}{12} \\ \frac{l}{2} \\ \frac{l^2}{12} \end{bmatrix} q_v. \end{aligned} \quad (3.40)$$

The wheel/rail contact force term is added when a contact point is positioned between the nodes i and j (see figure 3.5). If x^* is the distance of the contact point from node i ,

the local forces vector of a beam can be written as

$$\mathbf{f}_{ij}'' = \mathbf{N}_b(x^*)^T R_{w/r}$$

$$= \begin{bmatrix} \frac{1}{1+\phi} \left\{ 1 + 2 \left(\frac{x^*}{l} \right)^3 - 3 \left(\frac{x^*}{l} \right)^2 + \phi \left(1 - \frac{x^*}{l} \right) \right\} \\ \frac{l}{1+\phi} \left\{ \frac{x^*}{l} + \left(\frac{x^*}{l} \right)^3 - 2 \left(\frac{x^*}{l} \right)^2 + \frac{\phi}{2} \left[\frac{x^*}{l} - \left(\frac{x^*}{l} \right)^2 \right] \right\} \\ \frac{1}{1+\phi} \left\{ -2 \left(\frac{x^*}{l} \right)^3 + 3 \left(\frac{x^*}{l} \right)^2 + \phi \frac{x^*}{l} \right\} \\ \frac{l}{1+\phi} \left\{ \left(\frac{x^*}{l} \right)^3 - \left(\frac{x^*}{l} \right)^2 + \frac{\phi}{2} \left[\left(\frac{x^*}{l} \right)^2 - \frac{x^*}{l} \right] \right\} \end{bmatrix} R_{w/r} \quad (3.41)$$

The sleeper/rail connection force occurs when a node i or j is connected to the sleeper. The nodal force is:

$$\mathbf{f}_{ij}''' = \frac{k_p}{n} \begin{bmatrix} z_{r,i} - z_{s,i} \\ 0 \\ z_{r,i} - z_{s,i} \\ 0 \end{bmatrix} + \frac{c_p}{n} \begin{bmatrix} \dot{z}_{r,i} - \dot{z}_{s,i} \\ 0 \\ \dot{z}_{r,j} - \dot{z}_{s,j} \\ 0 \end{bmatrix}$$

$$= \frac{k_p}{n} \begin{bmatrix} z_{r,i} \\ 0 \\ z_{r,j} \\ 0 \end{bmatrix} + \frac{c_p}{n} \begin{bmatrix} \dot{z}_{r,i} \\ 0 \\ \dot{z}_{r,j} \\ 0 \end{bmatrix} - \frac{k_p}{n} \begin{bmatrix} z_{s,i} \\ 0 \\ z_{s,j} \\ 0 \end{bmatrix} - \frac{c_p}{n} \begin{bmatrix} \dot{z}_{s,i} \\ 0 \\ \dot{z}_{s,j} \\ 0 \end{bmatrix} \quad (3.42)$$

$$= \mathbf{f}_{ij,1}'''(\mathbf{z}_r) + \mathbf{f}_{ij,2}'''(\dot{\mathbf{z}}_r) + \mathbf{f}_{ij,3}'''(\mathbf{z}_s) + \mathbf{f}_{ij,4}'''(\dot{\mathbf{z}}_s).$$

In the next paragraph 3.4 the material coefficients included in $\mathbf{f}_{ij,1}'''(\mathbf{z}_r)$ and $\mathbf{f}_{ij,2}'''(\dot{\mathbf{z}}_r)$ will be added in the stiffness and damping matrices of the rail; and those included in $\mathbf{f}_{ij,3}'''(\mathbf{z}_s)$ and $\mathbf{f}_{ij,4}'''(\dot{\mathbf{z}}_s)$ will be added in the stiffness and damping matrices of the substructure (paragraph 4.4, equation 4.10).

3.4 ASSEMBLED MOTION EQUATIONS FOR THE RAIL MODEL

As explained in paragraph 3.3 the beam elements of rail in contact with pads are vertically connected to sleeper by spring-damper couples representing the behavior of pads. This connection is physically equivalent to nodal forces as seen in equations 3.42. The first two terms of this equation can be treated as an increment of stiffness in nodes connected to sleeper. This condition simplifies the implementation and the resolution of model. Then, four different types of local matrices have to be built (see 3.6).

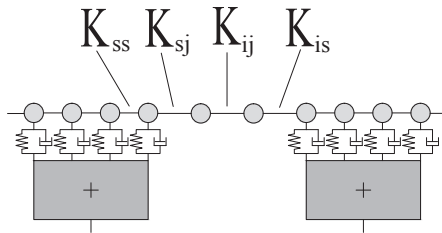


Figure 3.6 – The four type of stiffness matrices for the rail

The local stiffness matrix \mathbf{K}_{ij} for a generic beam not connected to sleepers is \mathbf{K}_1 or \mathbf{K}_2 or \mathbf{K}_3 calculated by equations 3.13, 3.25, 3.34. The local stiffness matrix for a generic beam connected to a sleeper in the first node is¹

$$\mathbf{K}_{sj} = \mathbf{K}_{ij} + \frac{k_p}{n} \begin{bmatrix} 1 & 0 & 0 & 0 \\ 0 & 0 & 0 & 0 \\ 0 & 0 & 0 & 0 \\ 0 & 0 & 0 & 0 \end{bmatrix}; \quad (3.43)$$

the local stiffness matrix for a generic beam connected to a sleeper in the last node is

$$\mathbf{K}_{is} = \mathbf{K}_{ij} + \frac{k_p}{n} \begin{bmatrix} 0 & 0 & 0 & 0 \\ 0 & 0 & 0 & 0 \\ 0 & 0 & 1 & 0 \\ 0 & 0 & 0 & 0 \end{bmatrix}; \quad (3.44)$$

the local stiffness matrix for a generic beam connected to a sleeper by both nodes is

$$\mathbf{K}_{ss} = \mathbf{K}_{ij} + \frac{k_p}{n} \begin{bmatrix} 1 & 0 & 0 & 0 \\ 0 & 0 & 0 & 0 \\ 0 & 0 & 1 & 0 \\ 0 & 0 & 0 & 0 \end{bmatrix}; \quad (3.45)$$

where k_p/n represents the vertical stiffness of the pad divided by the number of springs modeling the connection. Similarly the four types of damping matrices \mathbf{C}_{ij} , \mathbf{C}_{sj} , \mathbf{C}_{is} and \mathbf{C}_{ss} can be evaluated as:

$$\mathbf{C}_{sj} = \mathbf{C}_{ij} + \frac{c_p}{n} \begin{bmatrix} 1 & 0 & 0 & 0 \\ 0 & 0 & 0 & 0 \\ 0 & 0 & 0 & 0 \\ 0 & 0 & 0 & 0 \end{bmatrix}; \quad (3.46)$$

$$\mathbf{C}_{is} = \mathbf{C}_{ij} + \frac{c_p}{n} \begin{bmatrix} 0 & 0 & 0 & 0 \\ 0 & 0 & 0 & 0 \\ 0 & 0 & 1 & 0 \\ 0 & 0 & 0 & 0 \end{bmatrix}; \quad (3.47)$$

$$\mathbf{C}_{ss} = \mathbf{C}_{ij} + \frac{c_p}{n} \begin{bmatrix} 1 & 0 & 0 & 0 \\ 0 & 0 & 0 & 0 \\ 0 & 0 & 1 & 0 \\ 0 & 0 & 0 & 0 \end{bmatrix}; \quad (3.48)$$

Where the matrix \mathbf{C}_{ij} equals to \mathbf{C}_e evaluated as explained in 3.39. Once the stiffness matrices (equations 3.25 or 3.34, 3.43, 3.44, 3.45), the damping matrices (equations 3.39, 3.46, 3.47, 3.48), the mass matrices (equations 3.26 or 3.38) and the local force vector (equation 3.41) are defined for the generic beam element, it is possible to rewrite the equations of motion in the matrix form:

$$\mathbf{M}_r \ddot{\mathbf{z}}_r + \mathbf{C}_r \dot{\mathbf{z}}_r + \mathbf{K}_r \mathbf{z}_r - \mathbf{f}_{v/r}(\mathbf{z}_v, \mathbf{z}_r) - \mathbf{f}_{sub/r}(\mathbf{z}_s) = -\mathbf{q}_r. \quad (3.49)$$

The vector $\mathbf{f}_{v/r}(\mathbf{z}_v, \mathbf{z}_r)$ includes the equivalent nodal forces vector \mathbf{f}_{ij}'' shown in equation 3.41; the vector $\mathbf{f}_{sub/r}$ includes the equivalent nodal forces vector $\mathbf{f}_{ij,3}'''$ and $\mathbf{f}_{ij,4}'''$ shown in equation 3.42; and the vector \mathbf{q}_r includes the equivalent nodal forces vector \mathbf{q}_{ij}' shown in equation 3.40.

¹for simplicity the matrix is considered 4x4; if $\mathbf{K}_{ij} = \mathbf{K}_2$ the stiffness matrix has dimension 6x6; in this case to calculate \mathbf{K}_{sj} the term k_p/n is multiplied by the matrix $\mathbf{E}_{sj,6 \times 6}$ where all values are nulls except of $E_{1,1} = 1$; to calculate \mathbf{K}_{is} the term k_p/n is multiplied by the matrix $\mathbf{E}_{is,6 \times 6}$ where all values are nulls except of $E_{5,5} = 1$.

3.5 A TEST OF THE RAIL MODEL

A comparison with analytical results have been done to test the correctness and the accuracy of the presented rail model. The first test consists in the calculation of the mode shapes of a cantilever beam. Once the stiffness and the mass matrices have been evaluated for each element, they can be assembled in the global stiffness. Then the boundary conditions have to be applied. The target is to calculate the natural frequency of a cantilever beam with a rectangular section (figure 3.7) in the hypothesis of slender beam and stocky beam. The boundary conditions are:

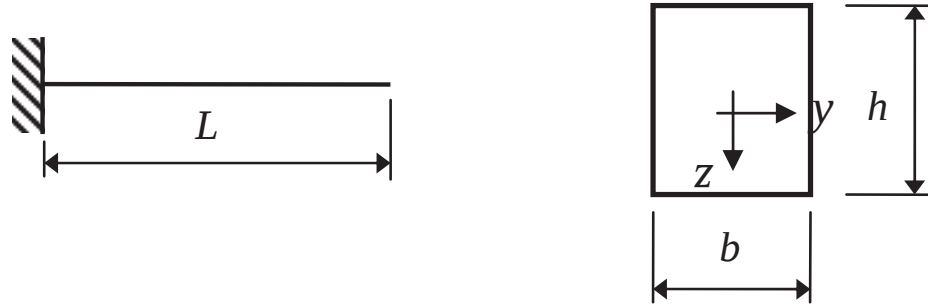


Figure 3.7 – Cantilever beam and its transversal section

$$\begin{cases} v = 0, & x = 0; \\ \phi = 0 & x = 0; \end{cases} \quad (3.50)$$

A similar condition is to set an infinity value in the correspondent degree of freedom of the global stiffness matrix. Then to find the natural frequencies it is sufficient to find the solutions of the equation:

$$\mathbf{M}\ddot{\mathbf{z}} + \mathbf{K}\dot{\mathbf{z}} = \mathbf{0}. \quad (3.51)$$

This differential equation has this type of solution:

$$\mathbf{z} = \mathbf{a} \sin(\omega t); \quad (3.52)$$

the first two derivatives are:

$$\begin{aligned} \dot{\mathbf{z}} &= \mathbf{a}\omega \cos(\omega t) \\ \ddot{\mathbf{z}} &= -\mathbf{a}\omega^2 \sin(\omega t); \end{aligned} \quad (3.53)$$

so the equation 3.51 can be written as:

$$\begin{aligned} -\mathbf{a}\omega^2 \mathbf{M} \sin(\omega t) + \mathbf{a}\mathbf{K} \sin(\omega t) &= \mathbf{0} \\ (\mathbf{K} - \omega^2 \mathbf{M})\mathbf{a} &= \mathbf{0} \\ (\mathbf{M}^{-1}\mathbf{K} - \omega^2 \mathbf{I}) \mathbf{a} &= \mathbf{0}. \end{aligned} \quad (3.54)$$

The solutions are: $\mathbf{a} = \mathbf{0}$ (the banal one), and the others can be found solving the equation:

$$\det |\mathbf{M}^{-1}\mathbf{K} - \omega^2 \mathbf{I}| = 0. \quad (3.55)$$

So the natural pulsations are the eigenvalues of the matrix $\mathbf{A}_{\text{eig}} = \mathbf{M}^{-1}\mathbf{K}$. The eigenvectors represent the natural shape functions. Analytically, the pulsations of a slender cantilever beam can be calculated with the Euler-Bernoulli theory as [17]:

$$\omega_i = \beta_i^2 \sqrt{\frac{EI}{\rho A}}, \quad (3.56)$$

where β_i are the solutions of the transcendental equation:

$$\cos(\beta_i L) \cosh(\beta_i L) + 1 = 0. \quad (3.57)$$

In table 3.1 the natural frequencies calculated analytically are compared with the natural frequencies calculated with the finite element method in the case of a slender beam. Moreover the results are shown in function of the number of element chosen for the discretization. The values adopted for the beam are are:

- $L = 1$ m;
- $b = 10$ mm;
- $h = 10$ mm;
- $A = 10^{-4}$ m²;
- $I = 8,333 \cdot 10^{-10}$ m⁴;
- $E = 2,1 \cdot 10^{11}$ N/m² (steel);
- $\nu = 0,3$ (the Poisson's ratio) ;
- $\rho = 7850$ kg/m³.

natural frequencies of a slender cantilever beam							
mode	theory	$N = 5$	ϵ	$N = 10$	ϵ	$N = 15$	ϵ
1	8,33	8,29	-0,43%	8,29	-0,45%	8,29	-0,44%
2	52,24	51,99	-0,47%	51,97	-0,52%	51,97	-0,52%
3	146,26	146,00	-0,18%	145,52	-0,51%	145,49	-0,53%
4	286,61	288,34	0,60%	285,27	-0,47%	285,06	-0,54%
5	473,80	478,40	0,97%	472,14	-0,35%	471,19	-0,55%
6	707,77	794,38	12,24%	706,98	-0,11%	704,00	-0,53%

Table 3.1 – Natural frequencies for a slender cantilever beam

In the case of a stocky beam the natural frequencies can be calculated analytically from the Timoshenko theory. The procedure is described in [50]. In the tables 3.2 and 3.3 the natural frequencies for a stocky beam are calculated by three different ways: the Euler-Bernoulli theory, the Timoshenko theory, the finite element method. Moreover the comparison is shown in two cases:

- the case of lumped mass matrix (table 3.2);
- the case of consistent mass matrix (table 3.3).

The parameters adopted for the beam are the same as the previous case except:

- $L = 1$ m;

Natural frequencies of a slender cantilever beam in the case of lumped matrix

mode	T. theory	E-B. theory	$N = 5$	ϵ	$N = 10$	ϵ	$N = 15$	ϵ	$N = 20$	ϵ	$N = 25$	ϵ	$N = 40$
1	424, 10	419, 60	407, 61	-3, 89%	415, 42	-2, 05%	416, 90	-1, 70%	417, 43	-1, 57%	417, 67	-1, 52%	417, 93
2	2653, 70	2666, 80	2312, 78	-12, 85%	2492, 72	-6, 07%	2530, 67	-4, 64%	2544, 32	-4, 12%	2550, 71	-3, 88%	2557, 67
3	7145, 30	7387, 30	5822, 21	-18, 52%	6594, 33	-7, 71%	6777, 31	-5, 15%	6844, 66	-4, 21%	6876, 41	-3, 76%	6911, 22
4	13016, 00	14284, 00	10129, 35	-22, 18%	12030, 63	-7, 57%	12533, 58	-3, 71%	12723, 34	-2, 25%	12813, 51	-1, 56%	12912, 83
5	19645, 00	23383, 00	14531, 87	-26, 03%	18336, 10	-6, 66%	19380, 30	-1, 35%	19783, 81	0, 71%	19976, 92	1, 69%	20190, 38

Table 3.2 – Natural frequencies for a stocky cantilever beam in the case of lumped matrix

Natural frequencies of a slender cantilever beam in the case of consistent matrix

mode	T. theory	E-B. theory	$N = 5$	ϵ	$N = 10$	ϵ	$N = 15$	ϵ	$N = 20$	ϵ	$N = 25$	ϵ	$N = 40$
1	424, 10	419, 60	417, 61	-1, 53%	417, 59	-1, 53%	417, 59	-1, 53%	417, 59	-1, 53%	417, 59	-1, 53%	417, 59
2	2653, 70	2666, 80	2545, 91	-4, 06%	2542, 62	-4, 19%	2542, 13	-4, 20%	2541, 97	-4, 21%	2541, 89	-4, 21%	2541, 82
3	7145, 30	7387, 30	6892, 79	-3, 53%	6834, 67	-4, 35%	6825, 48	-4, 48%	6822, 41	-4, 52%	6821, 01	-4, 54%	6819, 52
4	13016, 00	14284, 00	13055, 60	0, 30%	12740, 53	-2, 12%	12683, 87	-2, 55%	12664, 74	-2, 70%	12656, 02	-2, 77%	12646, 68
5	19645, 00	23383, 00	20627, 01	5, 00%	20000, 20	1, 81%	19795, 30	0, 77%	19725, 07	0, 41%	19692, 94	0, 24%	19658, 42

Table 3.3 – Natural frequencies for a stocky cantilever beam in the case of consistent matrix

- $b = 2 \text{ mm}$;
- $h = 8 \text{ mm}$.

In figure 3.8 the first 6 mode shapes functions for a cantilever beam are shown.

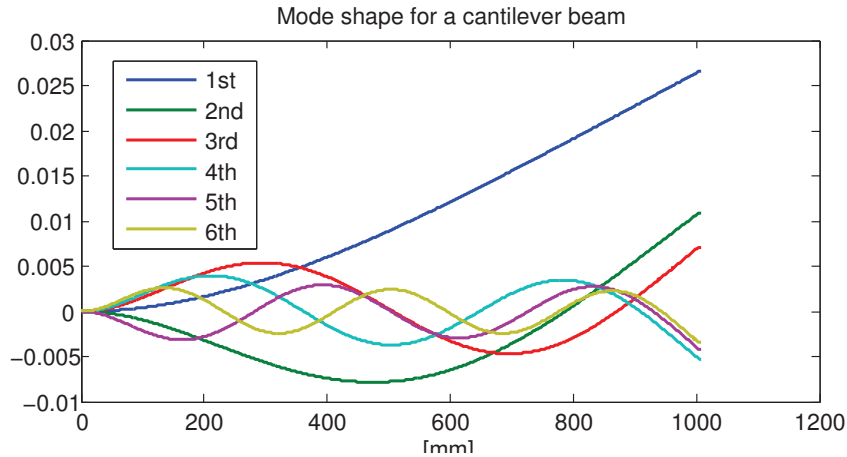


Figure 3.8 – first six modes shapes of a cantilever beam

3.6 THE RAIL PARAMETERS

Many types of rail are adopted to build railway infrastructure. The shape and the proportions are similar but they are noticeable mainly by their weight and resistance. Normally the infrastructure operators gives the standard specifications of the material and shape for all the different types of rail. This specifications are not very different in world countries. Following, we will see the most common type of Italian rails. The Italian international standard UNI EN 13674 [62] describes three rail types:

- 46E4 (correspondent to the 46UNI in the old denomination);
- 50E5 (correspondent to the 50UNI in the old denomination);
- 60E1 (correspondent to the 60UNI in the old denomination).

The 60E1 type is the most common profile for the high speed railway lines. The same profile is used in French (UIC60), in Belgium (Vign60), in German (SBBVI). In the figure 3.9 a section of this profile is shown. The rails are made of steel. The steel properties have to be in keeping with the International Organization for the Standardization (ISO 9000:2001). The material parameters are the following:

- density: $\rho_{st} = 7850 \text{ kg m}^3$;
- modulus of elasticity: $E = 2,1 \cdot 10^{11} \text{ N m}^2$;
- Poisson's modulus: $\nu = 0,3$.

Other material parameters for most common rail types are gathered in table 3.4.

60E1 (UIC60, SBBVI)

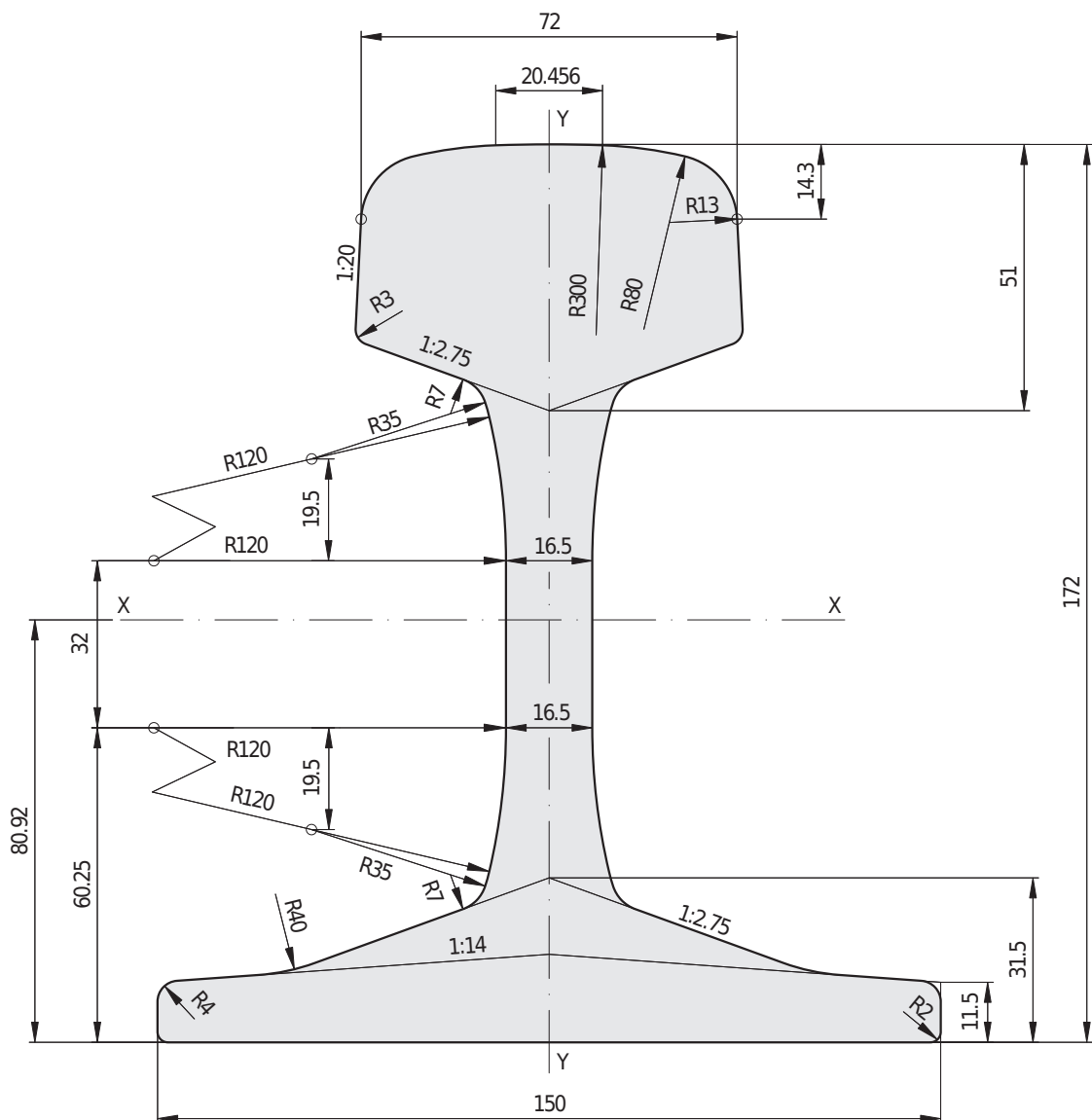


Figure 3.9 – A section of the rail type 60E1 [3]

Geometrical and material parameters for most common rail type

symbol	parameter	46E4	50E5	60E1	unit
S	transversal area	59,78	63,62	76,70	cm ²
m_r	linear mass	46,9	49,9	60,21	kg m ⁻¹
I_{xx}	moment of inertia (x-x axis)	1688	1844	3038,3	cm ⁴
I_{yy}	moment of inertia (y-y axis)	338,6	362,4	512,3	cm ⁴

Table 3.4 – most common rail type for train infrastructure

THE RAIL-PADS, SLEEPERS AND BALLAST MODEL

4.1 INTRODUCTION

Comparing mass and stiffness between rail-pads and concrete sleepers it results that rail-pad mass ($1 \sim 2$ kg) is negligible with respect to concrete sleeper mass ($250 \sim 350$ kg), and similarly sleeper stiffness ($K_s = 30 \sim 40 \cdot 10^{12} \text{ N m}^{-1}$) is six orders of magnitude bigger than pad stiffness ($15 \sim 25 \cdot 10^6 \text{ N m}^{-1}$). Moreover rail-pads should not be modeled as a punctual connection like [80, 45, 25, 51, 83], because rail-pads length cannot be neglected compared to sleeper base. So rail-pad is modeled as many spring-damper couples without mass. In accordance with [81, 25, 80, 83, 45] sleeper is modeled as a discrete rigid element and ballast is modeled as single blocks placed in correspondence of sleepers. A spring-damper couple, which represents the elasticity and viscosity of every ballast block, connects them with sleepers-elements. Also a spring-damper couple connects ballast blocks horizontally allowing the transmission of vibration in sense of train motion. Ballast stiffness is calculated according to [82],

4.2 THE RAIL-PADS MODEL

Commonly rail-pads are made from polymeric compound, rubber or composite materials. They are installed on rail seats in order to attenuate the dynamic variation of axles loads and reduce noise. In figures 4.1 two type of high-density polyethylene (HDPE) pads are shown. Due to their properties, the common scheme used to model pads is a viscous damping connection. As explained in paragraph 4.1 the mass of pads it can be neglected. A draft of pads model is shown in figure 4.2.

4.2.1 The rail-pad parameters

Rail-pad stiffness and damping properties depend on the type of rail fastening system adopted. There are many type of systems: concrete, wood or steel sleepers, ballasted or non ballasted track. In this thesis the model is developed to simulate the most common high speed railway line present in Europe. In this case, concrete sleepers and ballasted track is the usual configuration for the infrastructure. The values of stiffness and damping are given by rail-pad producers. The vertical stiffness k_p varies between 50 and 300 MN m^{-1} and the vertical damping c_p varies between 20 and 80 kNs m^{-1} . In table 4.1 some values adopted by other authors are shown. In this table also the linear weight of the rail is reported. Indeed the rail weight could be an index of the type of track (an high speed line or classical). The standard for the high speed railway lines is the rail type 60E1 (see table 3.4).

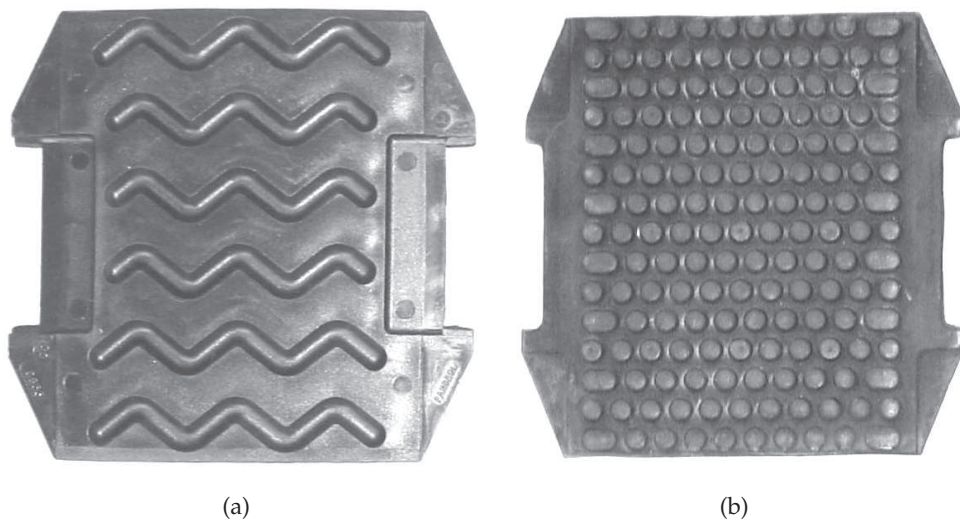


Figure 4.1 – [38] Rail pad specimens: (a) HDPE classic and (b) studded.

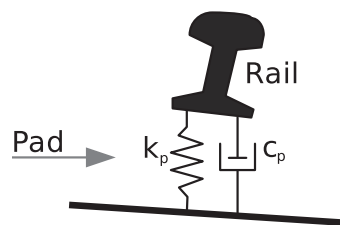


Figure 4.2 – A draft of rail pad model

Some values from bibliography								
	[42]	[42]	[80]	[80]	[25]	[80]	[45]	
m_r	50	56	56	56	56	60	60	kg m^{-1}
k_p	300	280	200	200	265	140	60	MN m^{-1}
c_p	45	63	21,8	70	40	45	46	kNs m^{-1}

Table 4.1 – Values of pad stiffness and damping used by other authors.

4.3 THE BALLAST MODEL

Track ballast forms the trackbed upon which railway sleepers are laid. It is packed between, below, and around the ties. It is typically made of crushed stone. Some authors [13, 67] studied the behavior of ballast under dynamic loads with discrete element method. A discrete element method could represents the displacement of each crushed stone giving a good description of real ballast behavior. Anyway the past models have developed simulations for few centimeters of railway line. Their study was focused to the volume of ballast around a singular sleeper. Only in this case the computational time and the complexity of the model could be reasonable to use this kind of model. Many studies [14, 56, 68, 27, 8, 9] show how the ballast vertical settlement is proportional to the elastic deflection caused by each wheel pass and the number of applied wheel loads. In this case, considering the objective of this work, the only interesting output variable is the total elastic deflection. The displacement of each crushed stone element is not required. For this reasons the ballast model made by Ahlbeck et al. [10] has been implemented in this work. Ahlbeck et al. [10] assumed that the load transmitting from sleeper to ballast coincides approximately with the cone distribution (see

figure 4.3(a)). The inclination of the cone is just the ballast stress pervasion angle corresponding to the Poisson's ratio. On the basis of this assumption, it could be concluded

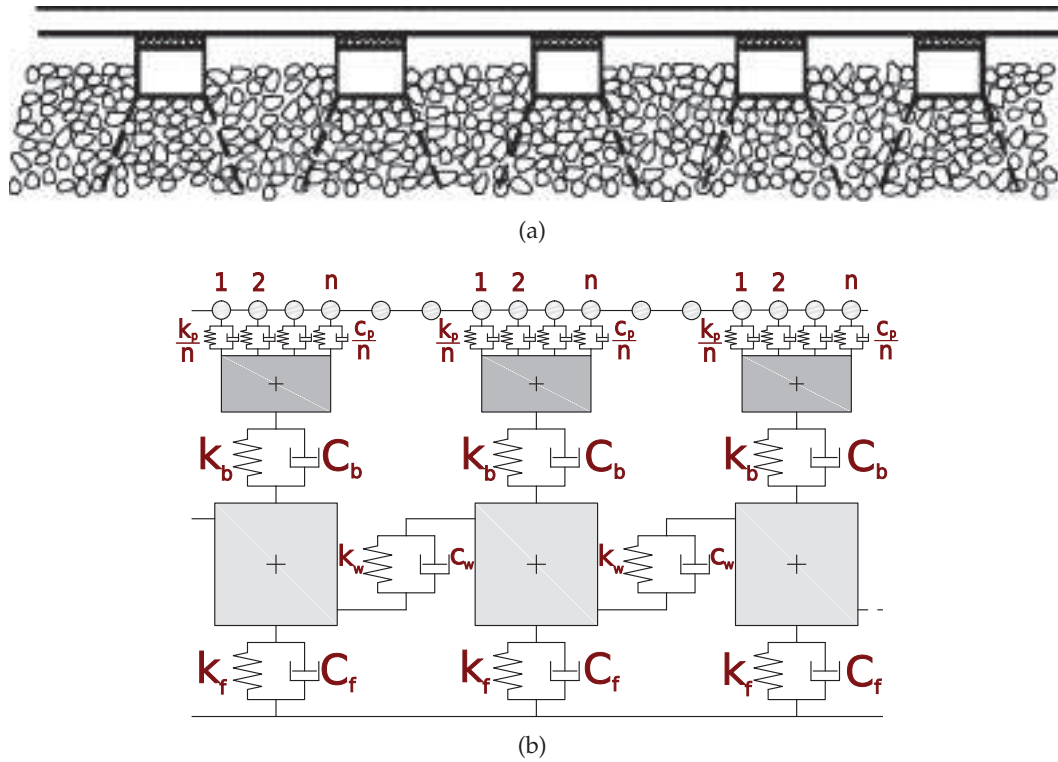


Figure 4.3 – The substructure: (a) load distribution region in continuous granular ballast [82]
(b) a draft of the substructure model.

that the vibrating part of the ballast under each sleeper is just the cone region such as shown in figure 4.3(a). Therefore, the continuous granular ballast could be modelled as a series of separate vibrating masses when analyzing the track dynamics, by which the analytical process of the ballast vibration is greatly simplified [82]. Anyway this

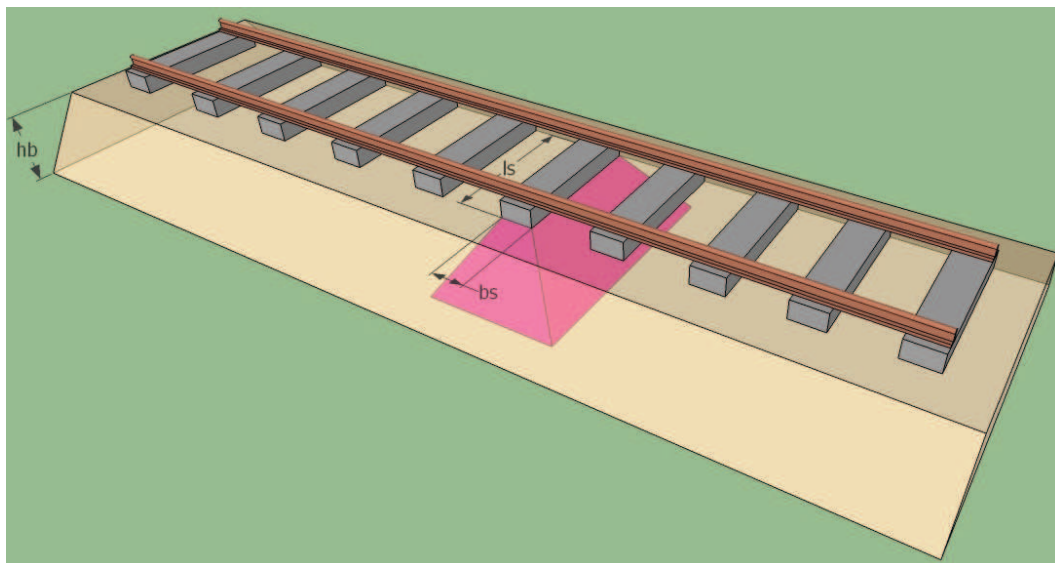


Figure 4.4 – Theoretical vibrating ballast region.

simplification results extortionate in many cases. Therefore a longitudinal connection

between ballast blocks is added to overcome this simplification (see figure 4.3(b)). This connection allows the horizontal transmission of vibrations through the ballast, giving to this part of track a shear stiffness and damping. Moreover, to represent the behavior of background a spring-damper couple is added under ballast blocks (see figure 4.3(b)).

4.3.1 The ballast parameters

In accordance with Ahlbeck et al. [10] the stiffness for a ballast block can be evaluated as:

$$k_b = \frac{2 \tan \varphi (l_s - b_s) E_b}{\ln \left[\frac{l_s (2 \tan \varphi h_b + b_s)}{b_s (2 \tan \varphi h_b + l_s)} \right]}, \quad (4.1)$$

in which:

- φ is the cone load angle of ballast;
- l_s and b_s are the dimensions of the effective contact area between ballast and sleepers (figure 4.5);
- h_b is the height of the ballast stratus (figure 4.4);
- E_b is the modulus of elasticity of the ballast.

In the following table 4.2 values of k_b and c_b adopted by other authors are shown. The

Some values from bibliography								
	[42]	[42]	[80]	[80]	[25]	[80]	[45]	
m_r	50	56	56	56	56	60	60	kg
k_b	100	70	31,6	29,1	240	29,1	15	MN m ⁻¹
c_b	72	82	21,8	47	58,8	47	9	kNs m ⁻¹

Table 4.2 – Values of ballast stiffness and damping used by other authors.

determination of C_b is quite difficult. Some authors [82] suggest to determine the ballast damping with the results of the so-called "wheelset-dropping test", originally designed by Sato [66] in Japanese Railways (JR) and now widely use in Chinese Railways. Others authors [80] have estimated this coefficient as 40% of the critical damping coefficients, that is equivalent to fix the damping ratio as $\xi = 0.4$. Anyway looking values adopted by authors this kind of procedure overestimate the coefficient. In this work the value of c_b adopted has been found by the curve fitting method explained in paragraph 7.2. The ballast stiffness k_b calculated by equation 4.1 has been divided in half. Indeed the symmetry of problem is assumed, so the half of volume shown in figure 4.5 is considered. According to the ballast volume as shown in figure 4.5, the vibrating mass of ballast under sleeper support point could be evaluated as:

$$M_b = \rho_b h_b \left[l_s b_s + (l_s + b_s) h_b \tan(\varphi) + \frac{4}{3} h_b^2 \tan^2(\varphi) \right], \quad (4.2)$$

where ρ_b is the density of the ballast. In accordance with [80] coefficients for longitudinal springs and dampers are calculated as 30% of respective vertical coefficient.

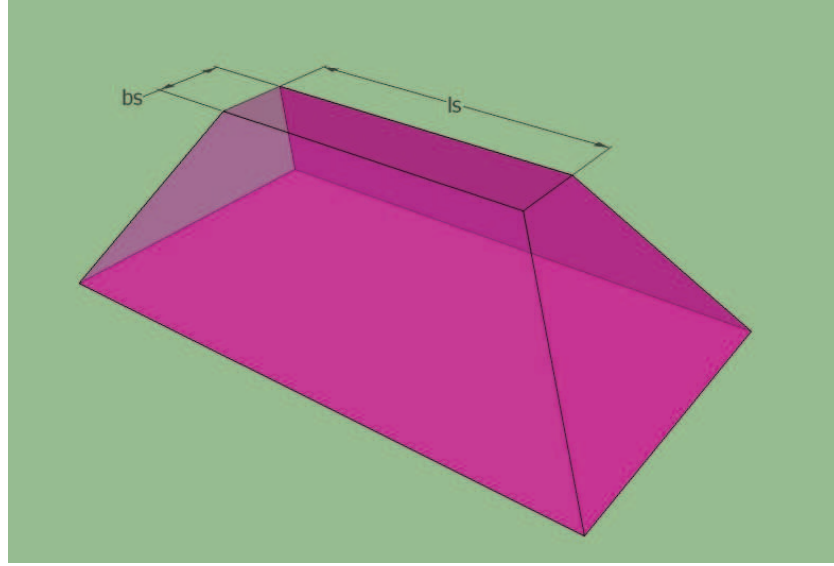


Figure 4.5 – The 3D load distribution region under a sleeper.

Similarly, in accordance to this theory [82], the subgrade stiffness could be calculated as the product of the cone base area and the modulus of subgrade:

$$k_f = [l_s + 2b_s \tan(\varphi)][b_s + 2l_s \tan(\varphi)]E_f, \quad (4.3)$$

where E_f is the K_{30} ¹ modulus of subgrade, which means the force acting on unit area that leads to unit deformation. The ballast mass M_b and the subgrade stiffness calculated by equations 4.2 and 4.3 have to be divided in half for the same reason explained for the ballast stiffness k_b .

4.4 ASSEMBLED MOTION EQUATIONS FOR THE SUBSTRUCTURE

In order to simplify resolution of track/vehicle equations system, motion equations of substructure are unified in matrix form by assembling equations of rail, sleepers and ballast blocks. The motion equation for the m^{th} sleeper (see figure 4.3(b)) is

$$m_s \ddot{z}_s + (c_b + c_p) \dot{z}_s + (k_b + k_p) z_s - c_b \dot{z}_b - k_b z_b - \frac{c_p}{n} \sum_{p=1}^n \dot{z}_r - \frac{k_p}{n} \sum_{p=1}^n z_r = m_s g; \quad (4.4)$$

the motion equation for the m^{th} ballast block is:²

$$m_b \ddot{z}_b + (2c_w + c_b + c_f) \dot{z}_b + (2k_w + k_b + k_f) z_b - c_w \dot{z}_{b_{i+1}} + \\ - c_w \dot{z}_{b_{i-1}} - k_w z_{b_{i+1}} - k_w z_{b_{i-1}} - c_b \dot{z}_s - k_b z_s = m_b g. \quad (4.5)$$

Then the equations 3.49, 4.5 and 4.4 can be written in the matrix form:

$$\mathbf{M}_{sub} \ddot{\mathbf{z}}_{sub} + \mathbf{C}_{sub} \dot{\mathbf{z}}_{sub} + \mathbf{K}_{sub} \mathbf{z}_{sub} - \mathbf{f}_{v/sub}(\mathbf{z}_v, \mathbf{z}_{sub}) = \mathbf{q}_{sub}. \quad (4.6)$$

¹The K_{30} is the subgrade reaction modulus evaluated by the plate loading test (PLT) [41]

²The equation is written considering a generic ballast block connected horizontally with next and previous block. An exception has to be done for boundary condition in which $i + 1$ and $i - 1$ terms in (4.5) are nulls.

This equation includes the rail motion equation too (equation 3.49). The term $\mathbf{f}_{sub/r}(\mathbf{z}_s)$ present in equation 3.49 is a linear function of sleeper displacements. So it can be included in substructure assembled stiffness matrix shown in equation 4.6 as shown forward (equation 4.10). Let n be the number of rail nodes and m be the number of sleepers included in the track route considered; \mathbf{M}_{sub} is the assembled mass matrix of substructure:

$$\mathbf{M}_{sub} = \begin{bmatrix} \mathbf{M}_r & \mathbf{0}_{2n \times m} & \mathbf{0}_{2n \times m} \\ \mathbf{0}_{m \times 2n} & \mathbf{M}_s & \mathbf{0}_{m \times m} \\ \mathbf{0}_{m \times 2n} & \mathbf{0}_{m \times m} & \mathbf{M}_b \end{bmatrix}_{(2n+2m) \times (2n+2m)}, \quad (4.7)$$

in which the sub-matrix \mathbf{K}_r has been defined in paragraph 3.4; \mathbf{M}_s and \mathbf{M}_b are

$$\begin{aligned} \mathbf{M}_s &= \text{diag} [m_s \ \cdots \ m_s]_{m \times m} , \\ \mathbf{M}_b &= \text{diag} [m_b \ \cdots \ m_b]_{m \times m} ; \end{aligned} \quad (4.8)$$

\mathbf{K}_{sub} is the assembled stiffness matrix of substructure:

$$\mathbf{K}_{sub} = \begin{bmatrix} \mathbf{K}_r & \mathbf{B}^T & \mathbf{0}_{2n \times m} \\ \mathbf{B} & \mathbf{K}_s & \mathbf{D} \\ \mathbf{0}_{m \times 2n} & \mathbf{D} & \mathbf{K}_b \end{bmatrix}_{(2n+2m) \times (2n+2m)}, \quad (4.9)$$

in which sub-matrices \mathbf{B} , \mathbf{K}_s , \mathbf{D} and \mathbf{K}_b are defined³ as

$$\mathbf{B} = \begin{bmatrix} -k_p & 0 & 0 & 0 & 0 & 0 & \cdots & \cdots & \cdots & 0 \\ 0 & 0 & 0 & 0 & -k_p & 0 & \cdots & \cdots & \cdots & 0 \\ 0 & 0 & 0 & 0 & 0 & 0 & \ddots & \ddots & \ddots & \vdots \\ \vdots & \vdots & \vdots & \vdots & \vdots & \vdots & \ddots & \ddots & \ddots & \vdots \\ 0 & 0 & 0 & 0 & 0 & 0 & \cdots & 0 & -k_p & 0 \end{bmatrix}_{m \times 2n}, \quad (4.10)$$

$$\begin{aligned} \mathbf{K}_s &= \text{diag} [k_b + k_p \ \cdots \ k_b + k_p]_{m \times m} , \\ \mathbf{D} &= \text{diag} [-k_b \ \cdots \ -k_b]_{m \times m} , \end{aligned} \quad (4.11)$$

$$\mathbf{K}_b = \begin{bmatrix} k'_{wbf} & -k_w & 0 & \cdots & \cdots & \cdots & 0 \\ -k_w & k_{wbf} & -k_w & 0 & \cdots & \cdots & 0 \\ 0 & -k_w & k_{wbf} & -k_w & 0 & \cdots & 0 \\ \vdots & 0 & -k_w & \ddots & \ddots & \ddots & \vdots \\ \vdots & \vdots & 0 & \ddots & \ddots & \ddots & 0 \\ \vdots & \vdots & \vdots & \ddots & \ddots & k_{wbf} & -k_w \\ 0 & 0 & 0 & \cdots & 0 & -k_w & k'_{wbf} \end{bmatrix}_{m \times m}, \quad (4.12)$$

³Sub-matrix \mathbf{B} shown in this example is written for simplicity considering only two beams between sleepers.

where $k'_{wbf} = k_w + k_b + k_f$ and $k_{wbf} = 2k_w + k_b + k_f$;

\mathbf{C}_{sub} is the assembled damping matrix written as \mathbf{K}_{sub} but substituting k terms with correspondent c terms;

\mathbf{Z}_{sub} is the assembled vector of displacements and rotations:

$$\mathbf{Z}_{sub} = \begin{bmatrix} \mathbf{z}_r \\ \mathbf{z}_s \\ \mathbf{z}_b \end{bmatrix}_{(2n+2m) \times 1}, \quad (4.13)$$

in which \mathbf{z}_s and \mathbf{z}_b are defined as

$$\begin{aligned} \mathbf{z}_s &= [z_{s_1} \quad \cdots \quad z_{s_i} \quad \cdots \quad z_{s_m}]_{m \times 1}^T, \\ \mathbf{z}_b &= [z_{b_1} \quad \cdots \quad z_{b_i} \quad \cdots \quad z_{b_m}]_{m \times 1}^T; \end{aligned} \quad (4.14)$$

\mathbf{q}_{sub} and \mathbf{f}_{sub} are the assembled forces vector:

$$\mathbf{q}_{sub} = \begin{bmatrix} \mathbf{q}_r \\ \mathbf{q}_s \\ \mathbf{q}_b \end{bmatrix}_{(2n+2m) \times 1}, \quad (4.15)$$

$$\mathbf{f}_{v/sub} = \begin{bmatrix} \mathbf{f}_{v/r} \\ \mathbf{0} \\ \mathbf{0} \end{bmatrix}_{(2n+2m) \times 1}, \quad (4.16)$$

where \mathbf{q}_s and \mathbf{q}_b are defined as

$$\mathbf{q}_s = m_s \mathbf{i}_{m \times 1}, \quad \mathbf{q}_b = m_b \mathbf{i}_{m \times 1}, \quad (4.17)$$

and $\mathbf{i}_{m \times 1}$ is a vector where all components are one. It has to be noted that only the vector $\mathbf{f}_{v/r}$ is present in equation 4.16. Indeed the vector $\mathbf{f}_{sub/r}$ present in equation 3.49 is included in the stiffness and damping matrices (see sub-matrix \mathbf{B} in equation 4.10).

5.1 INTRODUCTION

The friction and the relative motion between wheel and rail-head surfaces makes the rail head worn during train motion. A railway stands millions of wheel passes before the grinding maintenance. Additionally, its substitution is necessary only in few occasion, when major damages occur. Anyway the wear phenomenon does not appears homogeneously. It follows that the wheels meet height gradient during the motion even if the base level of the rail is perfectly horizontal. This phenomenon is well known and studied. Many models have been edited to draw up track worn profiles. In this work, three models have been used to generate track irregularities. The first one is suggested by the *EN ISO 3095 : 2004 standard* [15]. The International Organization for Standardization reports the frequency spectrum of rail irregularities. Then the roughness profile has been evaluated in 1/3 octave bands discretizing with 50 wavelengths in each band. The procedure to generate the roughness profile is described in [29]. The second model, used by American railway [45], allows to simulate the aging of track varying the grade of irregularities. In the third model an equivalent defect on the railway is used to simulate the effect of out-of-round wheels.

5.2 THE ISO 3095 MODEL

The *ISO 3095 : 2004 standard* gives the limit spectrum of rail roughness. The values in dB *re* 1 μm can be described as a logarithmic function of the center band wavelength as:

$$L_{rough}(\lambda) = 27,176 - 18,419 \log_{10} \left(\frac{\lambda_0}{\lambda} \right) \quad \text{with } \lambda > 10 \text{ mm}. \quad (5.1)$$

A graph of the function is shown in figure 5.1. The rail roughness level spectrum L_{rough} is defined by [29]:

$$L_{rough} = 10 \log_{10} \left(\frac{\tilde{r}^2}{\tilde{r}_{re}^2} \right) \quad (\text{dB re } 1 \mu\text{m}), \quad (5.2)$$

where \tilde{r}^2 is the mean square value of the roughness profile $\eta_r(x)$ evaluated in 1/3 octave bands. Then the rail roughness profile can be determined as sum of sine functions as:

$$\eta_r(x) = \sum_{i=1}^{N_d} a_i \left[\sum_{j=1}^M \sin \left(\frac{2\pi}{\lambda_{ij}} x + \phi_{ij} \right) \right], \quad (5.3)$$

Where N_d is the number of bands and M is an entire number big enough to have a good discretization. The parameter ϕ_{ij} is the mutually independent phase angle. It can

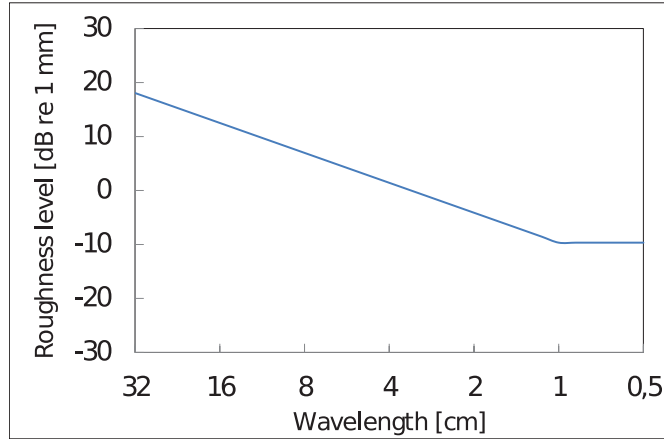


Figure 5.1 – Limit spectrum of rail roughness given by EN ISO 3095 : 2004 standard

be calculated as an uniformly random variable distributed between 0 and 2π . The M wavelengths λ_{ij} in band i are determined by assuming a constant wavenumber increment Δk_i that is function of the minimum and maximum wavelength in each band:

$$\begin{cases} \Delta k_i = \frac{2\pi}{M} \left(\frac{1}{\lambda_i^{min}} - \frac{1}{\lambda_i^{max}} \right) \\ \lambda_i^{min} = 2^{-\frac{1}{6}} \lambda_i \\ \lambda_i^{max} = 2^{\frac{1}{6}} \lambda_i \end{cases} \quad (5.4)$$

The amplitude of M sines in each band is obtained as:

$$a_i = \sqrt{\frac{2}{N_d}} 10^{\frac{L_{rough}(\lambda_i)}{20}}. \quad (5.5)$$

In order to edit a roughness profile the limit of the wavelengths have to be chosen. It can be defined λ_{lower} as the shorter wavelength and λ_{upper} as the longer. Then the related frequencies can be calculated as the ratio between train velocity and wavelengths ($f_{upper} = V/\lambda_{lower}$ and $f_{lower} = V/\lambda_{upper}$). Following the number of center wavelengths in each band has to be determined. The ratio between two consecutive bands center frequencies in 1/3 octave band is $k = \sqrt[3]{2}$ (see annex A.1), so:

$$\begin{aligned} f_{i+1} &= \sqrt[3]{2} f_i, \\ f_{i+2} &= \sqrt[3]{2} f_{i+1} = (\sqrt[3]{2})^2 f_i, \\ f_{upper} &= (\sqrt[3]{2})^{N_d} f_{lower}, \\ N_d &= \lceil 3 \log_2 \left(\frac{f_{upper}}{f_{lower}} \right) \rceil. \end{aligned} \quad (5.6)$$

Then all the bands center frequencies are:

$$f_i = (\sqrt[3]{2})^i f_{lower} \quad \text{for } i = 1, 2, \dots, N_d. \quad (5.7)$$

Once all wavelengths λ_i are calculated too ($\lambda_i = V/f_i$), the roughness level can be calculated by the equation 5.1. Then the amplitude in each band is calculated by the

equation 5.5. Finally the rail roughness profile can be edited by equation 5.3. The steps of the procedure are resumed here:

- fixate the upper and lower wavelength of defects: $\lambda_{upper}, \lambda_{lower}$;
- fixate the number of band discretization M ;
- calculate the number of bands center frequencies with equation 5.6;
- calculate the value of every frequency by equation 5.7 (and then λ_i);
- calculate the roughness level by mean of *ISO 3095 standard* for each band by equation 5.1;
- for each band i calculate the limit wavelengths λ_i^{min} and λ_i^{max} by equation 5.4;
- for each band i calculate all discretizing wavelengths λ_{ij} by equation 5.4;
- for each band i edit M ϕ_{ij} random variable uniformly distributed between 0 and 2π ;
- calculate the defects amplitude for each band by equation 5.5;
- edit the roughness profile by equation 5.3.

5.3 THE AMERICA RAILWAY STANDARD MODEL

The value of vertical defect in accordance with Lei and N.A. Noda [45], can be written as

$$\begin{aligned}\eta_r(t) &= \sum_{k=1}^{N_{d2}} a_k \sin(\omega_k t + \phi_k) \\ \eta_r(x) &= \sum_{k=1}^{N_{d2}} a_k \sin\left(\omega_k \frac{V}{x} + \phi_k\right),\end{aligned}\tag{5.8}$$

where a_k is a Gaussian random variable with expectation zero and variance σ_k , ϕ_k is a random variable with uniformity distribution in $0 - 2\pi$ range, V is the train speed and N_{d2} is the number of defect functions. In this work these values are generated with the Cristoforo Colombo random number generator. Pulsation for every sinusoidal function is

$$\omega_k = \omega_l + (k - 1)\Delta\omega, \quad k = 1, 2, \dots, N_{d2};\tag{5.9}$$

with

$$\Delta\omega = \frac{\omega_u - \omega_l}{N_{d2} - 1}.\tag{5.10}$$

The method requires the range of wavelengths, or the range of pulsation (upper pulsation ω_u , lower pulsation ω_l)¹, to be given, and the number of sinusoidal function N_{d2} has to be fixed. America Railway Standard gives the power spectral density $S(\omega)$ for six line grades of railway tracks (from worst line to best line). It is

$$S(\omega) = \frac{0.25 A_v \omega_c^2}{(\omega^2 + \omega_c^2) \omega^2},\tag{5.11}$$

¹If the train speed is constant, the pulsation can be calculated as function of the wavelength.

where A_v and ω_c are defined in table 5.1.

Coefficients for A_v and ω_c		
I_{gl} Line grade	A_v (cm ² rad m ⁻¹)	ω_c (rad m ⁻¹)
1	1.2107	0.8245
2	1.0181	0.8245
3	0.6816	0.8245
4	0.5376	0.8245
5	0.2095	0.8245
6	0.0339	0.8245

Table 5.1 – Coefficients taken from American Railway Standard [45].

Once the power spectral density function is defined, the variance σ_k can be calculated as

$$\sigma_k^2 = 4S(\omega_k)\Delta\omega, \quad k = 1, 2, \dots, N_{d2}. \tag{5.12}$$

5.4 THE RAIL EQUIVALENT CORRUGATION IN THE CASE OF OUT-OF-ROUND WHEELS

Sometimes, when a sudden braking occurs, the wheels slide over the railway head for many meters. The sliding generates a big increment of friction in a limited zone of wheels. This phenomenon causes sever wear of the part of the wheel in contact with the rail, leading to the formation of a “wheel flat”. Then these wheels continue to move on railway rotating. An impulsive increment of dynamic contact force occurs when wheel flats meet railway head during wheel rotation. This increment can be very conspicuous if the wheel flat is large (up to about 100 mm) and the height of wear is a big value. For this reason this phenomenon has been studied by many authors. In this work a study of the wheel-flat effects has been carried out. A draft of an idealized flat is shown in figure 5.2, As shown in figure 5.2 an idealized flat can be identified by his depth d and

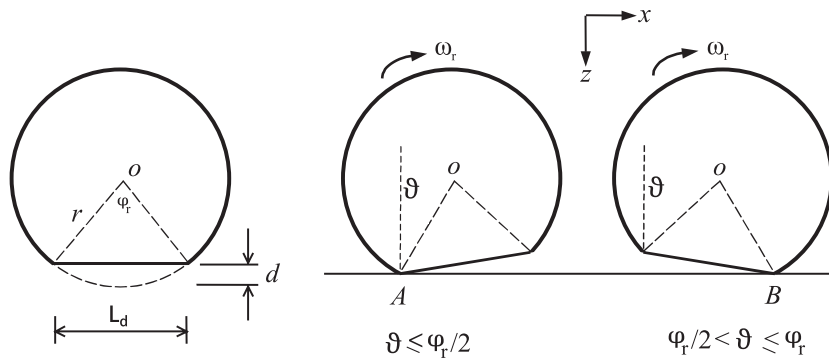


Figure 5.2 – Rolling of a wheel with an idealized flat [77].

his length l . If r is the radius of the wheels, d and l are related by $d \approx l^2/(8r)$. A perfect wheel moving on an equivalent defect railway can be used to simplify the model. The effects on the models will be the same. The following irregularity profile can be used [77, 80]:

$$z_p(x_p) = \frac{d}{2} \left[1 - \cos \left(2\pi \frac{x_p}{l} \right) \right], \tag{5.13}$$

where x_p is the longitudinal position of the contact point. The position of contact point is not the same of the wheel center (see figure 5.3).

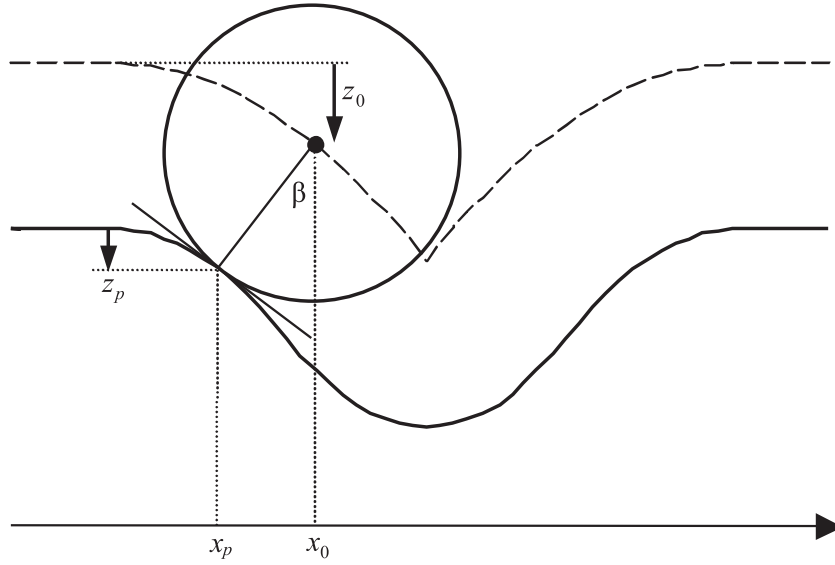


Figure 5.3 – Difference between center and contact point position [77].

The vertical position can be calculated as:

$$z_0(x_0) = z_p(x_p) + r(1 - \cos\beta), \quad (5.14)$$

where x_0 is the longitudinal position of the wheel center and x_p is the longitudinal position of the contact point. They are related by:

$$x_0 = x_p + r \sin\beta. \quad (5.15)$$

where β is the arctangent of the derivative of z_p in the point x_p as:

$$\beta = \arctan \frac{\partial z_p(x_p)}{\partial x_p} \approx \frac{\partial z_p(x_p)}{\partial x_p} = \frac{\pi d}{l} \sin\left(2\pi \frac{x_p}{l}\right). \quad (5.16)$$

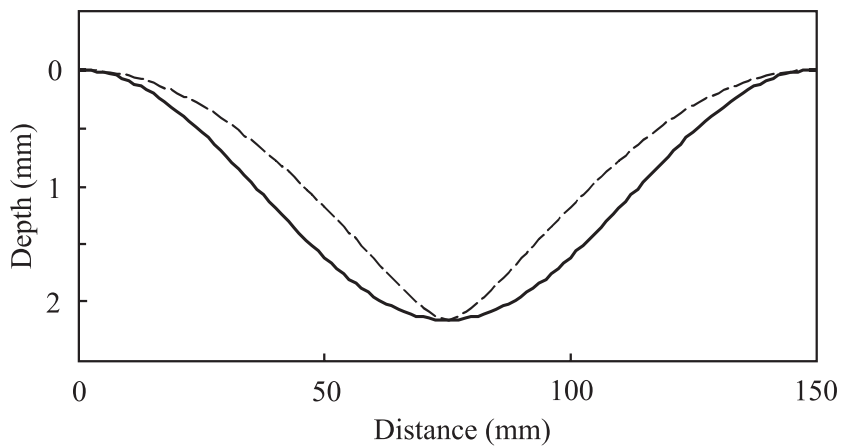


Figure 5.4 – Wheel flat geometry from equation 5.13, $r = 460\text{mm}$, $d = 2,15\text{mm}$ and $l = 150\text{mm}$; continuous line: irregularity on the railhead, dashed line: wheel center trajectory.

In figure 5.4 both functions (the railhead corrugation and the wheel center trajectory) are shown.

SOLVING EQUATIONS

6

6.1 INTRODUCTION

In the previous chapters the physic model has been resumed in two equations: one for the vehicle (Equation 2.2) and one for the substructure (Equation 4.6). To simplify the reading of this work these Equations are reported here:

$$\mathbf{M}_v \ddot{\mathbf{z}}_v + \mathbf{C}_v \dot{\mathbf{z}}_v + \mathbf{K}_v \mathbf{z}_v - \mathbf{f}_{sub/v}(\mathbf{z}_v, \mathbf{z}_{sub}) = \mathbf{q}_v, \quad (6.1)$$

$$\mathbf{M}_{sub} \ddot{\mathbf{z}}_{sub} + \mathbf{C}_{sub} \dot{\mathbf{z}}_{sub} + \mathbf{K}_{sub} \mathbf{z}_{sub} - \mathbf{f}_{v/sub}(\mathbf{z}_v, \mathbf{z}_{sub}) = \mathbf{q}_{sub}. \quad (6.2)$$

The system is non linear because the term $\mathbf{f}_{sub/v}(\mathbf{z}_v, \mathbf{z}_{sub})$, present in both vector equations, contains the contact force evaluated by Hertz's theory (see paragraph 2.4). During simulation, the train moves along the track with a fixed velocity. It's also assumed that the railway is straight in absence of curves. The first vector Equation 6.1 has the fixed dimension of 10 DOF. The dimension of second equation depends of the length of railway track, and the precision adopted for the discretization in the FE rail model. In this chapter two method of resolution are shown. The first one is the classical Newton Raphson method. This method and the model are shown in a paper published during the thesis [23, 24]. The second method proposed in this work consists in an particular algorithm that combines a fixed point and a Newton Raphson method. The algorithm of resolution has been programmed with the software MATLAB[®]. An user-friendly interface has been designed to allow a more simple use of the tool (see figure 6.4).

6.2 THE DISCRETIZATION

The space discretization has been done with the DEM and FEM (see chapters 2, 3 and 4). The Finite Difference Method (FDM) has been used for the time discretization. Displacements and speeds have been written as function of accelerations by the linear acceleration method (Newmark scheme with $\delta = 1/2$ and $\theta = 1/6$).

$$\begin{cases} \dot{\mathbf{z}}_{i+1} = \dot{\mathbf{z}}_i + \frac{\Delta t}{2} (\ddot{\mathbf{z}}_{i+1} + \ddot{\mathbf{z}}_i) \\ \mathbf{z}_{i+1} = \mathbf{z}_i + \Delta t \dot{\mathbf{z}}_i + \frac{\Delta t^2}{6} (\ddot{\mathbf{z}}_{i+1} + 2\ddot{\mathbf{z}}_i) \end{cases}, \quad (6.3)$$

where variables at i^{th} time-step are knowns. Then the vector equations for the vehicle and for the substructure can be rewritten in the discrete form:

$$\mathbf{F}_v(\ddot{\mathbf{z}}_{v,i+1}) = \mathbf{A}_v \ddot{\mathbf{z}}_{v,i+1} + \mathbf{f}_{v,i+1}(\ddot{\mathbf{z}}_{v,i+1}, \ddot{\mathbf{z}}_{sub,i+1}) - \mathbf{b}_{v,i} = \mathbf{0} \quad (6.4a)$$

$$\mathbf{F}_{sub}(\ddot{\mathbf{z}}_{sub,i+1}) = \mathbf{A}_{sub} \ddot{\mathbf{z}}_{sub,i+1} + \mathbf{f}_{sub,i+1}(\ddot{\mathbf{z}}_{v,i+1}, \ddot{\mathbf{z}}_{sub,i+1}) - \mathbf{b}_{sub,i} = \mathbf{0} \quad (6.4b)$$

where

$$\begin{aligned} \mathbf{A}_\alpha &= \left(\mathbf{M}_\alpha + \frac{\Delta t}{2} \mathbf{C}_\alpha + \frac{\Delta t^2}{6} \mathbf{K}_\alpha \right), \\ \mathbf{b}_{\alpha,i} &= \left[\mathbf{q}_\alpha - \mathbf{C}_\alpha \left(\dot{\mathbf{z}}_{\alpha,i} + \frac{\Delta t}{2} \ddot{\mathbf{z}}_{\alpha,i} \right) - \mathbf{K}_\alpha \left(\mathbf{z}_{\alpha,i} + \Delta t \dot{\mathbf{z}}_{\alpha,i} + \frac{\Delta t^2}{3} \ddot{\mathbf{z}}_{\alpha,i} \right) \right], \end{aligned} \quad (6.5)$$

for $\alpha = v$ or *sub*. These two systems of equations are coupled by the contact vector. Indeed, the contact forces $R_{r/w}$ are inside both of the vectors $\mathbf{f}_{v,i+1}$ and $\mathbf{f}_{sub,i+1}$ with opposite signs.

6.3 FIRST METHOD OF RESOLUTION

6.3.1 The Newton-Raphson method

As the forces vector, in both of the equations 6.4a and 6.4b, is a non linear function of accelerations, it can be possible to solve the non linear system with the Newton-Raphson iterative method. A singular vector equation that includes both equations for vehicle and substructure can be written:

$$\mathbf{F}(\ddot{\mathbf{z}}_{i+1}) = \mathbf{A}\ddot{\mathbf{z}}_{i+1} + \mathbf{f}_{i+1}(\ddot{\mathbf{z}}_{i+1}, \ddot{\mathbf{z}}_{i+1}) - \mathbf{b}_i = \mathbf{0} \quad (6.6)$$

where \mathbf{f}_{i+1} is:

$$\mathbf{f}_{i+1} = \begin{bmatrix} -\mathbf{f}_{sub/v}(\ddot{\mathbf{z}}_{v,i+1}, \ddot{\mathbf{z}}_{sub,i+1}) \\ -\mathbf{f}_{v/sub}(\ddot{\mathbf{z}}_{v,i+1}, \ddot{\mathbf{z}}_{sub,i+1}) \end{bmatrix}. \quad (6.7)$$

The number of equations in 6.6 is $n_{eq} = 10 + 2n + 2m$, where 10 is the number of degrees of freedom of the vehicle, n is the number of rail nodes and m is the number of sleepers included in the route considered. To simplify the calculation of Jacobian, it can be useful to separate it in two terms. Looking the equation 6.6 the Jacobian of three terms have to be calculated. The first term is $\mathbf{A}\ddot{\mathbf{z}}_{i+1}$. This is a linear function of the accelerations so the first Jacobian term is $\mathbf{J}_1 = \mathbf{A}$. The second term is $\mathbf{f}_{i+1}(\ddot{\mathbf{z}}_{i+1}, \ddot{\mathbf{z}}_{i+1})$. This term contains the Hertz contact forces. As seen in paragraph 2.4, contact forces are not a linear function of displacements and consequently neither of accelerations. The calculation of the Jacobian of this term will be shown in next paragraph 6.3.2. Finally the Jacobian of the third term (\mathbf{b}_i) is null. The Jacobian connected to the system of equations 6.6 is:

$$\mathbf{J}(\ddot{\mathbf{z}}_{i+1}^k) = \mathbf{A} + \begin{bmatrix} \mathbf{0}_{6 \times 6} & \mathbf{0}_{6 \times (4+2n)} & \mathbf{0}_{6 \times 2m} \\ \mathbf{0}_{(4+2n) \times 6} & \mathbf{R}(\ddot{\mathbf{z}}_{i+1}^k)_{(4+2n) \times (4+2n)} & \mathbf{0}_{(4+2n) \times 2m} \\ \mathbf{0}_{2m \times 6} & \mathbf{0}_{2m \times (4+2n)} & \mathbf{0}_{2m \times 2m} \end{bmatrix}, \quad (6.8)$$

where $\mathbf{R}(\ddot{\mathbf{z}}_{i+1}^k)_{(4+2n) \times (4+2n)}$ is a matrix which contains the derivatives of the components of the vector \mathbf{f}_{i+1} with respect to accelerations. The component at the line l and the column c is:

$$R_{l,c} = \frac{\partial f_{l+6}}{\partial \ddot{z}_{i+1,c+6}}, \quad 1 \leq l \leq (4+2n), \quad 1 \leq c \leq (4+2n). \quad (6.9)$$

Once the Jacobian is defined, the solution $\ddot{\mathbf{z}}_{i+1}$ can be calculated as limit of the sequence

$$\mathbf{J}(\ddot{\mathbf{z}}_{i+1}^k)(\ddot{\mathbf{z}}_{i+1}^{k+1} - \ddot{\mathbf{z}}_{i+1}^k) = -\mathbf{F}(\ddot{\mathbf{z}}_{i+1}^k), \quad (6.10)$$

where the superscript k is relative to the k^{th} Raphson iteration and subscript i is relative to the i^{th} time-step.

6.3.2 The derivation of the R matrix components to evaluate the Jacobian

The terms inside the matrix \mathbf{R} depending of displacements are derivative of the contact-forces. To simplify the construction of the matrix it is possible to split it in 4 sub-matrices as:

$$\mathbf{R} = \begin{bmatrix} \mathbf{R}_{11_{4 \times 4}} & \mathbf{R}_{12_{4 \times 2n}} \\ \mathbf{R}_{21_{2n \times 4}} & \mathbf{R}_{22_{2n \times 2n}} \end{bmatrix}. \quad (6.11)$$

R_{11} and R_{12} are related to the equation of motion of wheels (Equation 2.1). R_{21} and R_{22} are related to the equation of motion of rail nodes. Moreover, the matrices R_{11} and R_{21} contain the derivative of the contact force with respect to the wheel accelerations; the matrices R_{12} and R_{22} contain the derivative of the contact force with respect to the rail nodes accelerations. As shown in Equation 2.7 the wheel/rail contact force is calculated as:

$$R_{r/wj} = \begin{cases} k_h(z_{wj} - \hat{z}_{rj} - \eta_{rj})^{\frac{3}{2}} + c_h(\dot{z}_{wj} - \dot{\hat{z}}_{rj} - \dot{\eta}_{rj}) & \text{if } \delta > 0, \\ 0 & \text{if } \delta < 0. \end{cases} \quad (6.12)$$

The derivation of R_{11} components

R_{11} is a 4×4 diagonal matrix. If l and c are respectively the generic line of the matrix and the generic column, the c^{th} term is the derivative of the contact force with respect to the c^{th} wheel acceleration as:

$$\begin{aligned} \frac{\partial \mathbf{f}_{sub/v_l}^{k,i+1}}{\partial \dot{z}_{w_c}^{k,i+1}} &= \frac{\partial R_{r/w_l}^{k,i+1}}{\partial \dot{z}_{w_c}^{k,i+1}} \\ &= k_h \frac{\Delta t^2}{4} \left(z_{w_l}^{k,i+1} - \hat{z}_{r_l}^{k,i+1} - \eta_{r_l}^{i+1} \right)^{\frac{1}{2}} + c_h \frac{\Delta t}{2}, \end{aligned} \quad (6.13)$$

with $l = c$ varying from 1 to 4; $z_{w_c}^{k,i+1}$ is the displacement at the time-step $i + 1$, at the k^{th} Newton iteration, of the c^{th} wheel; the displacements $z^{k,i+1}$ ($\dot{z}^{k,i+1}$, z^i) at the time-step $i + 1$ at the k^{th} Newton iteration are calculated with Equations 6.3. The rail corrugation function η_r doesn't varies in k -iterations.

The derivation of R_{12} components

The components of this matrix contain the derivatives of contact force with respect to the accelerations corresponding to c^{th} DOF of the rail (if c is the generic column of the matrix). R_{12} is a $4 \times 2n$ matrix. Each line corresponds to each wheel and each column to each DOF of the rail nodes. In each line the contact force is present only in the rail DOF corresponding to the beam where the contact wheel/rail occurs. The the lc -terms of the matrix is:

$$\begin{aligned} \frac{\partial \mathbf{f}_{sub/v_l}^{k,i+1}}{\partial \dot{z}_{r_c}^{k,i+1}} &= \frac{3}{2} k_h (z_{w_l}^{k,i+1} - \hat{z}_{r_l}^{k,i+1} - \eta_{r_l}^{i+1})^{\frac{1}{2}} \frac{\partial \dot{z}_{r_l}^{k,i+1}}{\partial \dot{z}_{r_c}^{k,i+1}} \\ &= \frac{3}{2} k_h (z_{w_l}^{k,i+1} - \hat{z}_{r_l}^{k,i+1} - \eta_{r_l}^{i+1})^{\frac{1}{2}} \frac{\partial \dot{z}_{r_l}^{k,i+1}}{\partial \dot{z}_{r_c}^{k,i+1}} \frac{\partial \dot{z}_{r_c}^{k,i+1}}{\partial \dot{z}_{r_c}^{k,i+1}} \\ &= \frac{3}{2} k_h (z_{w_l}^{k,i+1} - \hat{z}_{r_l}^{k,i+1} - \eta_{r_l}^{i+1})^{\frac{1}{2}} \frac{\partial \dot{z}_{r_l}^{k,i+1}}{\partial \dot{z}_{r_c}^{k,i+1}} \frac{\Delta t^2}{6} \\ &= \frac{\Delta t^2}{4} k_h (z_{w_l}^{k,i+1} - \hat{z}_{r_l}^{k,i+1} - \eta_{r_l}^{i+1})^{\frac{1}{2}} n_c^{i+1}; \end{aligned} \quad (6.14)$$

where $\hat{z}_{r_l}^{k,i+1}$ is the rail displacement at the l^{th} contact-point and $z_{r_c}^{k,i+1}$ is the c^{th} DOF of the rail (a displacement or a rotation). The derivative of displacement with respect to acceleration is (from 6.3):

$$\frac{\partial z_{r_c}^{k,i+1}}{\partial \ddot{z}_{r_c}^{k,i+1}} = \frac{\Delta t^2}{6}, \quad (6.15)$$

and the derivative of the vertical displacement of the contact point $\hat{z}_{r_l}^{k,i+1}$ with respect to the c^{th} DOF of the rail $z_{r_c}^{k,i+1}$ corresponds to the shape function n_c^{i+1} .

The derivation of R_{21} components

The components of this matrix contains the derivatives of local forces vector (Equations 3.41) with respect to the wheel displacements. R_{21} is a $2n \times 4$ matrix. In each column the contact force is present only in the the rail nodes corresponding to the beam where the contact occurs. The derivative of the term for the generic term of the matrix is:

$$\begin{aligned} -\frac{\partial \mathbf{f}_{v/sub_l}^{k,i+1}}{\partial \ddot{z}_{w_c}^{k,i+1}} &= -n_l^{i+1} \frac{\partial R_{w/r_c}^{k,i+1}}{\partial \ddot{z}_{w_c}^{k,i+1}} \\ &= -n_l^{i+1} \left[k_h \frac{\Delta t^2}{4} \left(z_{w_c}^{k,i+1} - \hat{z}_{r_c}^{k,i+1} - \eta_{r_c}^{i+1} \right)^{\frac{1}{2}} + c_h \frac{\Delta t}{2} \right], \end{aligned} \quad (6.16)$$

The derivation of R_{22} components

The components of this matrix contains the derivatives of local forces vector (Equations 3.41) with respect to the nodes accelerations. R_{22} is a $2n \times 2n$ matrix. In each line the j^{th} contact force to derivate is the $R_{w/r_j}^{k,i+1}$ connected to the $[l/2]^{th}$ beam. The term is present only in the the DOF where the contact occurs. The derivative of the term for the generic term of the matrix is:

$$\begin{aligned} -\frac{\partial \mathbf{f}_{v/sub_l}^{k,i+1}}{\partial \ddot{z}_{r_c}^{k,i+1}} &= -n_l^{i+1} n_c^{i+1} \frac{\partial R_{w/r_j}^{k,i+1}}{\partial \ddot{z}_{r_c}^{k,i+1}} \\ &= -n_l^{i+1} n_c^{i+1} \left[k_h \frac{\Delta t^2}{4} \left(z_{w_j}^{k,i+1} - \hat{z}_{r_j}^{k,i+1} - \eta_{r_j}^{i+1} \right)^{\frac{1}{2}} + c_h \frac{\Delta t}{2} \right], \end{aligned} \quad (6.17)$$

where the subscript j , varying from 1 to 4, indicates which wheel is in contact with the l^{th} DOF.

6.3.3 Computational time-costs

The resolution of the problem consists to determinate the Jacobian, factorize it, and calculate the vector of displacement solving the system 6.10. This operation has to be repeated for each Newton iteration k and for each time-step i . The problem to factorize the Jacobian matrix is the step of the algorithm that requires the largest part of computational time. Both Cholesky and Lu factorization algorithm have been tested to find the most faster. The results depend principally on the length of track simulated. To improve the speed of the algorithm and allow simulations in shorter time another procedure is proposed in following paragraph.

6.4 SECOND METHOD OF RESOLUTION

6.4.1 Combination of Newton and Fixed point methods

This algorithm combines a fixed point and a Newton method to solve the non linear contact problem. At every time-step, for first fixed-point iteration, substructure equations 6.4b are solved assuming that contact forces can be calculated with Eq. (2.7); where $R_{w/r}$ is calculated as function of vehicle and substructure displacements relative to previous time-step; instead rail defects values are related to current time-step. The displacement vector of substructure, now calculated, becomes inputs for Newton-Raphson method applied to vehicle dynamic equation 6.4a. Then the non-linear contact force is calculated for every Newton-Raphson iteration, as function of vehicle displacements (with varies for every N.R.¹ iteration); substructure displacements are temporally assumed as constant.

The Jacobian related to the vehicle system (6.4a) is

$$\mathbf{J}(\ddot{\mathbf{z}}_v^{k,i+1}, \mathbf{z}_v^i, \mathbf{z}_{sub}^i) = \mathbf{A}_v + \begin{bmatrix} \mathbf{0}_{6 \times 6} & \mathbf{0}_{6 \times 4} \\ \mathbf{0}_{4 \times 6} & \mathbf{R}_{4 \times 4} \end{bmatrix}, \quad (6.18)$$

where \mathbf{R} is a diagonal matrix. Once the Jacobian \mathbf{J} is defined, the solution $\ddot{\mathbf{z}}_{i+1}$ can be calculated as limit of the sequence $\left[\ddot{\mathbf{z}}_{i+1}^k \right]_{k \in \mathbb{N}}$, where the superscript k is relative to the k^{th} N.R. iteration, such that²:

$$\mathbf{J} \left(\ddot{\mathbf{z}}_{i+1}^k \right) \left(\ddot{\mathbf{z}}_{i+1}^{k+1} - \ddot{\mathbf{z}}_{i+1}^k \right) = -\mathbf{F} \left(\ddot{\mathbf{z}}_{i+1}^k \right), \quad (6.19)$$

At the end of N.R. iterations new contact-forces and new displacements vector for the vehicle are calculated. Then new contact-forces become input for the next f.p.³ iteration. At every f.p. iteration convergence is checked on displacement vector of substructure as

$$\frac{\text{norm}(\mathbf{z}_{sub}^h - \mathbf{z}_{sub}^{h-1})}{\text{norm}(\mathbf{z}_{sub}^h)} \leq \epsilon, \quad (6.20)$$

where ϵ is the tolerance and subscript represents the j^{th} f.p. iteration. If the inequality (6.20) is satisfied, the algorithm goes to the next time-step. Similarly convergence is checked on displacement vector of vehicle to proceed in N.R. iterations.

The strong point of this algorithm consists in treating the non linearity of contact forces for every f.p. iteration applying N.R. only to the vehicle system. Indeed vehicle matrices dimensions are widely smaller than ones of substructure, so matrix factorization and system resolution result faster. Moreover, treating a part of non linearity of system vehicle leads a diminution of f.p. iterations. A global overview of the method is presented in Figure 6.1.

6.4.2 The derivation of the R matrix components to evaluate the Jacobian

In order to build the matrix \mathbf{R} , the contact-force can be rewritten in function of accelerations using the equations 6.3. So the contact force calculated at the time-step $i + 1$ for

¹Newton-Raphson.

²subscript "v" is omitted to simplify notations

³fixed-point.

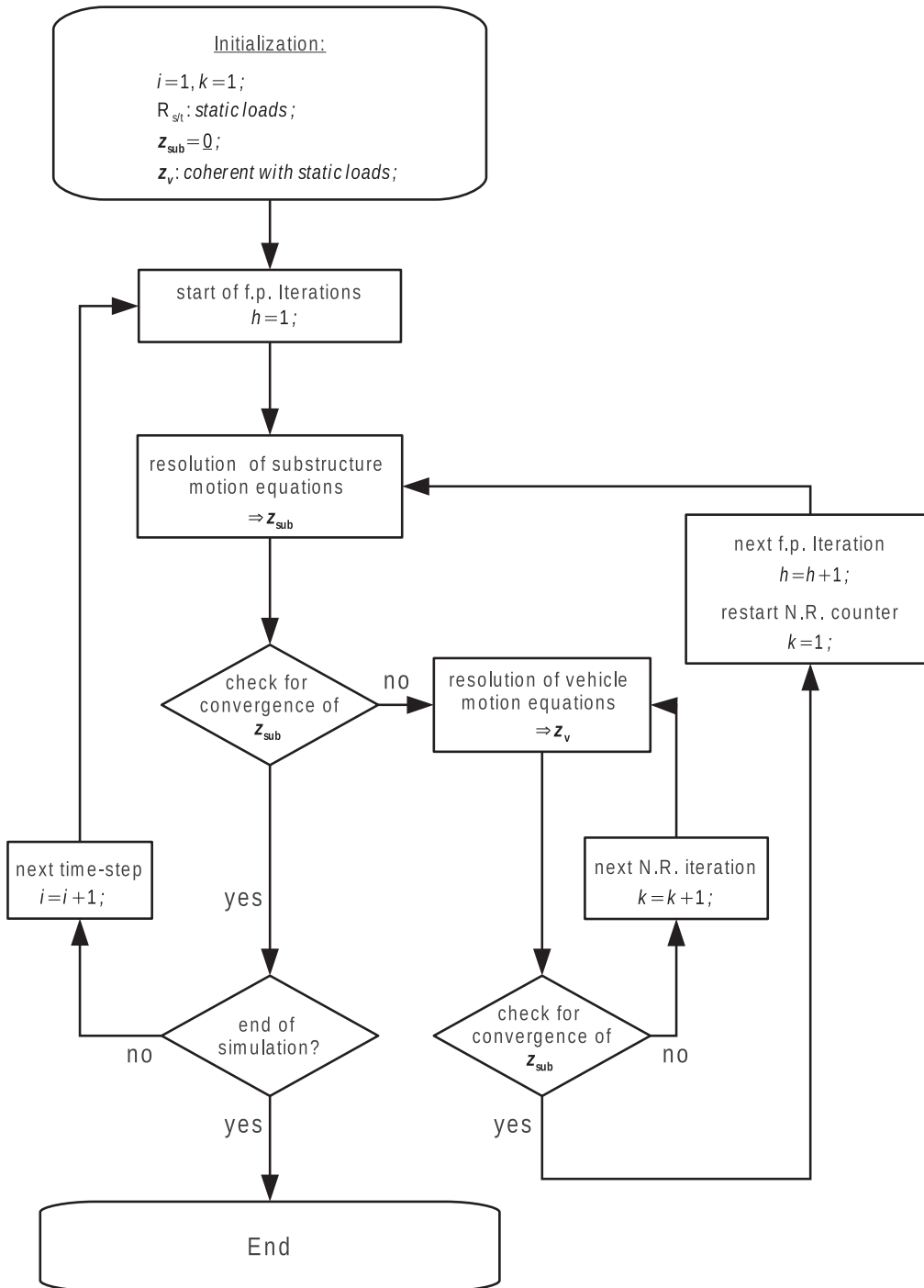


Figure 6.1 – Algorithm of resolution.

the iteration k is:

$$R_{r/w_j}^{k,i+1} = \begin{cases} k_h(z_{w_j}^i + \Delta t \dot{z}_{w_j}^i + \frac{\Delta t^2}{6} (\ddot{z}_{w_j}^{k,i+1} - 2\ddot{z}_{w_j}^i) - \dot{z}_{r_j}^{i+1} - \eta_{r_j}^{i+1})^{\frac{3}{2}} + & \text{if } \delta > 0, \\ c_h(z_{w_j}^i + \frac{\Delta t}{2} (\dot{z}_{w_j}^{k,i+1} + \dot{z}_{w_j}^i) - \dot{z}_{r_j}^{i+1} - \dot{\eta}_{r_j}^{i+1}) & \\ 0 & \text{if } \delta < 0. \end{cases} \quad (6.21)$$

If l and c are respectively the generic line of the matrix and the generic column, the diagonal elements are defined as

$$\begin{aligned} \frac{\partial \mathbf{f}_{sub/v_l}^{k,i+1}}{\partial \ddot{z}_{w_c}^{k,i+1}} &= \frac{\partial R_{r/w_l}^{k,i+1}}{\partial \ddot{z}_{w_c}^{k,i+1}} \\ &= k_h \frac{\Delta t^2}{4} \left(z_{w_l}^i + \Delta t \dot{z}_{w_l}^i + \frac{\Delta t^2}{6} (\ddot{z}_{w_l}^{k,i+1} - 2\ddot{z}_{w_l}^i) - \dot{z}_{r_l}^{k,i+1} - \eta_{r_l}^{i+1} \right)^{\frac{1}{2}} + c_h \frac{\Delta t}{2}, \end{aligned} \quad (6.22)$$

with $l = c$ varying from 1 to 4.

6.4.3 Computational time-costs

The algorithm here presented involves big advantages. Indeed in this case, Only the Jacobian matrix 10×10 has to be factorized at each k^{th} iteration and at each i^{th} time-step. The matrix A_{sub} in equations 6.4b has to be factorized only one time at the beginning of the algorithm. Then it can be stocked in memory. Moreover the problem is non linear cause of the Hertz contact-force. The non linearity is related for a half to the vehicle and for a half to the substructure (see Equation 6.12). The part of non linearity connected to the vehicle, with this method, is solved by the Newton-Raphson iterations. This fact allows to have a minor number of p.f. iterations because at every p.f. iteration the part of non linearity connected to the vehicle is resolved separately. Finally the advantages are double. First the total number of p.f. iterations results minor than in the first method. The second advantage consists in the c.p.u. computation time saved in each iteration. Indeed in this case only the 10×10 Jacobian matrix of vehicle equations has to be factorized allowing a faster computation. The model has been implemented in a first time with VBA[®] and than with MATLAB[®]. Programming languages such as VBA[®] or FORTRAN[®] could be best-performing. Anyway the speed of new algorithm proposed in paragraph 6.4 and the limited complexity of the model allowed to take advantage of the many tools included in MATLAB[®]. This fact allowed a fast programmability and a lot of advantages in the post-processing phase. The computational time for a generic simulation is shown in Figure 6.2. The simulation parameters are:

- total number of $DOF = 2498$;
- length run by train $L = 22.794$ m;
- train speed 300 km h⁻¹;
- time-step $dt = 3.6 \cdot 10^{-5}$ sec.

The total computational time has been $T = 319.987$ s. The characteristics of PC used are:

- RAM: 7.7 GiB;
- Processor: Intel Core i3-2310M CPU @ 2.10GHz x 4;
- OS: Windows 7[®] 64-bit;
- software: MATLAB[®].

The computational time in function of total number of DOF is shown in figure 6.3. In this case train speed is 160 km h^{-1} , the time-step chosen is $3.38 \cdot 10^{-5} \text{ sec}$ and the length run by train varies between 3 and 38 meters.

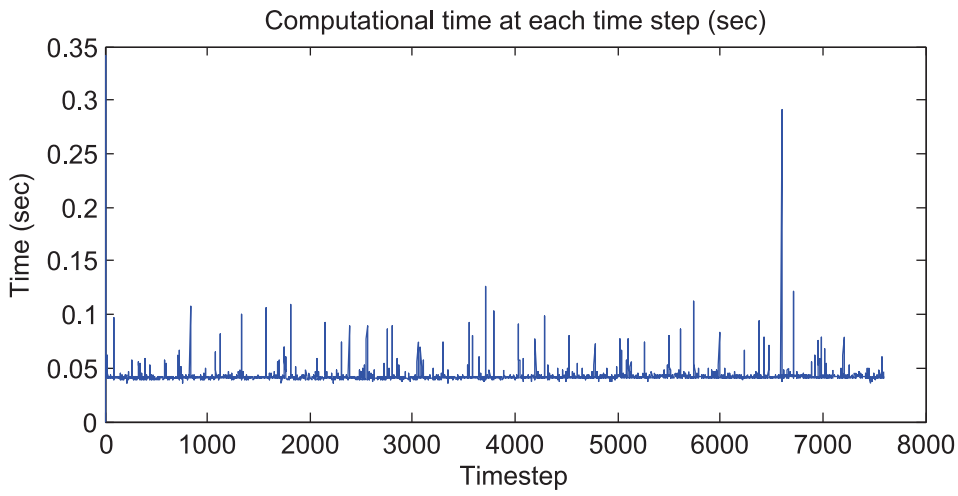


Figure 6.2 – Computational time for a generic simulation.

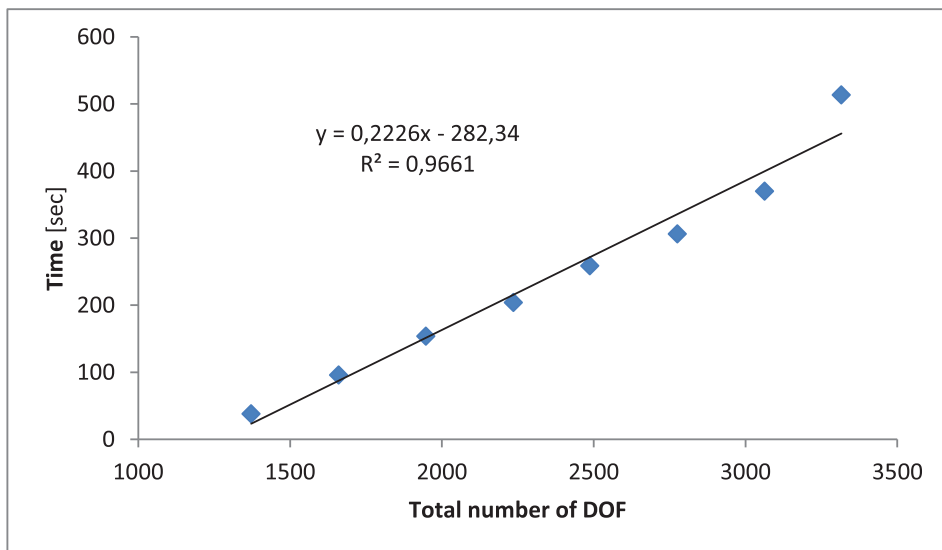


Figure 6.3 – Computational time of simulations at varying the total number of DOF.

simulation parameters

Train speed km/h

Length of simulation m

n° of steps in short

Rail parameters

UNI

weight Kg/m

I	1844e-8	m4
A	63.62e-4	m2
λ	0.34	

simulation options

NO RAILS DE...

preload time: s

rail's defects: m

n° sawing steps:

Panel

dt sec

STEP

Model options

Linear acceleration method + Newton Ra...

Newton-Raphson iteration err

Newton-Raphson iteration err

Newmark's constants

δ ≥ 0.5

α

Substructure parameters

sleeper distancy cm

n° of beam element between sleepers

sleeper mass kg

mass of a ballast element kg

parameters of rail's pseudo-random [mm]

wave lenght from to:

line damage index - best line

n° of defects random

Pad parameters

Pad width cm

n° of beam element connected to half of pad

K,C

Kp N/m Cp Ns/m

Kb N/m Cb Ns/m

Kf N/m Cf Ns/m

Kw N/m Cw Ns/m

parameters of rail defects [mm]

deterministic defects

width

wave

Locomotive

Calculate

Reset

Figure 6.4 – Interface of the software.

Part II

The Results

IN this part the results taken-out with the model presented are shown. The results of simulations have been carried out during three phases. In the first phase the simulations have been conducted taking in consideration only the substructure and exciting it with an impulsive force. This procedure has allowed to calibrate the model parameters and correct the errors present in the software. Indeed the analysis of track receptance represents the most common mean used in literature to validate the substructure model. Comparisons between experimental results and numerical data of other models have been carried out. In a second phase the vehicle has been added to the model. A check on the railway and sleeper accelerations caused by the train pass has been carried out. Also in this phase, numerical data have been compared with other models and experimental results. This phase has allowed to calibrate and correct the corrugations functions, the vehicle model, and the vehicle/substructure coupling method. The accuracy and the efficiency have been evaluated in this phase. In the third phase the speed and the sensitivity of the model have been evaluated. During this phase the treatment of data and the new results have been used to extrapolate new studies about the phenomenon of the critical speed and to develop a new formulation to evaluate the railway tolls.

THE ANALYSIS OF TRACK RECEPTANCE

7.1 INTRODUCTION

The analysis of track receptance is a good technique used by many authors to characterize the parameters of the models; for this reason receptance methods reflect the emphasis in the literature. Indeed when the transfer function is known it is relatively easy to calculate the response of the vehicle/track system to a moving irregularity [42]. It is possible to calibrate the parameters by a curve fitting technique, comparing measured and numerical calculated receptance. All measured vertical direct receptances of track are characterized by a common behavior. A first resonance is just over 100 Hz. At this frequency the sleepers and rail move on the ballast; a second is about 400 – 500 Hz, in this frequencies range the rail moves relative to the sleepers on the railpads [42]. Up to this second resonance frequency the point of excitation it is not very important. The position of the excitation point becomes really relevant around the so-called “pinned-pinned” resonance. In this frequency range (around 700 – 1000Hz) there is a resonance of the track when it is excited between sleeper and an anti-resonance when it is excited at a sleeper [42]. This resonance is very closed to the first natural frequency of a beam (with the same characteristics of the rail) with pinned-pinned boundary conditions considering the same length of the sleepers-base. Moreover for this reason the models with continuously supported track cannot represent the correct behavior in the pinned-pinned frequency range. Two type of receptance experiences are normally executed to have the correct overview of the global behavior: the vertical receptance related to a midspan excitation and the vertical receptance related to a on-sleeper excitation. In figures 7.1 and 7.2 a draft of both experiences is shown. To edit the receptance chart two

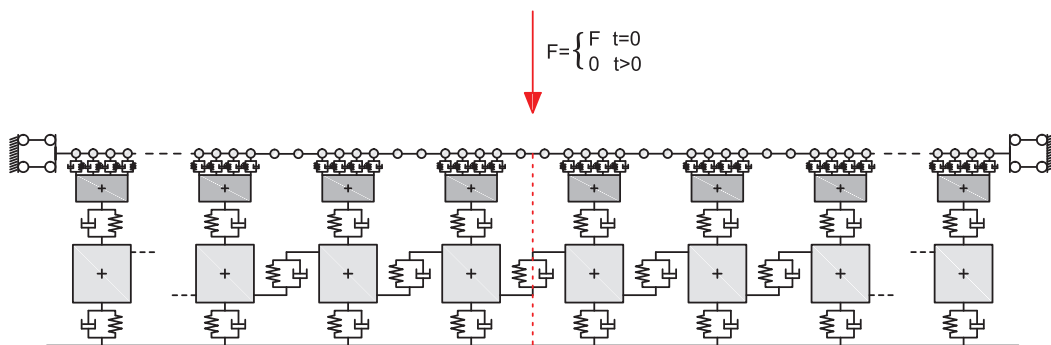


Figure 7.1 – receptance simulation: midspan excitation

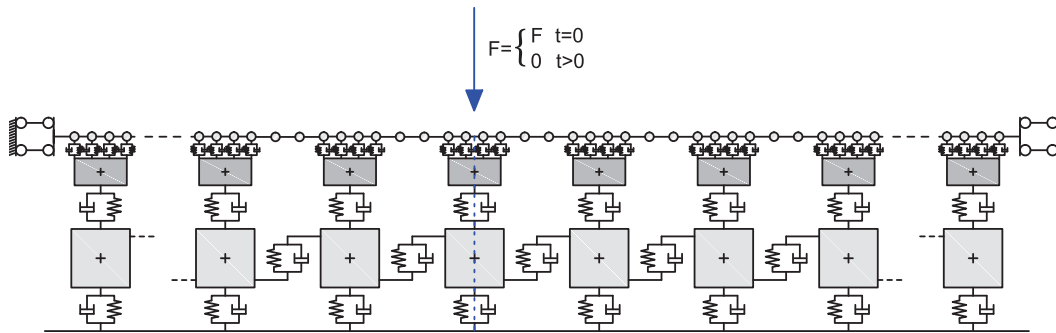


Figure 7.2 – receptance simulation: on-sleeper excitation

ways can be followed. The first way consists to excite the railhead of track with a sinusoidal load and register the displacement. Then the transfer function between the input function (excitation force) and output function (displacement) gives one point on the receptance chart. Varying the excitation frequency the receptance chart can be edited in the interested frequencies range. The second way consists to excite the track with an impulsive force. In this case the transfer function gives the results for all frequencies with one singular experience. In figure 7.3 the hammer for an impulsive excitation is shown. In figure 7.7 the waves propagation in time and in space due to a midspan excitation are shown.



Figure 7.3 – receptance experience with the impact hammer: on-sleeper excitation [18]

7.2 THE CURVE FITTING

The technique of curve fitting can be adopted to calibrate the model parameters. Not all the parameters are susceptible to a big uncertainty, indeed there are some value quite sure and not modifiable. The “sure” parameters of the track are: the linear mass and the stiffness of railway, the sleeper mass and the sleepers base. For this reason these parameters are known and they don’t play any role during the phase of curve fitting. The procedures to estimate all other parameters values have been shown in part I. Some parameters such as the ballast stiffness or the ballast damping have been estimated with procedures involving a margin of error bigger than the “sure” parameters. For this reason these parameters play a fundamental role in the phase of curve fitting. A sensitivity analysis has to be done in order to compare the measured and calculated receptances. This step allows to estimate the importance of parameters and their influence to a given output function (the receptance in this case). The parameters who influence more the

receptance of track are: The ballast stiffness k_b and damping c_b , the railpads stiffness k_p and damping c_p , the linear mass of rail m_r and the rail bending stiffness $kr = EI$. Varying these parameters the receptance changes with particular behaviors. Looking at figure 7.4 the influence of more important parameters is evident. The ballast stiff-

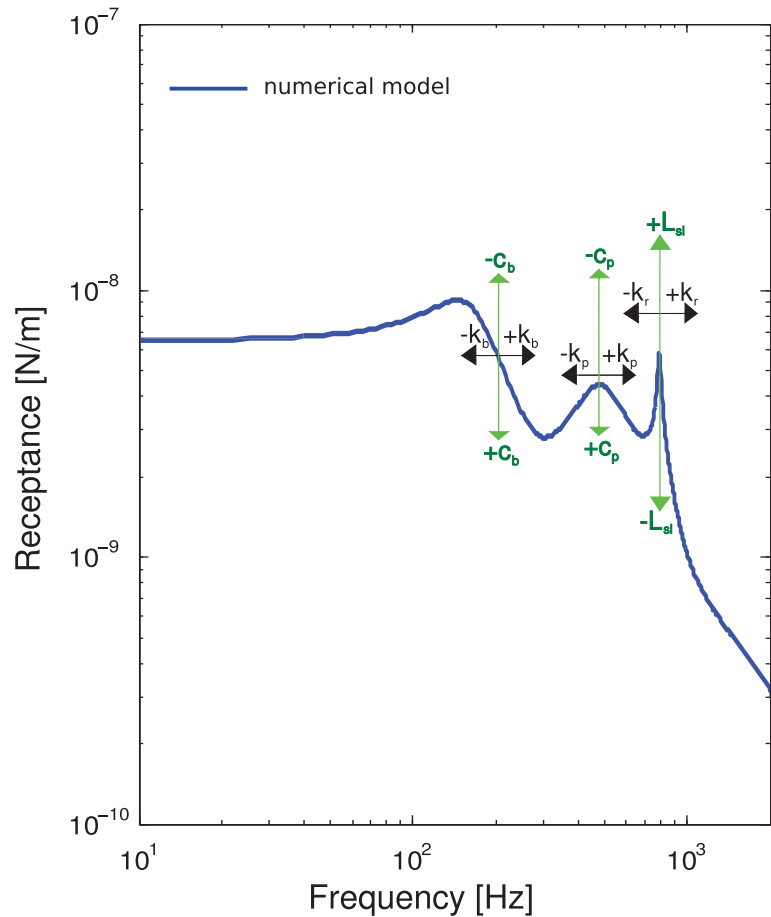


Figure 7.4 – The influence of the more important parameters to the receptance chart

ness, if incremented, moves the lowest resonance in the higher frequencies way. The same behavior is caused by the pad stiffness to the second resonance. The rail bending stiffness produces the same effect too. Anyway this parameter is quite sure, being the bending stiffness proportional to the elastic modulus of steel and the inertial modulus of rail section ("sure" values). The ordinates in the receptance chart are proportional to the vertical displacement. For this reason the ballast and the pad damping move the resonance peaks up and down with inverse proportion. Another important parameter is the sleeper base. Indeed the "pinned-pinned" resonance increases if the sleeper base increases too. This fact deserves some details. The sleepers base is a parameter known and fixed and it cannot be changed during the phase of calibration. Anyway, more exactly, the vertical displacement at midspan point is proportional to the length of rail not supported by pads but suspended between the internal faces of two consecutive sleepers. This is one of the reason why present model is more accurate than past models. Indeed, as seen in paragraph 3.3 the length of rail between sleepers, allowing a free vertical displacement in the connection-point model, is longer than reality. For this reason the connection-point model over-estimates the receptance at the pinned-pinned frequency. The present model, with the hypothesis of connection-area fits really better this value.

7.3 THE IMPORTANCE OF THE CONNECTION-AREA MODEL

In figures 7.5 and 7.6 the comparison between present model and experimental data by Knothe and Grassie [42] is shown. To show the importance of the connection-area model, the numerical results in the case of connection-point hypothesis is included too. The connection-point model produces errors especially in the range of the pinned-pinned frequency. In this frequency range, it overestimates the receptance by 402% in the case of midspan excitation. Additionally, in the case of on-sleeper excitation, the receptance is underestimated by the 149%. On the contrary the connection-area model fits very well the experimental data. All the parameters used in the simulation are reported in table 7.1.

Table 7.1 – Model parameters adopted for evaluation of railway receptance.

notation	parameter	value	unit
Model parameters of substructure			
E	young modulus of rail	$2.07 \cdot 10^{11}$	Nm^{-1}
I	inertial modulus of rail ^a	$2348 \cdot 10^{-8}$	m^4
A	section area of rail	$71.7 \cdot 10^{-4}$	m^2
χ	Timoshenko shear coefficient ^a	0.34	
m_r	railway mass ^a (per unit length)	56	kg m^{-1}
M_s	sleeper mass ^a	220	kg
k_p	pad stiffness ^a	$280 \cdot 10^6$	Nm^{-1}
c_p	pad damping ^b	$35 \cdot 10^3$	Ns m^{-1}
k_b	ballast stiffness ^b	$160 \cdot 10^6$	Nm^{-1}
c_b	ballast damping ^b	$90 \cdot 10^3$	Ns m^{-1}
l_{sl}	sleeper base ^a	69.8	cm
Other simulation parameters			
n_{ms}	number of sleepers (midspan excitation)	99	
n_{os}	number of sleepers (on-sleeper excitation)	100	
dt	time step	$3.37 \cdot 10^{-5}$	s
n	number of pad elements	8	
d	number of beam elements between sleepers	10	

^a Values extracted form [42]

^b estimated Values

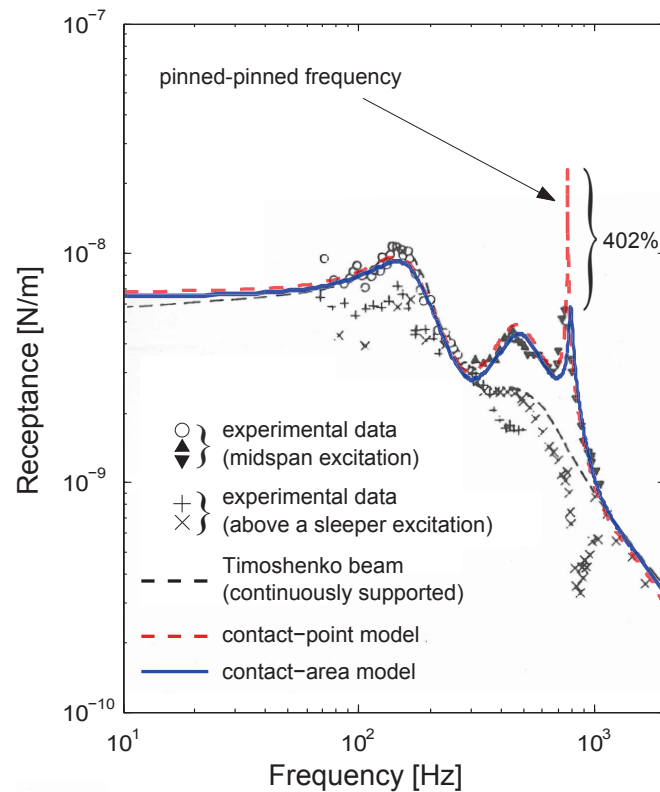


Figure 7.5 – Comparison between receptances of the railway in the case of: the connection-point model, the connection-area model and experimental data [42]; case of midspan excitation.

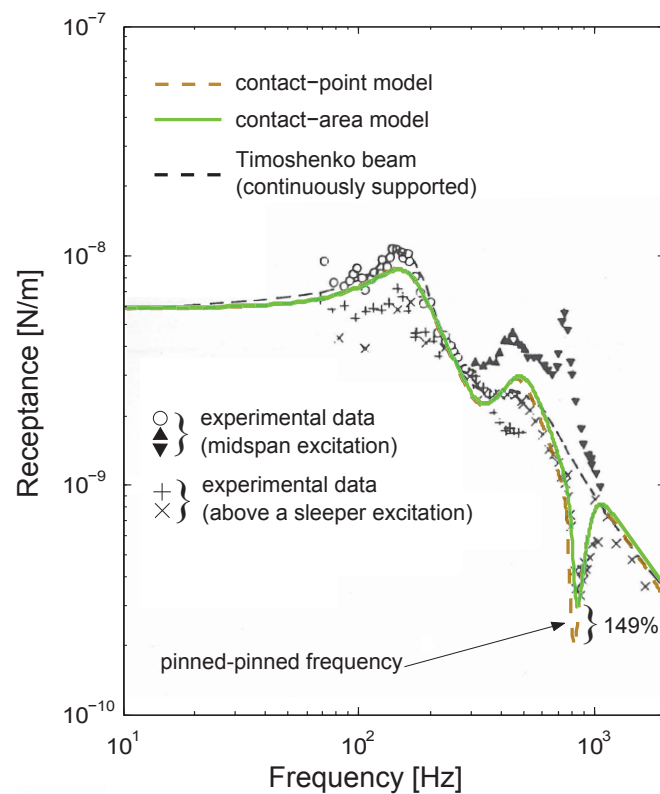


Figure 7.6 – Comparison between receptances of the railway in the case of: the connection-point model, the connection-area model and experimental data [42]; case of on-sleeper excitation.

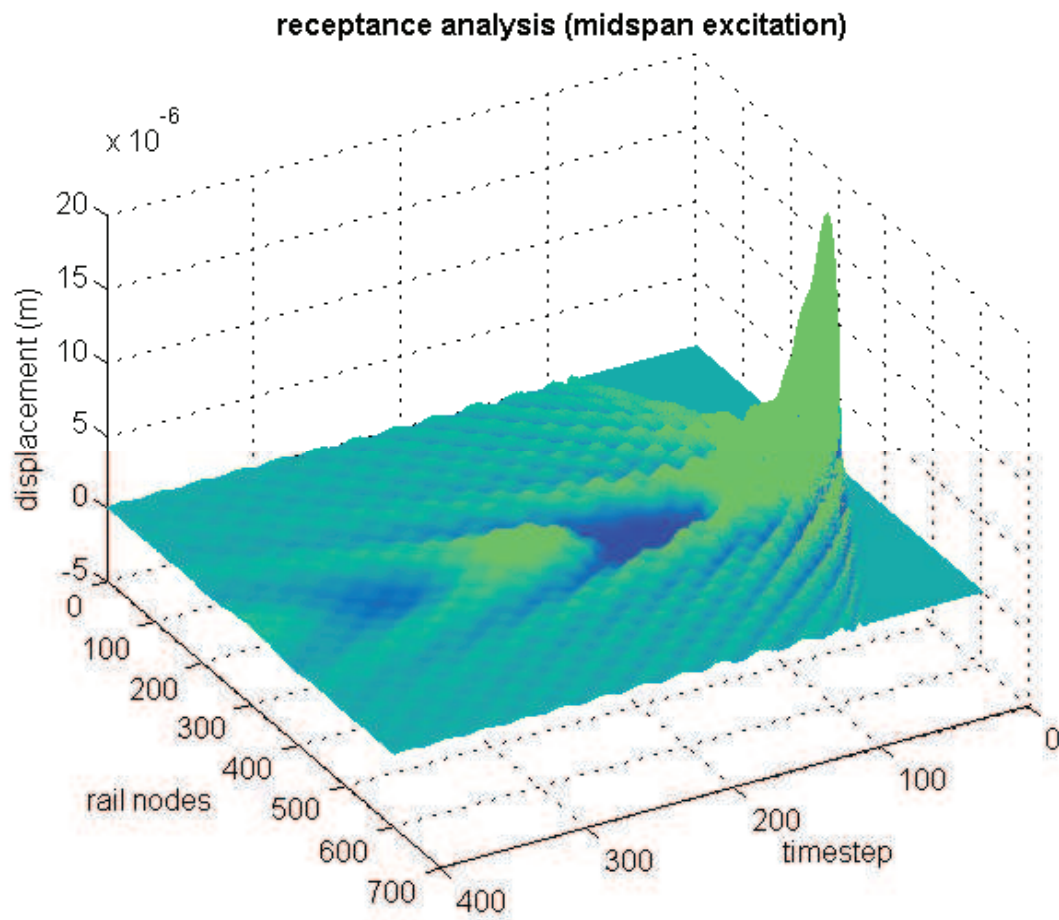


Figure 7.7 – Waves propagation in time and in space due to a midspan excitation.

8.1 THE SCENARIOS STUDIED

A comparison with experimental results and with other numerical models is done to validate the present model. An appropriate number of finite elements is chosen to have a good approximation and simultaneously not extend too much the computational time. The part of rail between two consecutive sleepers is discretized with nine beam elements; the part of rail vertically connected to sleepers by pads is discretized with six beam elements. The model is applied to many railway lines with different properties. In the Case 1 the rail is an old line with wood sleepers. A corrugation function has been assigned to the rail with the American railway standard procedure (see paragraph 5.3). The comparison with experimental results is shown here. In the Case 2 the case of out-of-round wheels is treated. Finally, in the Case 3 a newer line is studied. The corrugation function in this case has been evaluated with the ISO3095 [15] method.

8.2 CASE 1 - CORRUGATED RAIL (AMERICAN RAILWAY STANDARD [45]) - COMPARISON WITH EXPERIMENTAL RESULTS

First railway section, 64.35 m long, is relative to the Italian line Alcamo-Marsala (116 km). It's an old line with wood sleepers. In this railway, measurements have been carried out with a series of accelerometers by [25]. A running of a *ALn688* train with a single configuration, having a velocity of 90 km h^{-1} , has been considered (see figure 8.1).



Figure 8.1 – A picture of a ALN668 Locomotive at the Train Station

The model parameters are shown in table 8.1. A comparison between experimental data [25] and numerical results of the rail vertical acceleration is shown in figure 8.2. Similarly a comparison of sleeper vertical acceleration is shown in figure 8.3. Experimental data (figure 8.2(a)) show how the peaks of rail vertical acceleration are included between 50 m s^{-2} and 100 m s^{-2} . Moreover, they occur in correspondence of the four wheels-sets passes. The same behavior is predicted by numerical simulation (figure 8.2(b)). In numerical simulations G. Di Mino et Al. [25] found a similar behavior for the sleeper acceleration too. However experimental data (figure 8.3(a)) shows that peaks of sleeper vertical acceleration occur in correspondence of bogies passes but they are not distinguishable for each wheel-set. figure 8.3(b) shows how present model predicts well this kind of behavior. The defect grade of railway is unknown so it has to be assumed. To study the influence of uncertainties connected to line grade index, many simulations have been implemented. Numerical results and experimental data have been compared varying the line grade index. The worst value of index ($I_{lg} = 1$) allows numerical simulation to fit well experimental data. Moreover as this case is referred to an old line it is supposable that defects are relevant.

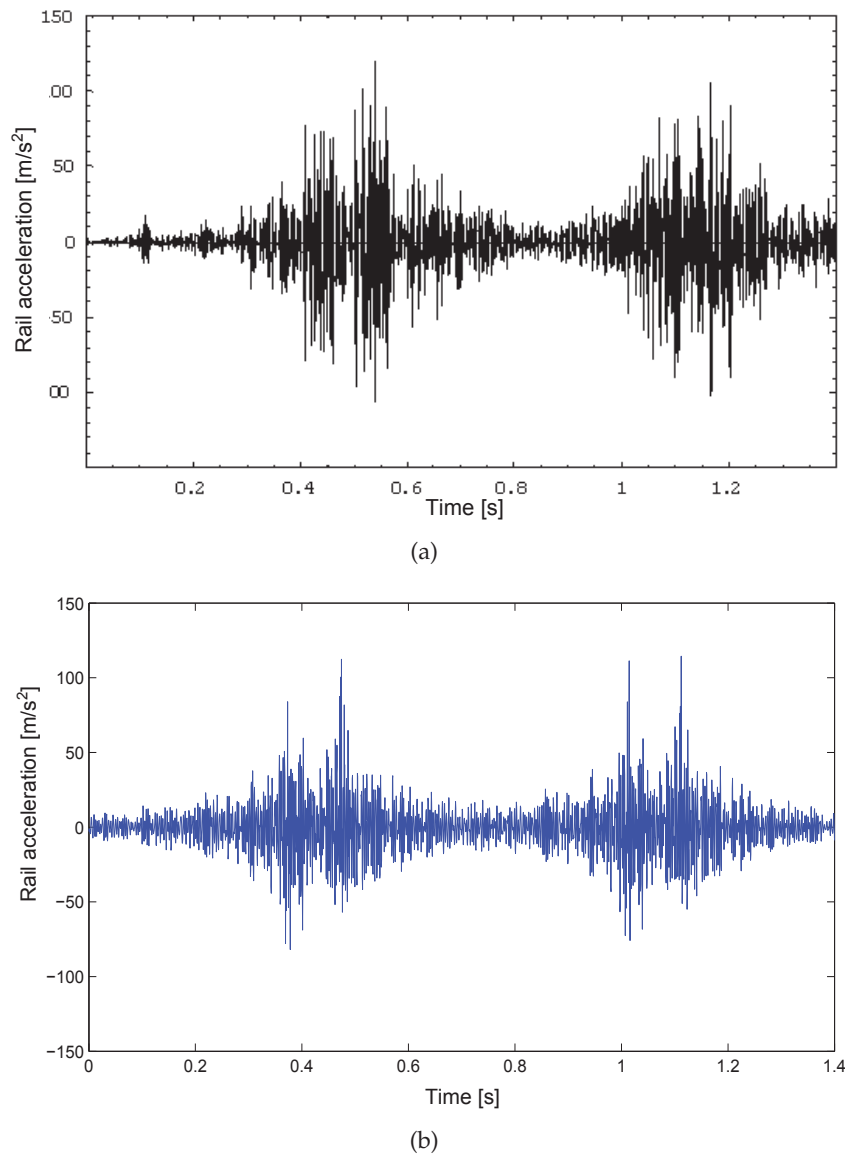
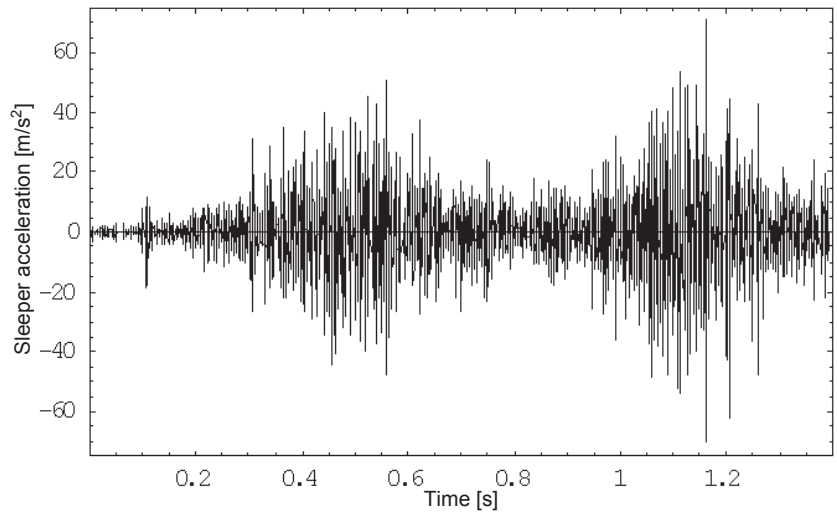


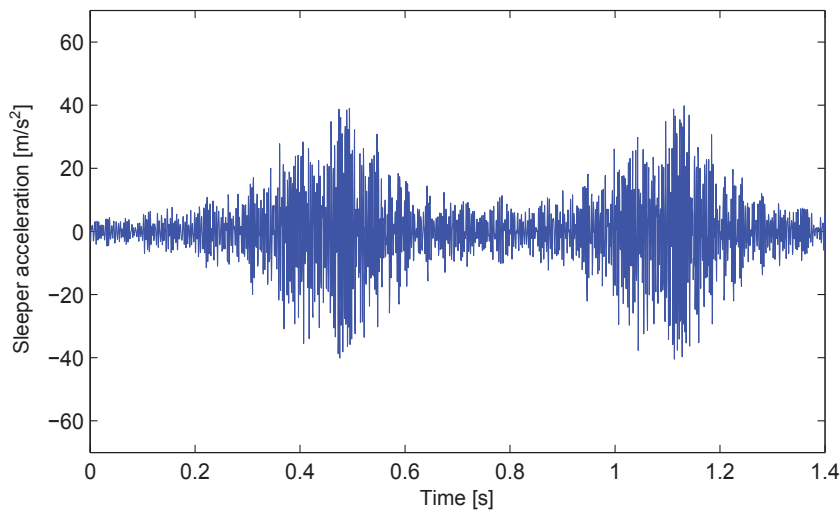
Figure 8.2 – Comparison between: (a) experimental data [25] and (b) numerical results of the rail vertical acceleration in the case 1.

8.3 CASE 2: OUT-OF-ROUND WHEELS - COMPARISON WITH EXPERIMENTAL RESULTS AND OTHER NUMERICAL MODELS

Second railway section is about the field testing reported by [22]. Their study has been carried out to analyze vertical interaction between wagon and track in case of out-of-round wheels. The wheels have been artificially grounded with a defect 40 mm long and 0.35 mm deep. Experimental data has been used by [80] to validate their model. The discretization adopted for the rail is the same as the previous case. Because of the few parameters reported by [22], model parameters for train and substructure have been extracted both from [80] and [22]. All values are reported in table 8.2. A comparison between experimental data [80] and numerical results for the second railway line is shown in figure 8.4. A simulation with no rail defects have been developed by other authors too [80, 22] (see figure 8.5(a) and 8.5(b)). Focusing on figure 8.4(a), the contact force returns to static value approximately 0.05 s after the perturbation caused



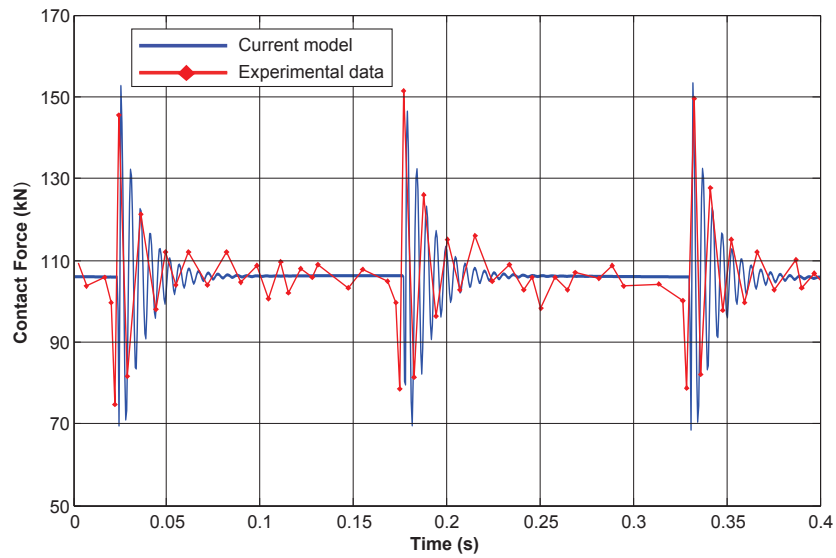
(a)



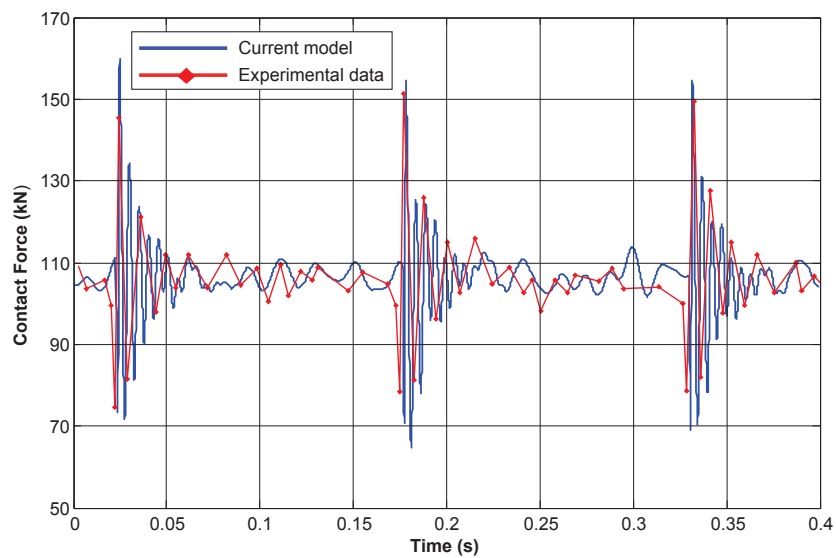
(b)

Figure 8.3 – Comparison between: (a) experimental data [25] and (b) numerical results of the sleeper vertical acceleration in the first case.

by wheel defect. Analyzing the experimental data in figure 8.4(a) it can be seen how the contact force maintains a periodical oscillation until next defect. This fact could be probably explained considering that the experimental data is affected by a minimum level of defects present on rail. A lower level of defect: $I_{lg} = 6$ is applied to the rail to best represent this phenomena. Looking at figure 8.4(b) the simulation with rail defects seems to fit better experimental data. The lower and the upper pulsation in table 8.2 are equivalent to ordinary values of long wavelength roughness (2000 mm) and a medium wavelength roughness (220 mm) when the train velocity is 70 km h^{-1} . The number of sinusoidal defects functions N_{d2} (see equation 5.8) seems to be not so relevant after the value of 100, anyway the X. Lei and N.A. Noda [45] suggested the value: $N_{d2} = 2500$.

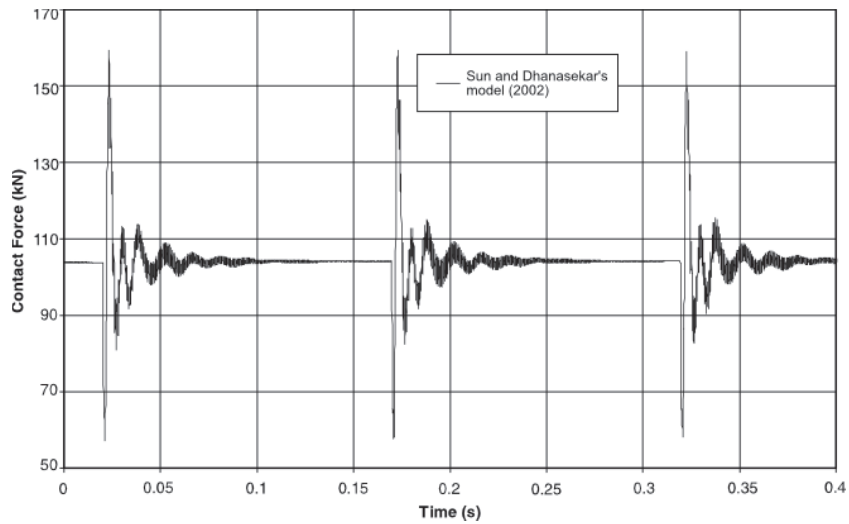


(a)

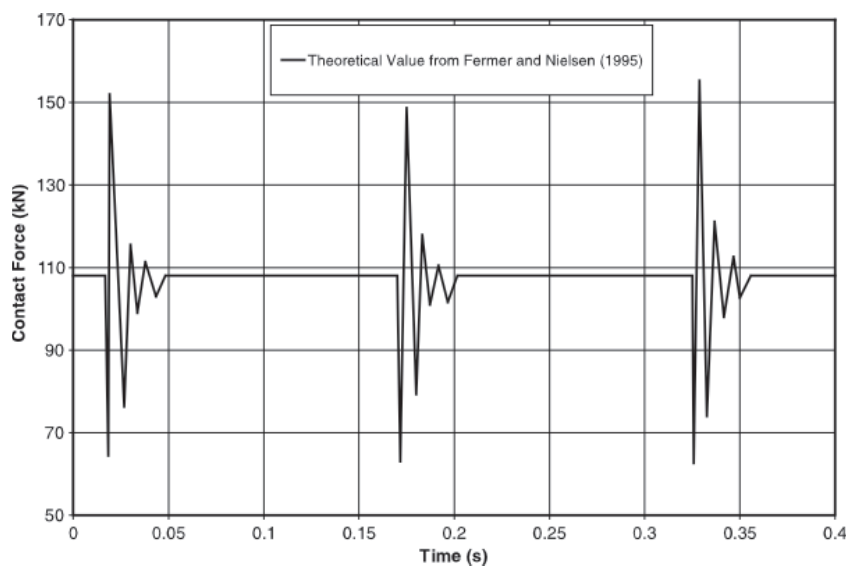


(b)

Figure 8.4 – Comparison between experimental data [80] and numerical results for the case 2: (a) not including rail defects; (b) including rail defects.



(a)



(b)

Figure 8.5 – Numerical results of: (a) Sun and Dhanasekar[80]; (b) Fermer and Nielsen[22].

Table 8.1 – Model parameters adopted for the simulation in first railway line.

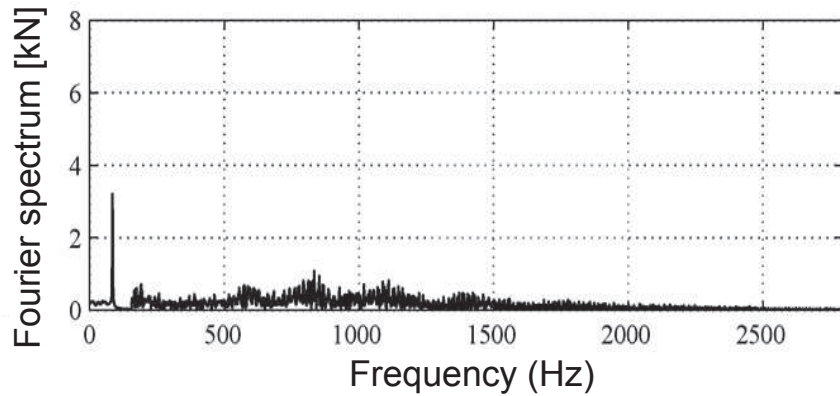
Case 1			
notation	parameter	value	unit
Model parameters of substructure ^a			
E	young modulus of rail	$2.07 \cdot 10^{11}$	N m^{-1}
I	inertial modulus of rail	$1884 \cdot 10^{-8}$	m^4
A	section area of rail	$63.62 \cdot 10^{-4}$	m^2
χ	Timoshenko shear coefficient	0.34	
m_r	railway mass (per unit length)	49.9	kg m^{-1}
M_s	sleeper mass	33	kg
M_b	ballast mass	700	kg
k_p	pad stiffness	$26.5 \cdot 10^7$	N m^{-1}
c_p	pad damping	$40 \cdot 10^3$	N s m^{-1}
k_b	ballast stiffness	$24 \cdot 10^7$	N m^{-1}
c_b	ballast damping	$58.8 \cdot 10^3$	N s m^{-1}
k_w	horizontal stiffness	$7.84 \cdot 10^7$	N m^{-1}
c_w	horizontal damping	$80 \cdot 10^3$	N s m^{-1}
k_f	subgrade stiffness	$7.68 \cdot 10^7$	N m^{-1}
c_f	subgrade damping	$64.6 \cdot 10^3$	N s m^{-1}
l_s	sleeper base	65	cm
Model parameters of train <i>Aln668</i> ^a			
$2M_c$	car body mass	28800	kg
M_b	bogie mass	3600	kg
$2M_w$	wheelset mass	500	kg
l_c	total length	23540	mm
$2l_b$	wheelset base	2.45	m
$2l_w$	bogie base	15.95	m
k_1	primary suspension stiffness	500	kN m^{-1}
k_2	secondary suspension stiffness	8800	kN m^{-1}
c_1	primary suspension damping	0.5	kN s m^{-1}
c_2	secondary suspension damping	41.5	kN s m^{-1}
Other simulation parameters			
dt	time step	$6 \cdot 10^{-5}$	s
K_h	Hertz contact coefficient ^b	$0.87 \cdot 10^{11}$	$\text{N m}^{-3/2}$
C_h	contact damping coefficient	$3 \cdot 10^5$	N s m^{-1}
L_s	simulation line length ^a	64.45	m
n	number of pad elements	7	
d	number of beam elements between sleepers	9	
N	number of defects functions	200	
ω_u	upper pulsation	1560	rad s^{-1}
ω_l	lower pulsation	12	rad s^{-1}
I_{lg}	line grade index	1	
V	train velocity	90	km h^{-1}

^a parameters extracted from [25].

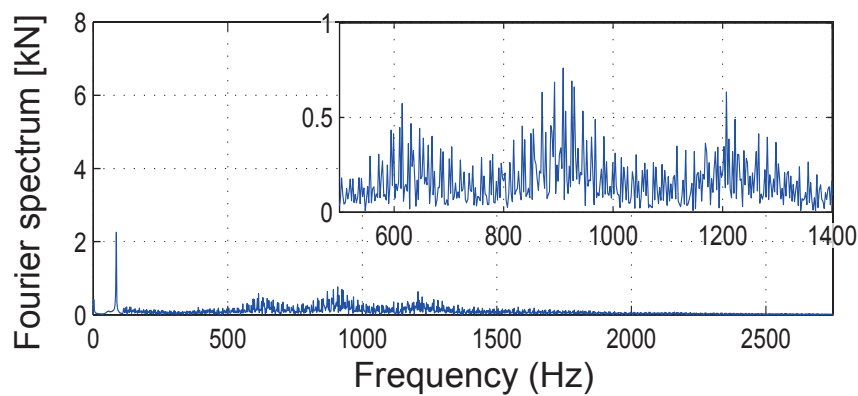
8.4 CASE 3: CORRUGATED RAIL (ISO3095 [15]) - COMPARISON WITH OTHER NUMERICAL MODELS

In this case a rail with corrugation based on ISO3095 [15] is considered. The modal frequency analysis of the contact-force has been compared with results obtained by A. Johansson and J.C.O. Nielsen [36] model. The comparison between models is shown

in figure 8.6. The biggest amplitude of the normal contact-force Fourier spectrum corresponds to the train sleeper passing frequency: 85 Hz. Focusing on figure 8.6(b), amplitudes increase in magnitude around 600 Hz, 900 Hz and 1200 Hz. These frequencies correspond to the bending modes of a rail, with pinned-pinned boundary conditions, considering the same length of the boogie wheelbase [32, 78]. Experimental results confirm this behavior [36].



(a) Fourier spectrum of the normal contact force by Johansson & Nielsen [36]



(b) Fourier spectrum of the normal contact-force calculated with our model

Figure 8.6 – Comparison between A. Johansson and J.C.O. Nielsen [36] model and the proposed one in case of ISO3095 [15] based corrugation.

Table 8.2 – Model parameters adopted for the simulation in second railway line.

Case 2			
notation	parameter	value	unit
Model parameters of substructure			
E	young modulus of rail ^a	$2.07 \cdot 10^{11}$	N m^{-1}
I	inertial modulus of rail ^b	$2940 \cdot 10^{-8}$	m^4
A	section area of rail ^b	$77.70 \cdot 10^{-4}$	m^2
χ	Timoshenko shear coefficient ^b	0.34	
m_r	railway mass ^a (per unit length)	60	kg m^{-1}
M_s	sleeper mass ^b	270	kg
M_b	ballast mass ^b	480	kg
k_p	pad stiffness ^a	$57.65 \cdot 10^6$	N m^{-1}
c_p	pad damping ^a	$33.65 \cdot 10^3$	N s m^{-1}
k_b	ballast stiffness ^c	$29.06 \cdot 10^6$	N m^{-1}
c_b	ballast damping	$8.30 \cdot 10^3$	N s m^{-1}
k_w	horizontal stiffness ^c	$7.84 \cdot 10^6$	N m^{-1}
c_w	horizontal damping ^c	$2.49 \cdot 10^3$	N s m^{-1}
k_f	subgrade stiffness ^c	$76.80 \cdot 10^6$	N m^{-1}
c_f	subgrade damping	$64.6 \cdot 10^3$	N s m^{-1}
l_{sl}	sleeper base ^a	68.5	cm
L_s	effective length of rail support area ^b	16.4	cm
Model parameters of the train			
$2M_c$	car body mass ^d	72000	kg
M_b	bogie mass ^b	3600	kg
$2M_w$	wheelset mass ^b	1900	kg
$2l_b$	wheelset base ^b	1.675	m
$2l_w$	bogie base ^b	10.36	m
k_1	primary suspension stiffness ^b	6500	kN m^{-1}
k_2	secondary suspension stiffness ^b	2555	kN m^{-1}
c_1	primary suspension damping ^b	10	kN s m^{-1}
c_2	secondary suspension damping ^b	30	kN s m^{-1}
r_w	wheel radius ^a	0.475	m
Other simulation parameters			
dt	time step	$5.14 \cdot 10^{-5}$	s
K_h	Hertz contact coefficient ^b	$0.87 \cdot 10^{11}$	$\text{N m}^{-3/2}$
n	number of pad elements	7	
d	number of beam elements between sleepers	9	
N	number of defects functions	2500	
ω_u	upper pulsation	555	rad s^{-1}
ω_l	lower pulsation	61	rad s^{-1}
I_{lg}	line grade index	6	
V	train velocity	70	km h^{-1}

^a Values extracted from [22]^b Values extracted form [80]^c Calculated Values

THE SENSITIVITY ANALYSIS

9

9.1 INTRODUCTION

A sensitivity analysis has been done to study the influence of each model variable to output parameters. Indeed all variables are susceptible to uncertainties. Moreover the variables have a range of variation depending on the type of train or substructure. During the phase of model building it is necessary to study the influence of each variable to focus the calibration on most important variable and, in some case, eliminate the unnecessary ones. A OFAT method (one-factor-at-a-time) is adopted to evaluate the sensitivity of parameters to each variable.

9.2 THE INPUT VARIABLES

In order to analyze the sensitivity of the model, the variational range of each values has to be set. In tables 4.2 and 4.1 the values of k_b , c_b , k_p , c_p adopted by other authors is shown. Considering these values, the variational range for the substructure stiffness and damping values has been fixed. The sleeper masses are known; they depend principally on the type and material used (wood, reinforced concrete, bi-block in reinforced concrete and steel). Also the rail mass is known; it depends on the type of rail adopted. The rail linear masses are shown in table 3.4. The Manchester Benchmark [34] and the values adopted by other authors have been considered to evaluate the range of variation of the train variables. In figure 9.1 the variational range of each variable is shown.

		x_0	x_{\max}	x_{\min}	dim	$V(x_i)$
1	kp	1,70E+08	2,55E+08	8,50E+07	N/m	4,82E+15
2	cp	3,00E+04	4,50E+04	1,50E+04	Ns/m	1,50E+08
3	kb	2,00E+08	3,00E+08	1,00E+08	N/m	6,67E+15
4	cb	8,50E+04	1,28E+05	4,25E+04	Ns/m	1,20E+09
5	kf	1,50E+09	2,25E+09	7,50E+08	N/m	3,75E+17
6	cf	5,00E+04	7,50E+04	2,50E+04	Ns/m	4,17E+08
7	ms	125	200	30	kg	4,84E+03
8	mb	500	900	300	kg	6,22E+04
9	Mc	16000	24000	8000	kg	4,27E+07
10	Mb	1307,5	1961,25	653,75	kg	2,85E+05
11	Mw	906,5	1359,75	453,25	kg	1,37E+05
12	k1	2,22E+06	3,33E+06	1,11E+06	N/m	8,21E+11
13	k2	6,43E+06	9,65E+06	3,22E+06	N/m	6,89E+12
14	c1	2,00E+03	1,00E+03	3,00E+03	Ns/m	6,67E+05
15	c2	2,00E+04	3,00E+04	1,00E+04	Ns/m	6,67E+07
16	kh	8,70E+10	1,31E+11	4,35E+10	N/m ^{-1,5}	1,26E+21

Figure 9.1 – Variational range of each input variable.

9.3 THE OUTPUT PARAMETERS

The output parameters selected for the analysis are the dynamic amplification factor of the wheel-rail contact force $\delta_{dyn} = R_{w/r}/R_{static}$ (R_{static} is the vehicle weight divided by the number of wheels) and the sleeper elastic vertical deflection z_{sl} . The dynamic amplification factor is time dependent. The contact force $R_{w/r}$ varies around the static value during the simulation and at certain time steps it assumes very high values. Anyway, these values are singular points and do not represent the complete behavior of contact-force during the whole time of simulation T . The following procedure has been conducted to choose a representative output parameter. The time interval $[0, T]$ has been divided in p intervals of size τ . For each g -range the maximum value of the dynamic amplification factor $\delta_{dyn,g}$ has been evaluated for the third wheel from the left. In fact, the third wheel is the one less affected by boundary effects. Therefore the average between maximum values in all the time ranges has been calculated for each simulation. The procedure is summarized in equation (9.1).

$$\left\{ \begin{array}{l} \overline{\delta_{dyn}} = \sum_{g=1}^p \frac{\delta_{dyn,g}}{p} \\ p = \frac{T}{\tau} \\ \delta_{dyn,g} = \max \left[\frac{R_{w/r,3}(t)}{R_{static}} \right] \quad t \in [(g-1)\tau, (g)\tau]; \quad g = 1, 2, \dots, p. \end{array} \right. \quad (9.1)$$

The interval τ has been calculated as the time necessary to cover the passing of three consecutive sleepers. The sleeper distance used is 0.65 meters, so τ has been calculated as $2.3 \text{ m}/V$, being $(3 \times 0.65 \text{ m}) < 2.3 \text{ m}$. An example for $p = 3$ is shown in figure 9.2.

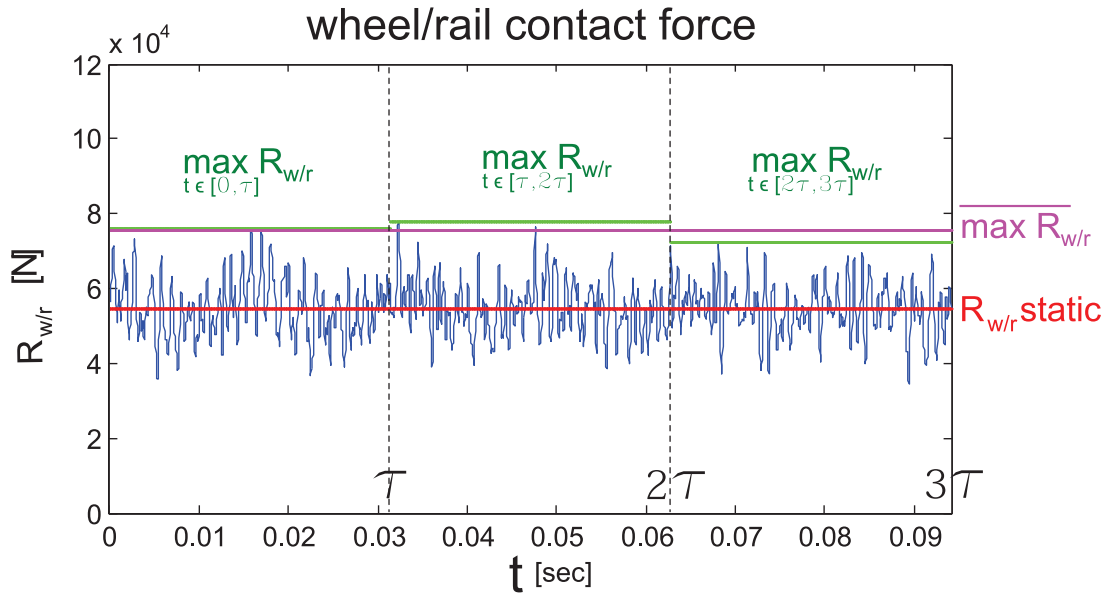


Figure 9.2 – An example for the determination of the average dynamic amplification factor.

Many studies [14, 56, 68, 27, 8, 9] show how the ballast vertical settlement is proportional to the elastic deflection caused by each wheel pass and the number of applied wheel loads. Being ballast maintenance one of the most important cost for the rail infrastructure operators, a sensitivity analysis of the sleeper deflection is done. The sleeper chosen to check the maximum deflection value is the nearest one to the mid-point between the end of the railway length and the fourth wheel from the left. Among others, this sleeper is the one less affected by boundary effects.

9.4 THE OFAT METHOD

The sensitivity index for every variable can be calculated with the standard regression coefficient [37] as:

$$SRC_i = \frac{\beta_i^2 V(X_i)}{V(Y)} \in [0, 1] \quad (9.2)$$

where the operator V means *variance of*; The coefficient β_i , in the case of a linear model, can be calculated as the ratio between the variation of the output parameter ΔY and the increment of the variable ΔX_i . Two simulations have been done for each input variable. One considering the value x_{min} and one considering X_{max} . Then the values β have been determined as:

$$\begin{aligned} \beta &= \frac{\beta_1 + \beta_2}{2} \\ \beta_1 &= \frac{y(x_{max}) - y(x_0)}{x_{max} - x_0} \\ \beta_2 &= \frac{y(x_0) - y(x_{min})}{x_0 - x_{min}}. \end{aligned} \quad (9.3)$$

The SRC of each variable for the dynamic amplification factor and the sleeper deflection are reported in figures 9.3 and 9.4. In the first figure 9.3 the variables are sorted by model parts: the substructure and the train; in the second figure 9.4 the variables are sorted by type: mass, damping and stiffness.

sorting by parts		$V(x_i)$	Z_{sl}			δ_{dyn}		
			$E(b_{zsl})$	$b_i^2 V(x_i)$	SRC_{zsl}	$E(b_{\delta_{dyn}})$	$b_i^2 V(x_i)$	$SRC_{\delta_{dyn}}$
substructure	kp	4,8E+15	1,8E-13	1,5E-10	2%	-1,1E-10	5,9E-05	1%
	cp	1,5E+08	-3,1E-11	1,5E-13	0%	-1,4E-06	2,8E-04	7%
	kb	6,7E+15	-7,6E-13	3,9E-09	61%	4,3E-11	1,2E-05	0%
	cb	1,2E+09	-1,0E-11	1,2E-13	0%	2,0E-07	4,9E-05	1%
	kf	3,8E+17	-3,5E-18	4,5E-18	0%	2,4E-12	2,2E-06	0%
	cf	4,2E+08	-1,3E-11	7,0E-14	0%	-7,3E-08	2,2E-06	0%
	ms	4,8E+03	3,1E-08	4,6E-12	0%	-1,2E-04	6,8E-05	2%
	mb	6,2E+04	-4,7E-10	1,4E-14	0%	2,4E-05	3,5E-05	1%
train	Mc	4,3E+07	7,2E-09	2,2E-09	34%	-9,0E-06	3,5E-03	82%
	Mb	2,8E+05	1,4E-08	5,6E-11	1%	-1,5E-05	6,5E-05	2%
	Mw	1,4E+05	2,8E-08	1,0E-10	2%	-1,9E-05	5,1E-05	1%
	k1	8,2E+11	-9,4E-14	7,3E-15	0%	-5,6E-09	2,6E-05	1%
	k2	6,9E+12	-4,1E-14	1,1E-14	0%	2,4E-09	3,9E-05	1%
	c1	6,7E+05	2,6E-10	4,6E-14	0%	-1,9E-06	2,4E-06	0%
	c2	6,7E+07	4,4E-11	1,3E-13	0%	-8,9E-07	5,3E-05	1%
	kh	1,3E+21	2,2E-18	6,0E-15	0%	-1,3E-14	2,0E-07	0%
V(Y)		6,39E-09	100%	V(Y)	4,23E-03	100%		

Figure 9.3 – Standard regression coefficients of input variables sorted by parts.

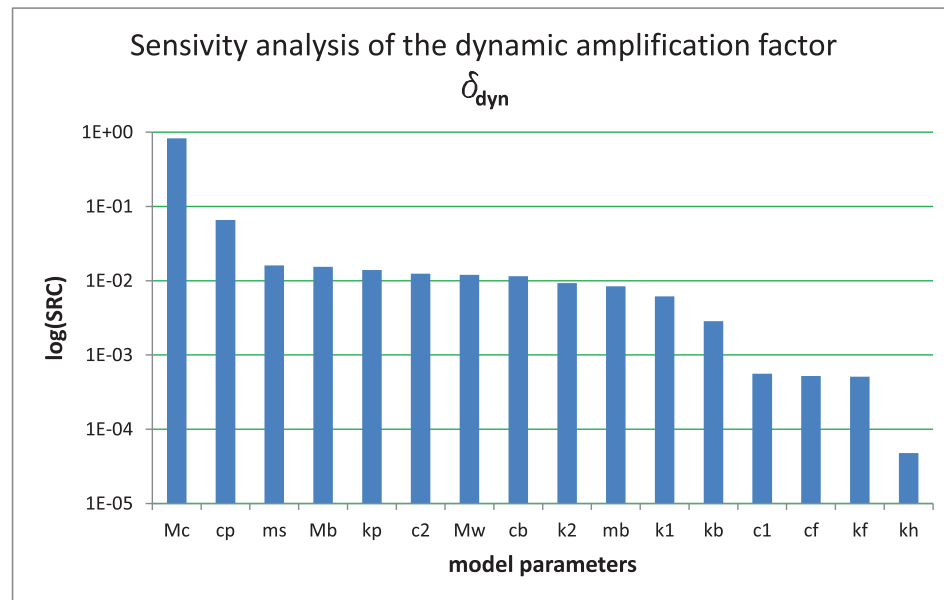
sorting by type		$V(x_i)$	Z_{sl}			δ_{dyn}		
			$E(b_{zsl})$	$b_i^2 V(x_i)$	SRC_{zsl}	$E(b_{\delta_{dyn}})$	$b_i^2 V(x_i)$	$SRC_{\delta_{dyn}}$
stiffness	kp	4,8E+15	1,8E-13	1,5E-10	2%	-1,1E-10	5,9E-05	1%
	kb	6,7E+15	-7,6E-13	3,9E-09	61%	4,3E-11	1,2E-05	0%
	kf	3,8E+17	-3,5E-18	4,5E-18	0%	2,4E-12	2,2E-06	0%
	k1	8,2E+11	-9,4E-14	7,3E-15	0%	-5,6E-09	2,6E-05	1%
	k2	6,9E+12	-4,1E-14	1,1E-14	0%	2,4E-09	3,9E-05	1%
	kh	1,3E+21	2,2E-18	6,0E-15	0%	-1,3E-14	2,0E-07	0%
damping	cp	1,5E+08	-3,1E-11	1,5E-13	0%	-1,4E-06	2,8E-04	7%
	cb	1,2E+09	-1,0E-11	1,2E-13	0%	2,01E-07	4,9E-05	1%
	cf	4,2E+08	-1,3E-11	7,0E-14	0%	-7,3E-08	2,2E-06	0%
	c1	6,7E+05	2,6E-10	4,6E-14	0%	-1,9E-06	2,4E-06	0%
	c2	6,7E+07	4,4E-11	1,3E-13	0%	-8,9E-07	5,3E-05	1%
mass	Mc	4,3E+07	7,2E-09	2,2E-09	34%	-9,0E-06	3,5E-03	82%
	Mb	2,8E+05	1,4E-08	5,6E-11	1%	-1,5E-05	6,5E-05	2%
	Mw	1,4E+05	2,8E-08	1,0E-10	2%	-1,9E-05	5,1E-05	1%
	ms	4,8E+03	3,1E-08	4,6E-12	0%	-1,2E-04	6,8E-05	2%
	mb	6,2E+04	-4,7E-10	1,4E-14	0%	2,4E-05	3,5E-05	1%
V(Y)		6,39E-09	100%	V(Y)	4,23E-03	100%		

Figure 9.4 – Standard regression coefficients of input variables sorted by type.

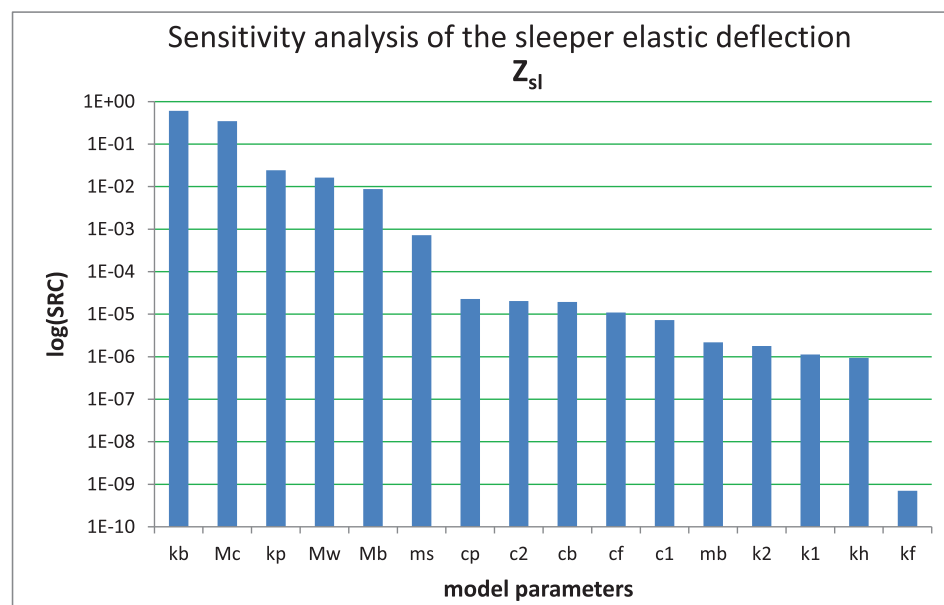
9.5 THE RESULTS

In figure 9.5, input parameters are plotted in a log scale and ordered according to their influence. SRC values are also reported in tables 9.6 and 9.7. The importance of train mass is observed in both analysis. The ballast equivalent stiffness has a lot of influence

on the sleeper deflection but not on the dynamic amplification factor. Focusing on figure 9.5(a) a significant outcome is about the damping properties of ballast. Indeed they results not very important if compared to damping of pads. This property is inverted for the ballast deflection (figure 9.5(b)) where the ballast equivalent damping is more significant. Moreover in both of the analysis the wheel masses show a large influence.



(a)



(b)

Figure 9.5 – Sensitivity analysis of: (a) the dynamic amplification factor; (b) the sleeper elastic deflection.

δ_{dyn}		
sorting by importance		$\text{SRC}_{\delta_{\text{dyn}}}$
1	Mc	8,25E-01
2	cp	6,57E-02
3	ms	1,61E-02
4	Mb	1,54E-02
5	kp	1,39E-02
6	c2	1,24E-02
7	Mw	1,20E-02
8	cb	1,15E-02
9	k2	9,32E-03
10	mb	8,38E-03
11	k1	6,16E-03
12	kb	2,86E-03
13	c1	5,60E-04
14	cf	5,20E-04
15	kf	5,09E-04
16	kh	4,77E-05

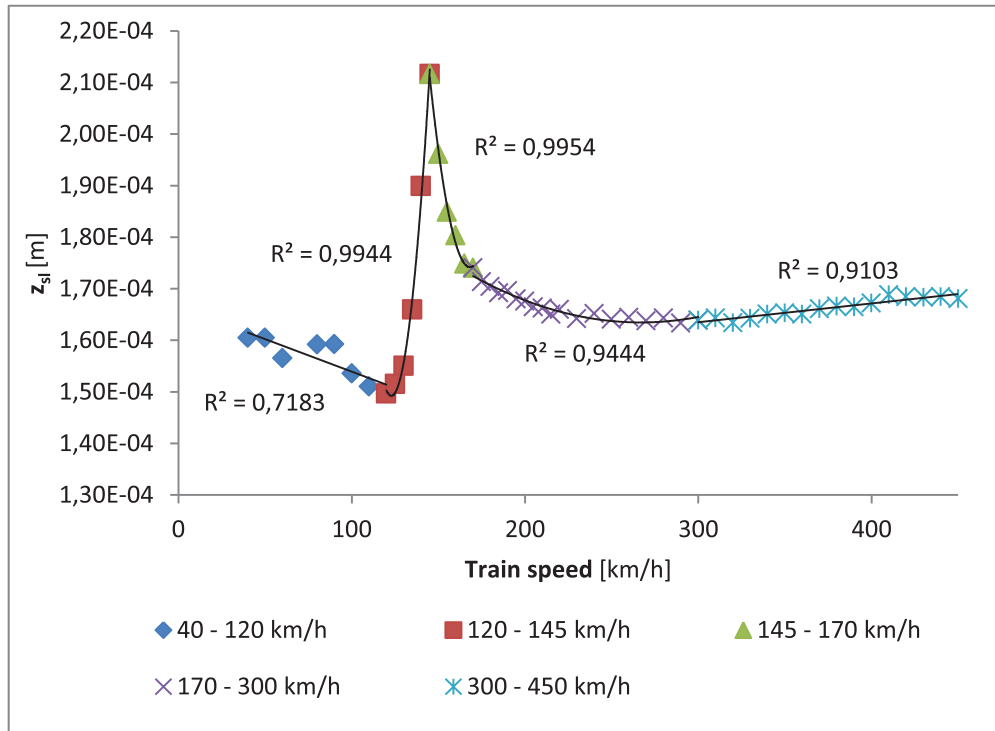
Figure 9.6 – Standard regression coefficients of input variables for the dynamic amplification factor ordered by importance.

Z_{sl}		
sorting by importance		SRC_{zsl}
1	kb	6,05E-01
2	Mc	3,45E-01
3	kp	2,42E-02
4	Mw	1,63E-02
5	Mb	8,72E-03
6	ms	7,20E-04
7	cp	2,28E-05
8	c2	2,05E-05
9	cb	1,94E-05
10	cf	1,10E-05
11	c1	7,26E-06
12	mb	2,17E-06
13	k2	1,80E-06
14	k1	1,14E-06
15	kh	9,32E-07
16	kf	7,07E-10

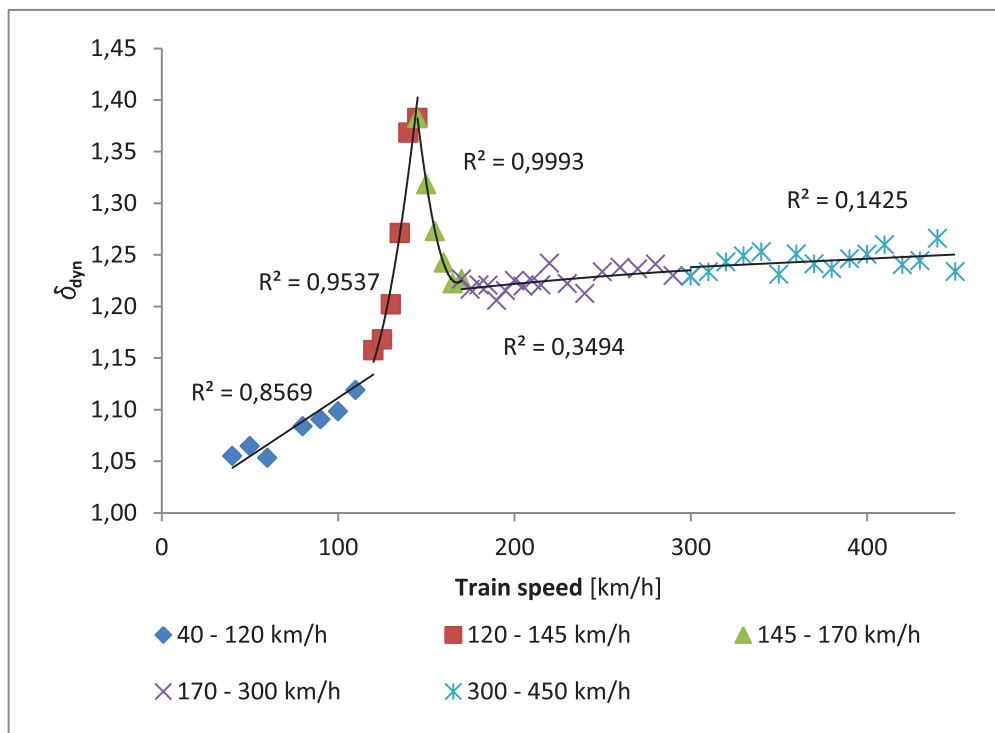
Figure 9.7 – Standard regression coefficients of input variables for the sleeper deflection ordered by importance.

9.6 THE INFLUENCE OF TRAIN SPEED ON SLEEPER ELASTIC DEFLECTION AND DYNAMIC AMPLIFICATION FACTOR

The influence of train speed on sleeper elastic deflection and on dynamic amplification factor can be studied with a sensitivity analysis too. In this case all input variables except velocity are fixed. The values adopted to do the analysis are the same as those of figure 9.1. The variational range of train speed is 40 – 450 km h⁻¹. The sleeper elastic deflection and the dynamic amplification factor in function of train velocity are shown in figure 9.8.



(a)



(b)

Figure 9.8 – The influence of train speed on: (a) the sleeper elastic deflection; (b) the dynamic amplification factor.

Focusing on figure 9.8(a), the behavior of curve can be separated in five ranges. In the first range $40 - 120 \text{ km h}^{-1}$ the tendency of the curve is an inverse proportion. This fact could be explained with a comparison to road infrastructure. It is well known how

the dynamic modulus of many material is directly proportional to the frequency of excitation. This is the case for the road infrastructure. Indeed the slower vehicles, weight being equal, produce much rutting than faster vehicles. In the same way it can be affirmed that, for slow speeds, the equivalent complex modulus of substructure is directly proportional to train velocity. Then the deformation decrease with speed increasing. In the second range $120 - 145 \text{ km h}^{-1}$ the behavior changes totally. In this interval the elastic deflection increases quickly up to a critical speed (145 km h^{-1} in this case). The reason of this behavior will be discussed in paragraph 12.2.1. Once the critical speed is passed the elastic deflection decreases quickly in the range $145 - 170 \text{ km h}^{-1}$. This interval where the deflection increases and decreases quickly is centered on critical speed with a range of $V_c \pm 25 \text{ km h}^{-1}$. Once this interval is passed the deflection continues to decrease but with a smaller slope. This range is $170 - 300 \text{ km h}^{-1}$. Finally the deflection restarts to increase with a small inclination in the range $300 - 450 \text{ km h}^{-1}$. Focusing on figure 9.8(b), the behavior of dynamic amplification factor has been divided in five range too, only to compare intervals with elastic deflection chart. In this case the dynamic amplification factor is proportional to speed in first, fourth and fifth interval. In the range $V_c \pm 25 \text{ km h}^{-1}$, it assumes the same behavior than sleeper deflection. Some guesswork could be done comparing curves. Overlooking what happens near to critical speed, the elastic deflection must obey to two physical phenomenons contemporaneously. The first one is about the equivalent complex modulus of substructure. It could be deduced, force being equal, that the elastic deflection should always decrease with speed increasing. The second phenomenon can be seen focusing on dynamic amplification factor behavior. Indeed, increasing the speed, the dynamic load increases too. It follows that the elastic deflection should increase with the dynamic load increasing. Finally these two phenomenons contrasts each to other. In the case studied, the first phenomenon wins on second one up to 300 km h^{-1} speed. Once this speed is passed the dynamic loads still increases inverting the process.

A NEW FORMULATION TO EVALUATE THE RAILWAY TOLLS

10.1 INTRODUCTION

The target of this paragraph is to propose a new formulation for the calculation of the railway toll. In accordance to the new deregulation of European rail transport, all member states of EU have to separate the railway administration in two separate agency: the Infrastructure Manager and the Train Operator. Indeed this separation will allow to liberalize the trade of this kind of service. In this scenario Train Operators pay a toll to the Infrastructure Manager to allow the trains circulation. The toll depends on many parameters such as the train speed, the weight, the train type, the type of railway track, the energy consumption, the time and the kilometers run. A part of toll is proportional to the Infrastructure wear. It is well known that the biggest wear cost is related to the ballast maintenance. It's a difficult problem to find a simple relationship between costs and train parameters. For this reason in this paragraph a method to evaluate the part of toll related to the ballast maintenance is proposed. Moreover we perceived that the Italian method to evaluate the wear tolls is improper.

10.2 THE ITALIAN SCENARIO

The Italian Infrastructure Manager in Italy is *RFI (Rete Ferroviaria Italiana)*. It is responsible for the track, the stations and the installations. *RFI* ensures to railway undertakings the access to the railway network, performs the maintenance and the safe circulation on the whole network, manages the investments for the upgrading and improvement of railway lines and installations and it develops the technology of systems and materials [1]. All Train Operators, such as *Trenitalia* or *NTV*, have to follow the EU directive on the deregulation of European rail transport. As a consequence they have to pay a toll to *RFI* to allow the trains circulation. The relations between Infrastructure Manager and Train Operators are regulated by the *PIR (Prospetto Informativo di Rete)*. This document, among other things, sanctions the rules for the toll payment. Moreover an Italian Ministerial Decree reports the method to evaluate the toll. The Decree is *D.M. 21/04/2000: determinazione dei criteri di determinazione del canone di utilizzo dell'infrastruttura ferroviaria* (the methodology to evaluate the Railway Infrastructure tolls). According to the Decree the total Toll can be divided in two parts:

$$\$ = \$_1(\text{line}) + \$_2(\text{space, time}). \quad (10.1)$$

The part $\$_1$ is a fixed quota depending on the type of line. This part considers the quality of the Infrastructure in the way requested by train Operator. The second part depends

on the use of the Infrastructure. Therefore this part is proportional to time and space. It can be calculated as

$$\$2 = \$_{ref} \sum_{j=1}^n \sum_{w=1}^s km_{jw} (\alpha_1 W_{capacity} + \alpha_2 W_{density} + \alpha_3 W_{wear}), \quad (10.2)$$

where:

- $\$_{ref}$ is a reference fixed cost $\$_{ref} = 1\text{€}$;
- j is the type of line (a list is shown in the decree);
- n is the total number of line types;
- w is the type of time slot (a list is shown in the decree);
- s is the total number of time slots;
- $\alpha_1, \alpha_2,$ and α_3 are three fixed coefficients; the sum as to be equal to 1; the decree attachment specify that each coefficient is $\alpha_i = 0.3$;
- $W_{capacity}$ is the cost weight related to the reduction of Infrastructure capacity;
- $W_{density}$ is the cost weight related to the vehicle traffic density;
- W_{wear} is the cost weight related to wear.

Finally the wear is 1/3 of total cost $\$2$. This weight can be evaluated as discrete function of a variable z . The values of W_{wear} in function of z are reported in table 10.1.

Coefficients for W_{wear}			
Interval	Interval limits		W_{wear}
i	z_{i-1}	z_i	$W_{wear,i}$
1	0	0.8	0.7
2	0.8	1.2	1.0
3	1.2	2.0	1.8
4	2.0	> 2	3.5

Table 10.1 – Values of the discrete function $W_{wear}(z)$

The variable z is function of train speed, train weight and number of pantographs used. It is:

$$z = \frac{\beta_1 (V^2 P) + \beta_2 (V N)}{\beta_1 (V_{ref}^2 P_{ref}) + \beta_2 (V_{ref} N_{pant,ref})}, \quad (10.3)$$

where:

- $\beta_1 = 0.85$;
- $\beta_2 = 0.15$;
- V is the train speed;

- P is the train weight;
- N is the number of pantographs used;
- V_{ref} is the train reference speed $V_{ref} = 80 \text{ km h}^{-1}$;
- P_{ref} is the train reference weight $P_{ref} = 500 \text{ tonn}$.

The aim of this paragraph is to evaluate the relationship between wear costs and train variables. To compare it to the new formulation proposed, the part of cost related to substructure has to be isolated. The function z can be separated in two parts, one for the substructure wear and one for the pantograph wear:

$$z = z_{sub} + z_{pant}$$

$$z = \frac{\beta_1 (V^2 P)}{\beta_1 (V_{ref}^2 P_{ref}) + \beta_2 (V_{ref} N_{pant,ref})} + \frac{\beta_2 (V N_{pant})}{\beta_1 (V_{ref}^2 P_{ref}) + \beta_2 (V_{ref} N_{pant,ref})}. \quad (10.4)$$

Moreover, looking at coefficients $\beta_1 = 85\%$ and $\beta_2 = 15\%$, it can be affirmed that the substructure cost is more relevant. Than, grouping all constants, the function $z_{sub}(V, P)$ can be defined as:

$$z_{sub} = c_{sub} P V^2$$

$$c_{sub} = \frac{\beta_1}{\beta_1 (V_{ref}^2 P_{ref}) + \beta_2 (V_{ref} N_{pant,ref})}. \quad (10.5)$$

Knowing the function $z_{sub}(V)$ and $W_{wear}(z)$ it is possible to determine the function W_V . To define this function the approximation $z_{pant} = 0$ has been assumed. This assumption is reasonable if considering the coefficients β_1 and β_2 . Moreover the aim is not to focus on W_{wear} values but only on the relationship with train speed. Next considerations are true not considering costs connected to the wear of pantographs.

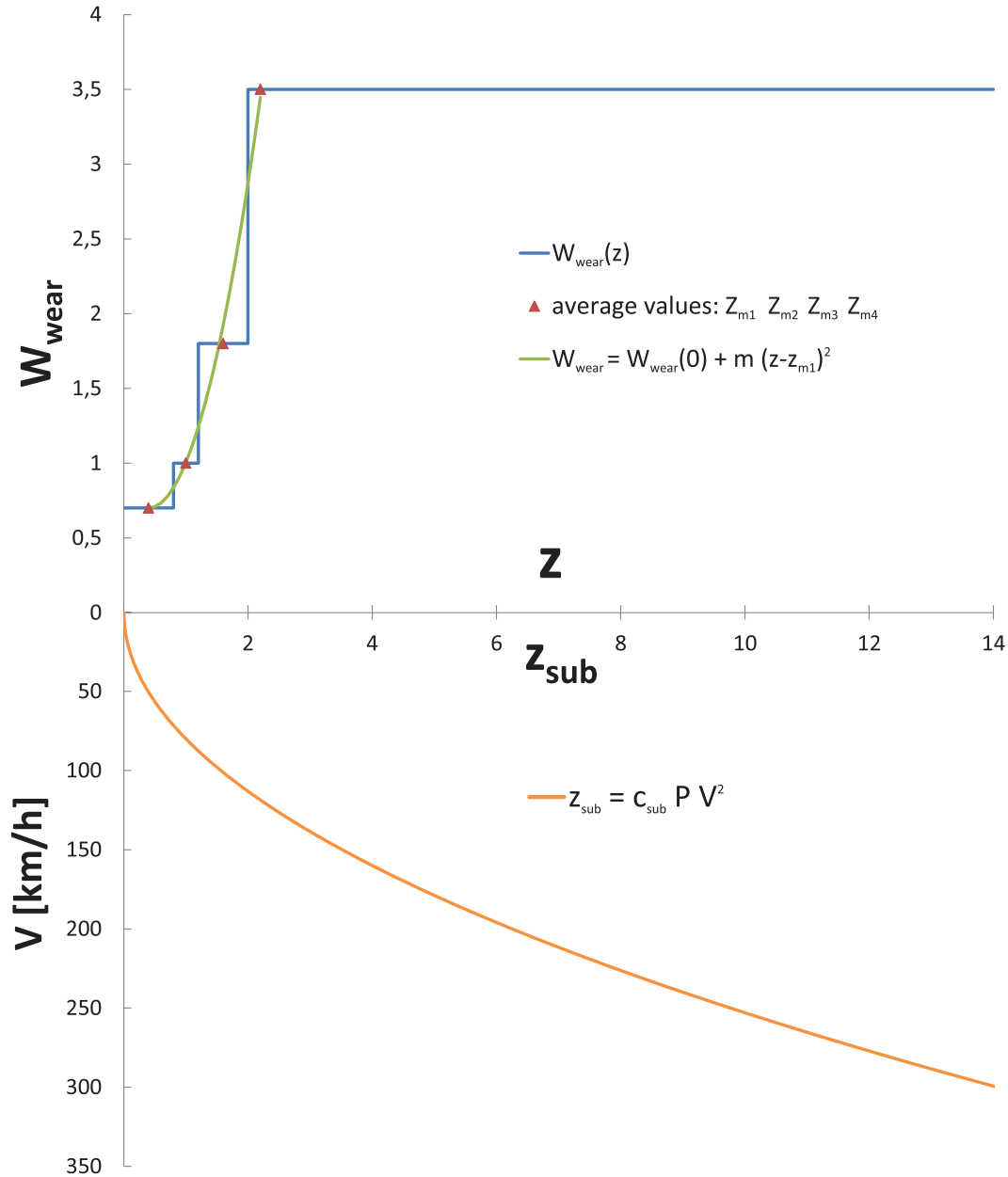


Figure 10.1 – Wear weight cost W_{wear} in function of z , and z_{sub} in function of speed.

In figure 10.1 both functions are shown and related to train speed. To edit the charts the train weight has been fixed as $P = 500$ tonn. The W_{wear} is a discrete function of z and so, it will be a discrete function of speed too. It can be said that the cost is fixed under a minimum speed $V(z_1)$, than it increases with the speed by a discrete function, finally it is constant over a maximum speed $V(z_2)$. In the example shown the values of minimum and maximum speeds are $V_{min} = 51 \text{ km h}^{-1}$ and $V_{max} = 119 \text{ km h}^{-1}$. These values are function of P being:

$$V_{min} = \sqrt{\frac{z_1}{C_{sub}P}} \quad V_{max} = \sqrt{\frac{z_3}{C_{sub}P}}, \tag{10.6}$$

Where z_1 and z_3 are shown in table 10.1. To understand the trend of $W_{wear}(V)$ in the $V_{min} - V_{max}$ range the discrete function W_{wear} can be redefined doing a regression between the average values of discrete intervals. In this case the new function \hat{W}_{wear} is

defined as:

$$W_{wear} = f(z) = \begin{cases} W_1 & z < z_1 \\ W_2 & z_1 \leq z < z_2 \\ W_3 & z_2 \leq z < z_3 \\ W_4 & z_3 \leq z \end{cases} \rightarrow \hat{W}_{wear} = g(z) = \begin{cases} W_1 & z \leq z_{m1} \\ h(z) & z_{m1} < z < z_{m4} \\ W_4 & z_{m4} \leq z \end{cases} \quad (10.7)$$

where the average values z_{m2} and z_{m3} are the centers of the intervals $z_1 - z_2$ and $z_2 - z_3$; and the values z_{m1} and z_{m4} are calculated fixing the distance between z_{mi} points:

$$\begin{aligned} z_{m1} &= z_1 - (z_2 - z_1) \\ z_{m2} &= z_3 + (z_2 - z_1) \end{aligned} \quad (10.8)$$

Doing a regression in this range ($z_{m1} - z_{m2}$) a quadratic relationship between W_{wear} and V has been found:

$$W_{wear} = W_{wear}(0) + m(z - z_{m1})^2. \quad (10.9)$$

taking $m = 0.847$ the regression results a good approximation ($R^2 = 0.99$). Now the function $W_{wear}(V)$ can be defined in this range as:

$$\hat{W}_{wear} = h(z) = W(0) + mz_{m1}^2 - 2mc_{sub}PV^2 + mc_{sub}^2P^2V^4. \quad (10.10)$$

A chart of this function is shown in figure 10.2.

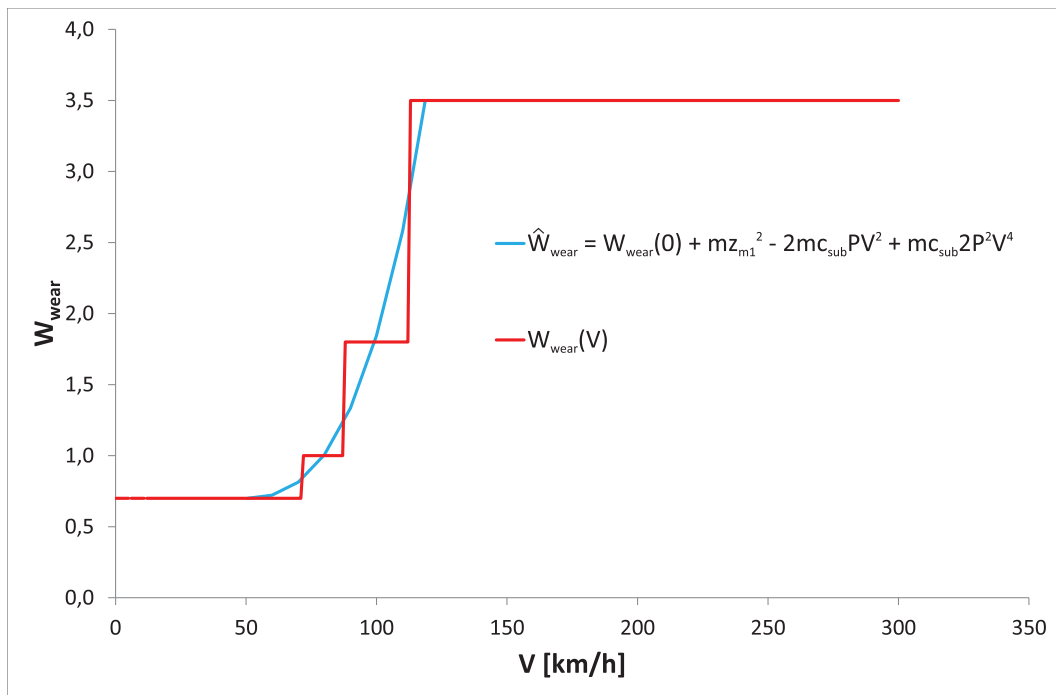


Figure 10.2 – Wear weight cost W_{wear} in function of speed V .

This function evidences the strong proportionality (almost 4th degree) between wear costs and train speed. As shown in next paragraph, this hypothesis results to much strong and discordant to reality. Indeed the part of wear cost, that is the biggest part of total wear cost, has a different relationship with train speed.

10.3 THE BALLAST SETTLEMENT PHENOMENON

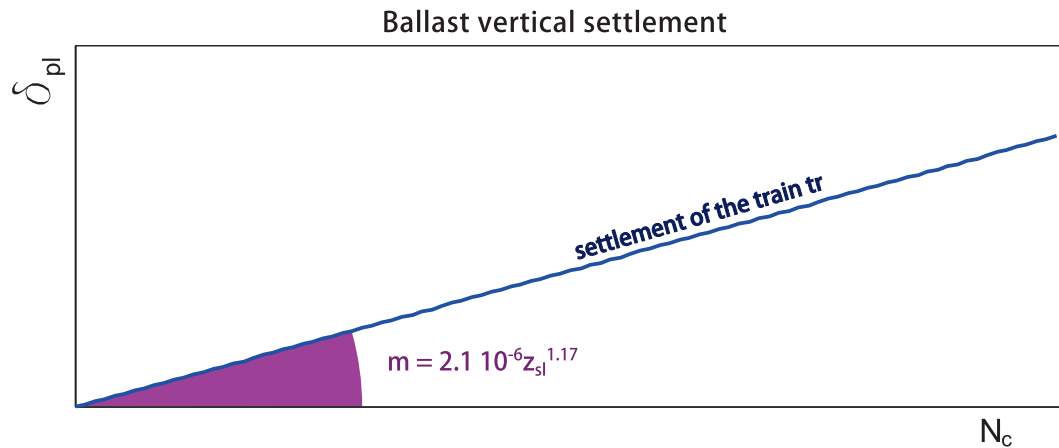
Many studies [14, 56, 68, 27, 8, 9] show how the ballast vertical settlement is proportional to the elastic deflection caused by each wheel pass and the number of applied wheel loads. [14] and [27] have proposed a linearly proportion between settlement and load cycles after a phase of stabilization. They have noticed that the duration of this phase (almost 50,000 – 100,000 cycles) is related to the type of ballast intervention adopted: tamping or stoneblowing (see annex A.2). Bodin-Bourgoin et al. [14] and Guerin [27] have expressed the derivative of ballast settlement in function of two variables: the number of load cycles and the elastic deflection; as:

$$\begin{aligned} \frac{\partial \delta_{pl}}{\partial N_c} &= a z_{sl}^b, \\ \delta_{pl} &= m N_c \end{aligned} \quad (10.11)$$

where the coefficients a and b are given, N_c is the number of wheel passes, and z_{sl} is the elastic deflection of ballast. Bodin-Bourgoin et al. [14] and Guerin [27] have proposed different values for a and b . Both authors have proposed these empiric formulations interpolating data of experimental tests. The tests have been carried out on scale model but only Bodin-Bourgoin et al. [14] have proposed values correcting the scale error. The values suggested by Bodin-Bourgoin et al. [14] are: $a = 2.1 \cdot 10^{-6}$ and $b = 1.17$. In the model presented in this work the elastic deflection in equation 10.11 equals to the sleeper vertical displacement. Other authors have studied the ballast settlement during the stabilization phase. Indraratna and Salim [33] have proposed the following relation up to 100,000 load cycles:

$$\delta_{pl} = c + d \log N_c. \quad (10.12)$$

Looking equations 10.11 and 10.12 some considerations can be done. In the first phase (almost 100,000 load cycles) the ballast settlement increases very fast with load cycles. Paderno [56] has noticed the same behavior carrying out tests on a 1 : 1 scale model. Then, once this phase is finished, the increasing ratio appears stabilized and the settlement is linearly proportional to load cycles. Looking the equations 10.11 and 10.12 only the second one seems to represent this fact. In truth the equation 10.11 considers this behavior implicitly. Indeed as shown by Paderno [56] the ballast stiffness grows quickly in the first phase after every maintenance intervention. Consequentially the elastic deflection decreases. The elastic deflection caused by the train tr can be evaluated once the substructure variables are fixed. If a reference train (with a reference speed and weight) is chosen, it is possible to edit the trend of ballast settlement in function of the number of wheel passes. Similarly it is possible to edit the trend for the train tr . An example of trend is shown in figure 10.3. The angular coefficient is more than proportional to elastic deformation.



Every Infrastructure Manager fixes the limits of intervention for the ballast settlement. The ballast settlement is often connected to the vertical alignment VA . The vertical alignment is an index of the surface uniformity in the vertical plane. In tables 10.2 and 10.3 the limits of intervention of the vertical alignment VA for the Italian and French infrastructure are shown.

Limit of intervention in Italy	
speed range [km h ⁻¹]	values [mm]
200 – 250	10 < VA ≤ 14
160 – 200	11 < VA ≤ 20
120 – 160	12 < VA ≤ 20
< 120	15 < VA ≤ 22

Table 10.2 – Intervention limits of vertical alignment VA for the Italian infrastructure

Limit of intervention in French	
speed range [km h ⁻¹]	values [mm]
220 – 300	$VA_{10-15} \pm 9$
220 – 300	$VA_{15-20} \pm 12$
220 – 300	$VA_{25-35} \pm 18$
160 – 220	± 9
120 – 160	± 10
80 – 120	+10, -15
40 – 80	+10, -20
< 40	± 25

Table 10.3 – Intervention limits of vertical alignment VA for the French infrastructure

The VA index can be evaluated measuring the vertical deflection of the rail at the midpoint of a chord positioned along railhead. The length of chord is 10 m in Italy and in French too. The only difference occurs in the high lines (220 – 300 km h⁻¹). In this range the French Infrastructure Manager applies different base to evaluate the VA index longer bases (10 – 15 m, 15 – 20 m, 25 – 30 m) as seen in table 10.3. Once the limit of vertical alignment is passed, the maintenance of ballast is necessary. In worst cases,

when the life of ballast approach to its end, a total substitution is preferred to the maintenance intervention. Indeed the frequency of interventions increases proportionally to the age of ballast. A typical scheme of ballast interventions following the Veit model [?] is shown in figure 10.4.

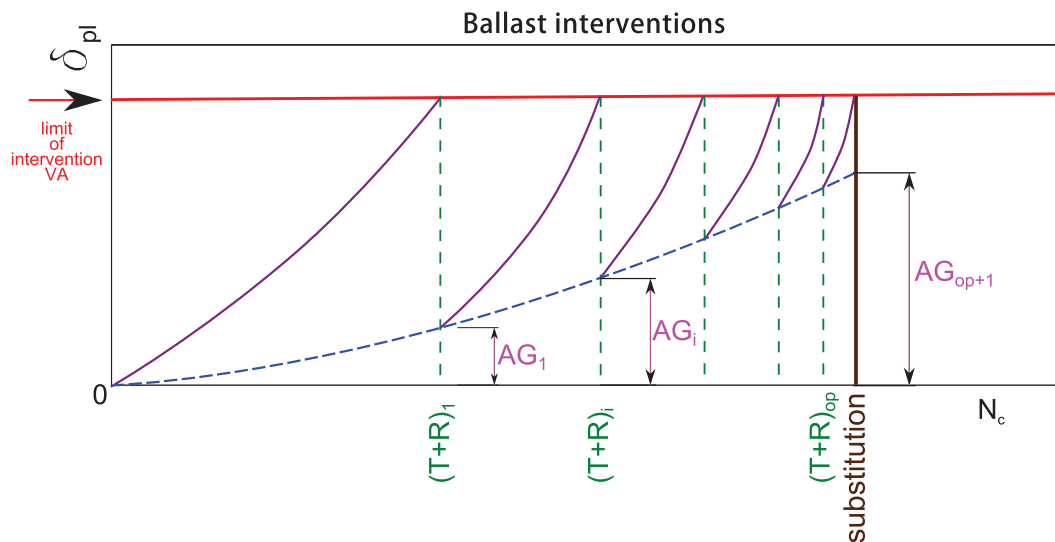


Figure 10.4 – Scheme of ballast interventions.

In this figure the green dotted lines represent the interventions of tamping and regulation ($T + R$), the violet line is the trend of vertical alignment, the blue dotted line represents the aging effect. The aging of ballast is caused directly and indirectly by the trains traffic. By a direct way, trains traffic affects the wear of ballast with vibration and dynamic loads; this fact is 30% responsible of ballast aging. Indirectly, the train traffics causes maintenance intervention to restore the correct vertical alignment of the track. These interventions are 60% responsible of ballast aging [?].

10.4 THE COST OF SETTLEMENT: A NEW FORMULATION FOR THE RAILWAY TOLL

The aim of this paragraph is to suggest a renovation for the toll cost functions. In particular the function proposed will affect the wear costs related to ballast maintenance. The maintenance of ballast represents the 40 – 50% of the total maintenance costs [56]. The French group SNCF estimates a cost of 9,500 € km⁻¹ for the maintenance operation of ballast tamping and regulation; and a cost of 710,000 € km⁻¹ for the substitution [52]. These costs are so high because the largest part of works has to be executed during the night. In order to propose a new formulation some important considerations done in past paragraphs are here resumed:

- the cost of ballast maintenance is proportional to the grow rate of ballast settlement;
- the grow rate of ballast settlement is proportional to elastic deflection (equation 10.11);
- The elastic deflection depends on substructure parameters, train parameters and it varies with velocity (figure 9.8(a));

- the substructure parameters are affected by age (equation 10.12 and [?]);
- the elastic deflection is affected by ballast age;
- the ballast aging implies an increasing of settlement grow rate.

The cost per kilometer connected to a vertical alignment limit $\$_{VA}$ can be calculated as:

$$\$_{VA} = \sum_{i=1}^{op} \$_{t+r}^i + \$_s \quad [€ km^{-1}], \quad (10.13)$$

where op represents the number of maintenance operations of ballast tamping and regulation done before the substitution, $\$_{t+r}^i$ is the cost for the tamping and regulation ($9,500 € km^{-1}$), and $\$_s$ is the cost for the substitution ($710,000 € km^{-1}$). Then it is possible to evaluate the cost for unit of ballast settlement $\$_{bs}$:

$$\$_{bs} = \frac{\$_{VA}}{VA (op + 1) - \sum_1^{op+1} AG_i} \quad [€ km^{-1} mm^{-1}], \quad (10.14)$$

where AG_i is the part of settlement that cannot be restored even with the intervention (see figure 10.4). Finally the toll cost for the train tr could be calculated as:

$$\$_{toll}^{tr} = \$_{bs} \Delta \delta_{pl}^{tr} \quad [€ km^{-1}], \quad (10.15)$$

where $\Delta \delta_{pl}^{tr}$ is the settlement caused by the pass of the train tr . It can be calculate from equation 10.11 as:

$$\Delta \delta_{pl}^{tr} = 1.44 \cdot 10^{-6} [z_{zsl,loco}^{2.51} N_{axles,loco}^{tr} + z_{zsl,wagon}^{2.51} N_{axles,wagon}^{tr}] \quad [mm], \quad (10.16)$$

where $N_{axles,loco}^{tr}$ is the axles number of the train locomotive tr and $N_{axles,wagon}^{tr}$ is the axles number of the train wagon.

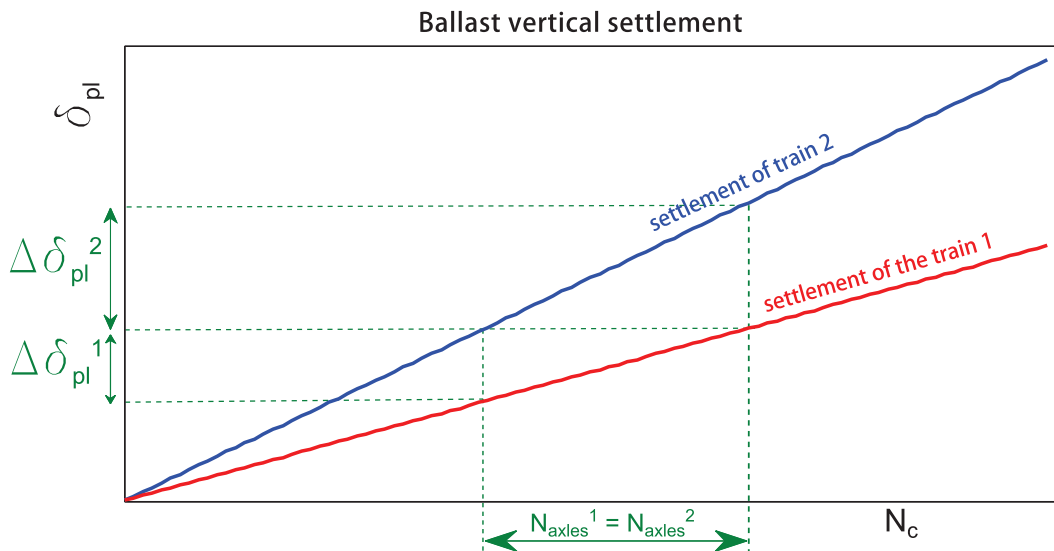


Figure 10.5 – Settlement of ballast caused by the pass of the train tr .

To evaluate the ballast settlement in equation 10.16, we decided to use the equation 10.11 and not the equation 10.12 for two reasons. First, equation 10.12 considers the

aging of ballast, but a train has not to be considered as responsible if it passes when the substructure is old or new. Indeed the objective is to evaluate its effect and it should not vary in function of the moment of transit. Second, in the equation 10.12 no physical variables appear; Indeed c and d are two constants depending on substructure and train but not directly related with some known parameters. On the contrary in equation 10.11 the elastic deflection could be evaluated with present model as seen in paragraph 9.6. Finally we propose an equation, where the toll can be expressed in function of elastic deflection: from equations 10.15 and 10.16:

$$\$_{toll}^{tr} = \$_{bs} 1.44 \cdot 10^{-6} [z_{zsl,loco}^{2.51} N_{axles,loco}^{tr} + z_{zsl,wagon}^{2.51} N_{axles,wagon}^{tr}] [\text{€ km}^{-1}]. \quad (10.17)$$

The toll function cost in equation 10.17 represents the most common situation in which only two type of axles (one for the locomotive and one for other wagons) are present. If the train has a complex composition, and not only two type of axles are present, the equation for the toll cost can be becomes:

$$\$_{toll}^{tr} = \$_{bs} 1.44 \cdot 10^{-6} \sum_1^{ty} z_{sl,ty}^{2.51} N_{axles,ty}^{tr} [\text{€ km}^{-1}], \quad (10.18)$$

where the subscript ty index the type of axle. The values of $\$_{bs}$ and N_{axles}^{tr} are simple to evaluate; on the contrary z_{sl} depends on train characteristics, substructure type, and especially the speed of train. Anyway for a chosen train and a chosen substructure, the only variable of interest is the speed of transit of the train. Only numerical method, as the one presented in this work, can give a good reliability of elastic deflection in function of speed. In figure 9.8(b) we have seen the function $Z_{sl}(V)$. From these values it is easy to edit the curve $\$_{toll}^{tr}(V)$. In the figure 10.6 an example of toll function cost is shown.

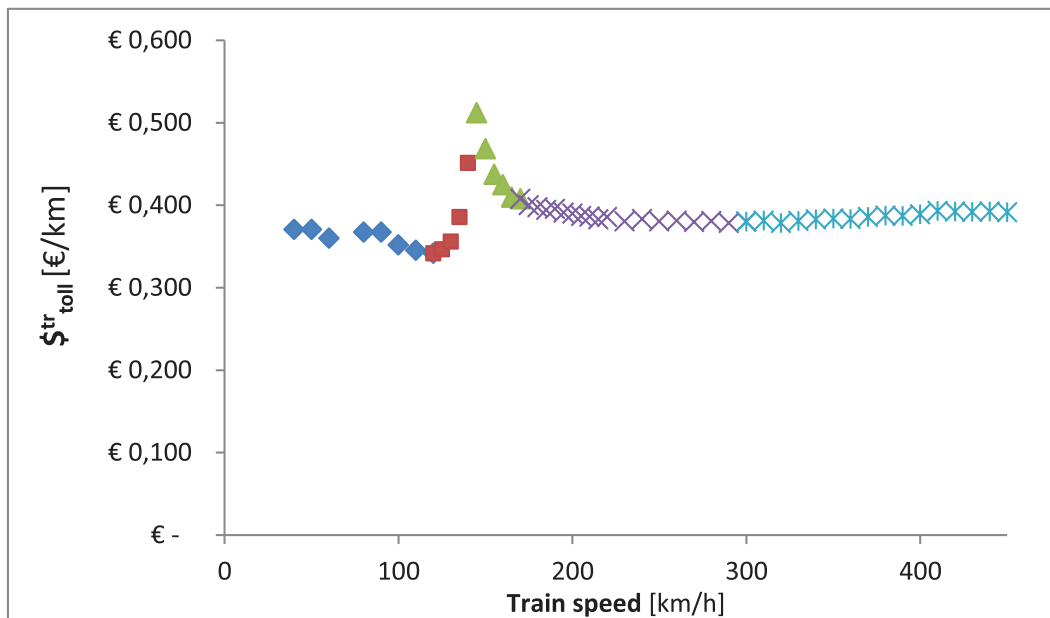


Figure 10.6 – Example of toll in function of train speed.

For this example the values reported in table 10.4 are adopted.

parameter	value
<i>op</i>	20
<i>VA</i>	12
N_{axes}^{tr}	20
<i>ty</i>	1

Table 10.4 – *Values adopted for the toll function cost example.*

The values adopted for the substructure and the train, are the input variables used for the sensitivity analysis (see figure 9.1).

A RECEPTANCE ANALYSIS FOR THE COUPLED VEHICLE / TRACK SYSTEM

11.1 INTRODUCTION

The problem to study the response of substructure to the variation of train speed equals, for many points of view, to study the substructure reaction to different excitation frequencies. During motion the contact force is subjected to variate with two causes of excitation:

- the rail deflection (that varies along the motion direction);
- the rail corrugations.

Moreover if we see the contact force registered on a fixed point of the rail, the excitation is an impulsive force present when a wheel passes over the point. In this case the frequencies of excitation are caused by:

- the wheel-base;
- the boogie-base.

On the other side the response of the substructure could be studied by a modal analysis. The study of receptance view in paragraph 7 gives some important informations about the substructure behavior. Anyway it cannot be enough to understand the response of track during a train pass. Indeed train masses and suspension play an important role during the contact with track, modifying its response. Then it results necessary to do a receptance analysis of the coupled structure, considering both systems: train and substructure. Many positions of train and many points of excitation have been combined to do the analysis.

11.2 TRAIN AT THE CENTER OF TRACK

In the first combination the train has been positioned to the center of track. Both midspan excitation and on-sleeper excitation have been tested to analyze the receptance. A draft of these combinations is shown in figure 11.1.

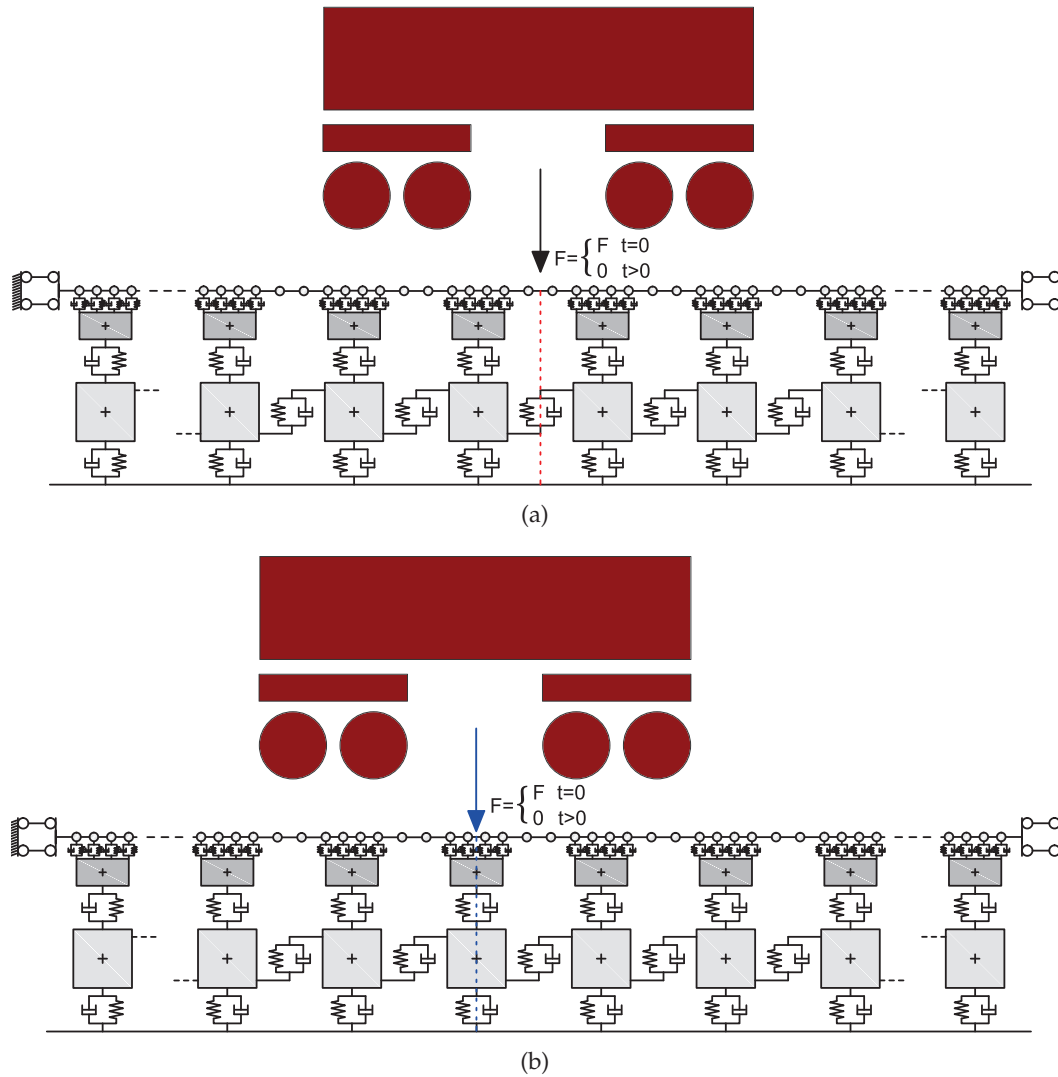
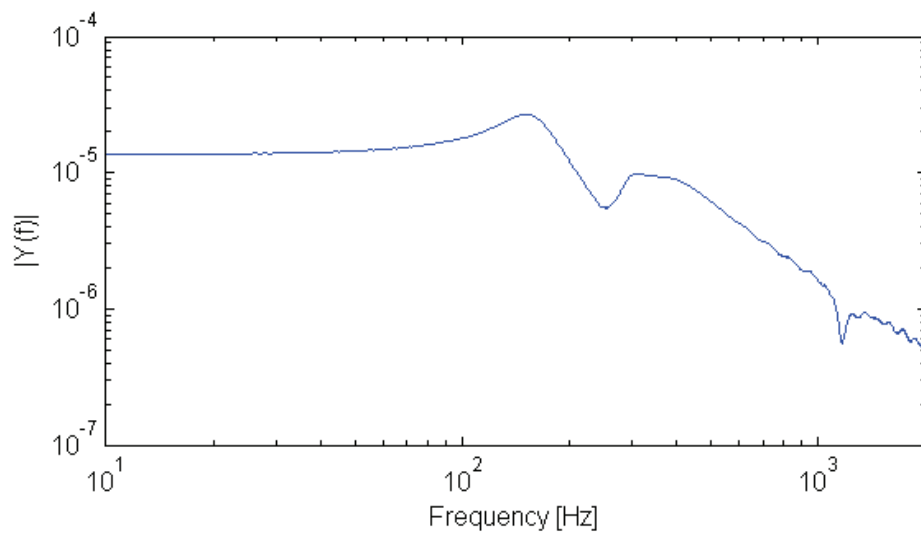
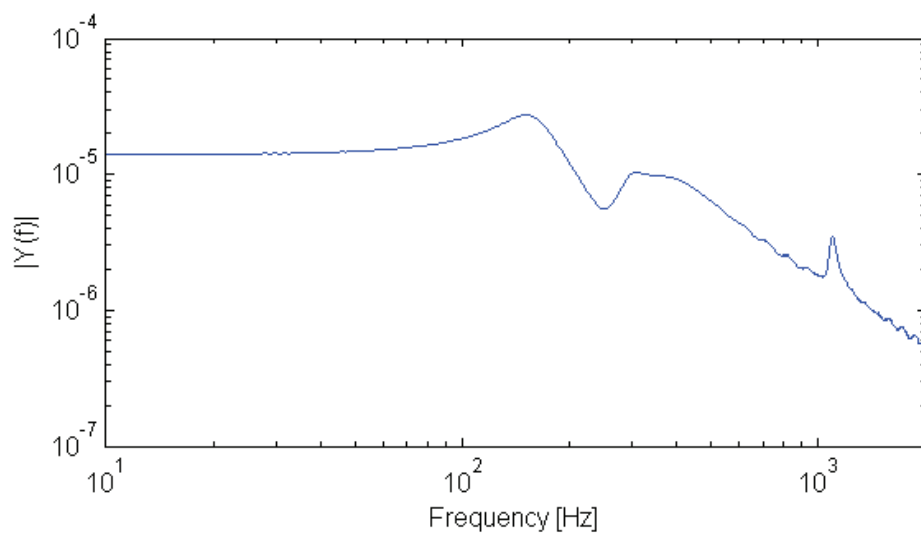


Figure 11.1 – Type of excitation for the receptance simulation: (a) centered train, midspan excitation; (b) centered train, on-sleeper excitation.

In this case the receptances measured aren't very different from the ones measured without train. The results are shown in figure 11.2. The peaks rest in the same position but with smaller value. It can be concluded that the wheels are far enough from the point of excitation and they don't modify the natural frequencies of the structure. However they influence their amplitudes. Indeed the only effect observed is an increasing of damping. In figure 11.3 the waves propagation in time and in space, in the case of on-sleeper excitation, is shown.



(a)



(b)

Figure 11.2 – Analysis of receptance of the coupled system for different combinations: (a) centered train, midspan excitation; (b) centered train, on-sleeper excitation.

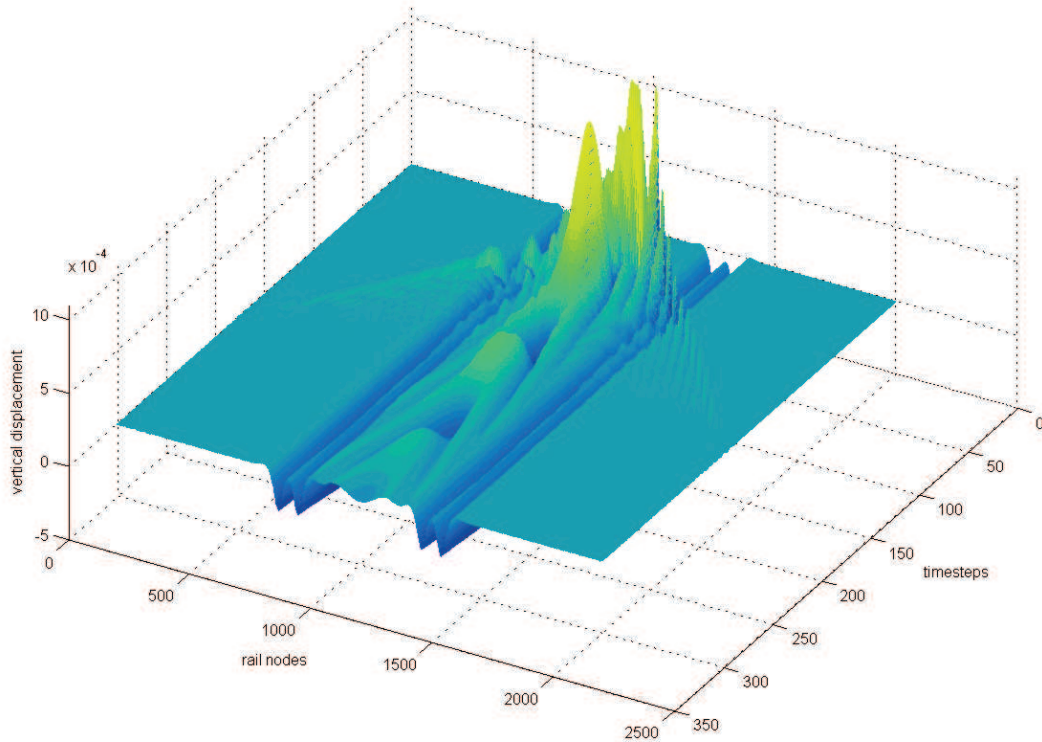


Figure 11.3 – *Waves propagation in time and in space in the case of centered train, on-sleeper excitation.*

11.3 THIRD WHEEL AT THE CENTER OF TRACK

In the second combination the third wheel has been positioned to the center of track. Both midspan excitation and on-sleeper excitation have been tested to analyze the receptance. A draft of these combinations is shown in figure 11.4. Maybe this combination represents the most important receptance analysis. The impulsive force is applied in the same position of the contact force. The study of receptance in this case is more useful because it represents the response to the contact force. On the contrary in any case a load will be applied between wheels (as seen in paragraph 11.2).

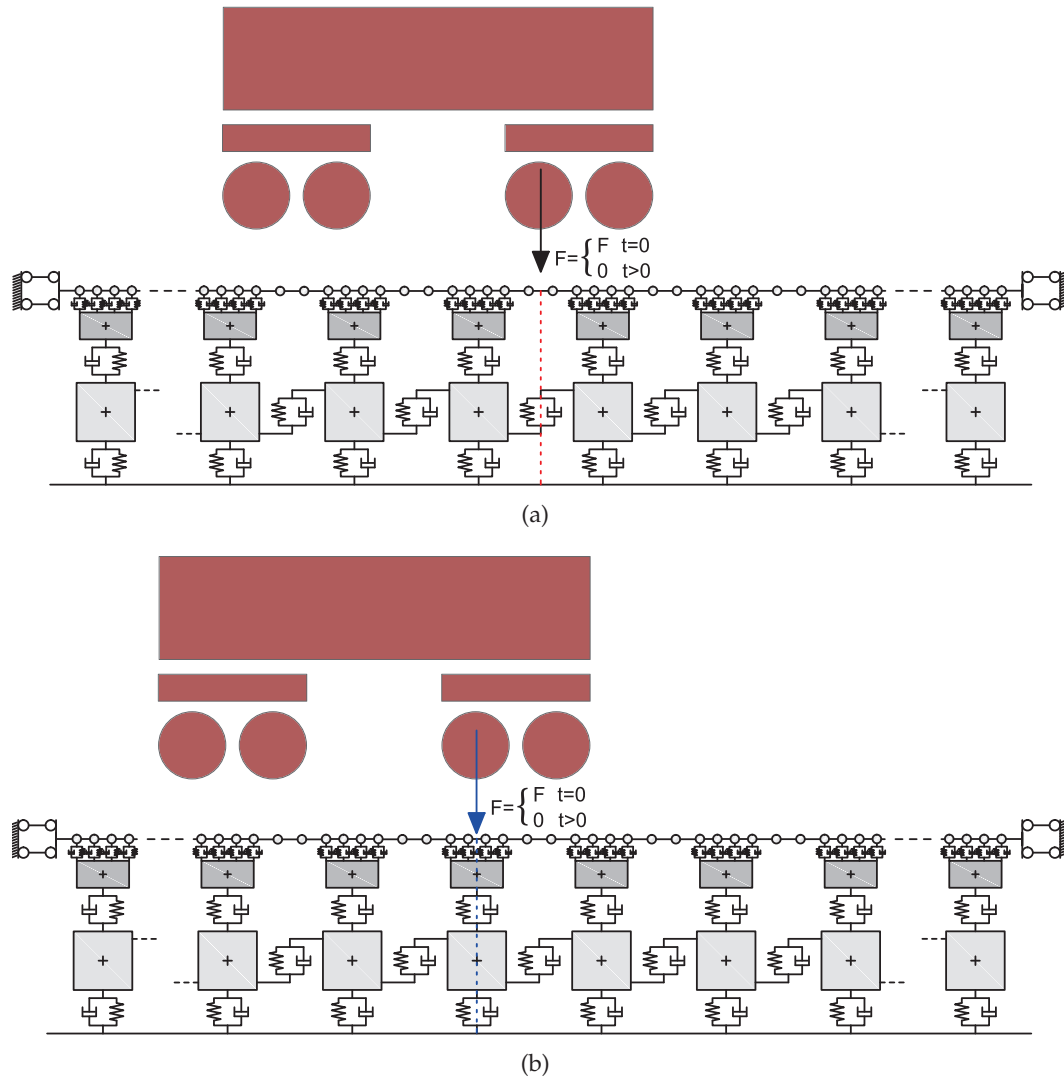


Figure 11.4 – Type of excitation for the receptance simulation: (a) centered third wheel, midspan excitation; (b) centered third wheel, on-sleeper excitation.

The results are totally different if compared to ones without the train. The receptance reveals one singular peak in a low frequency range 50 – 120 Hz (see figures 11.7, 11.9, 11.11, 11.13). The wave propagation in time and space are shown in figure 11.5.

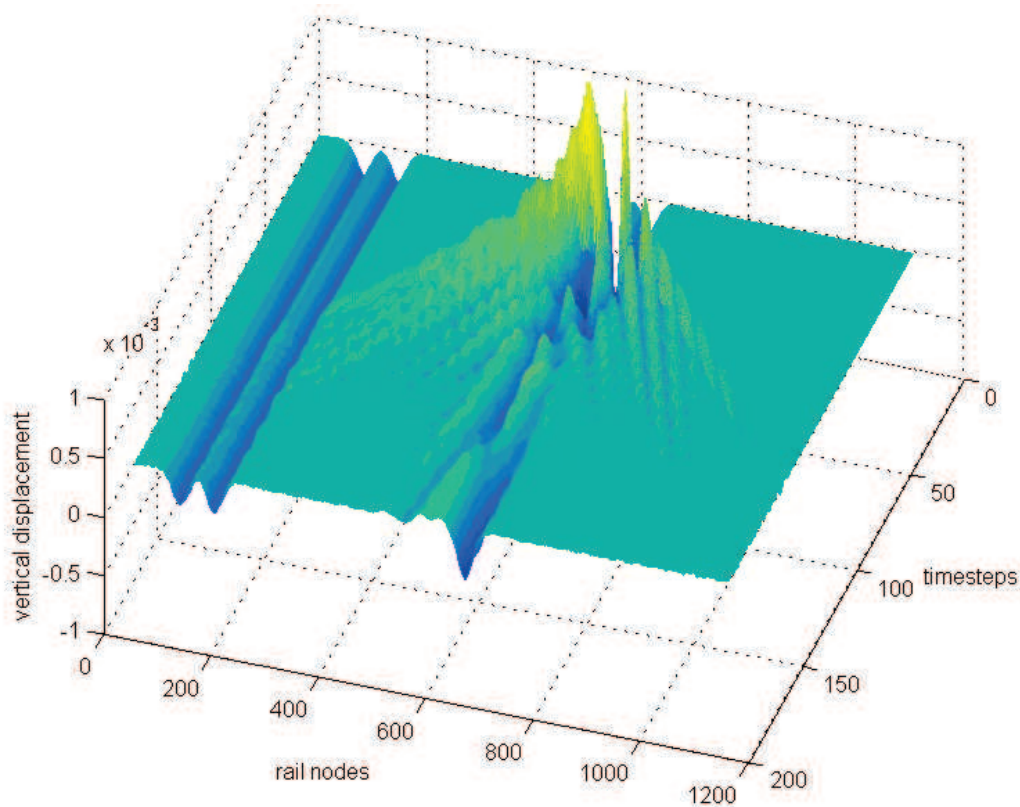


Figure 11.5 – *Waves propagation in time and in space in the case of centered third wheel, on-sleeper excitation.*

The results of four scenarios are presented in following paragraphs, two different types of vehicle are combined with three types of substructure.

11.3.1 Scenario 1

In the first scenario the vehicle type Manchester Benchmark has been chosen. The values adopted for the substructure correspond to the values x_{max} in figure 9.1 and the rail adopted is the 50E5 type (see table 3.4). Looking at figure 11.7(a) a resonance frequency can be recognized at about 69 Hz. Other natural frequencies, even if with a very smaller amplitude, can be recognized at about 230, 390 and 500 Hz. In figure 11.6 the vertical displacement of excited point is shown in function of time steps. Focusing on this figure 11.6 it can be seen how, after few time-steps (red dotted line), all frequencies have been damped except the one at 69 Hz. This fact is confirmed in figure 11.7(b), where the FFT algorithm has been applied only in the part of function after the red dotted line. In this case a clear peak is present at the frequency of 69 Hz.

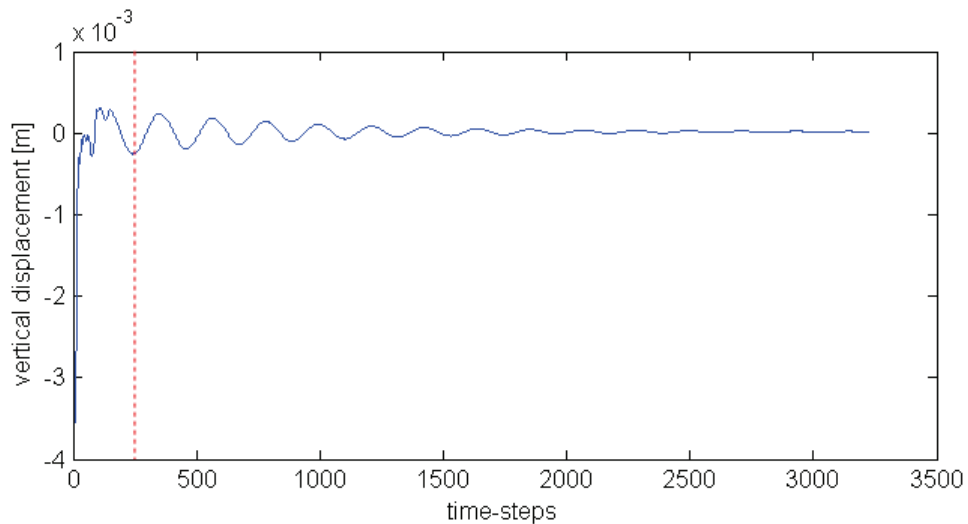


Figure 11.6 – Vertical displacement for the receptance analysis in the scenario 1.

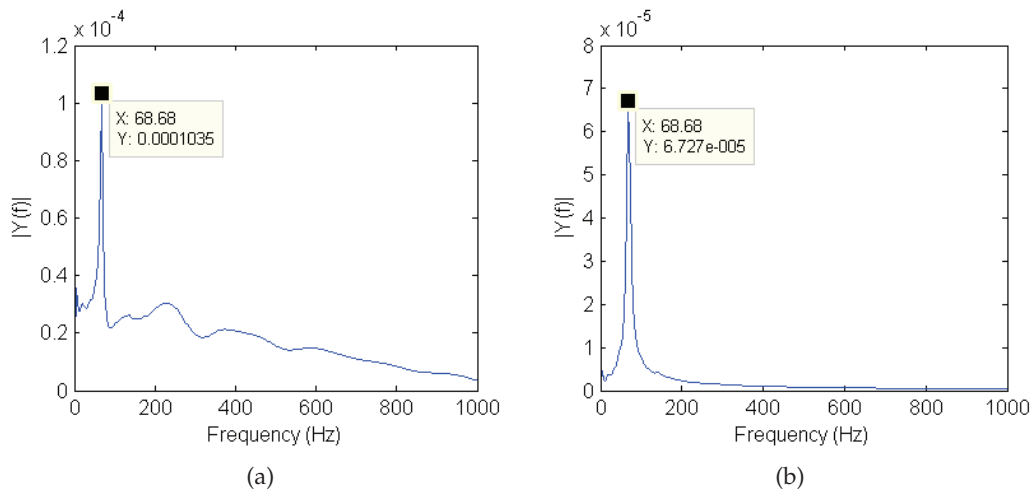


Figure 11.7 – Comparison between: (a) the receptance considering all time-steps and (b) the receptance considering stabilized part in the scenario 1.

11.3.2 Scenario 2

In the second scenario all the values adopted are the same of scenario 1 except the type of rail. In this scenario a 60E1 (see table 3.4) type has been adopted. The behavior observed is the same described as in the scenario 1. The vertical displacement of excited point is shown in figure 11.8. The receptance analysis are shown in figure 11.9. Even in this case a receptance analysis of the vertical displacement after the damping of higher frequencies is shown in figure 11.9(b).

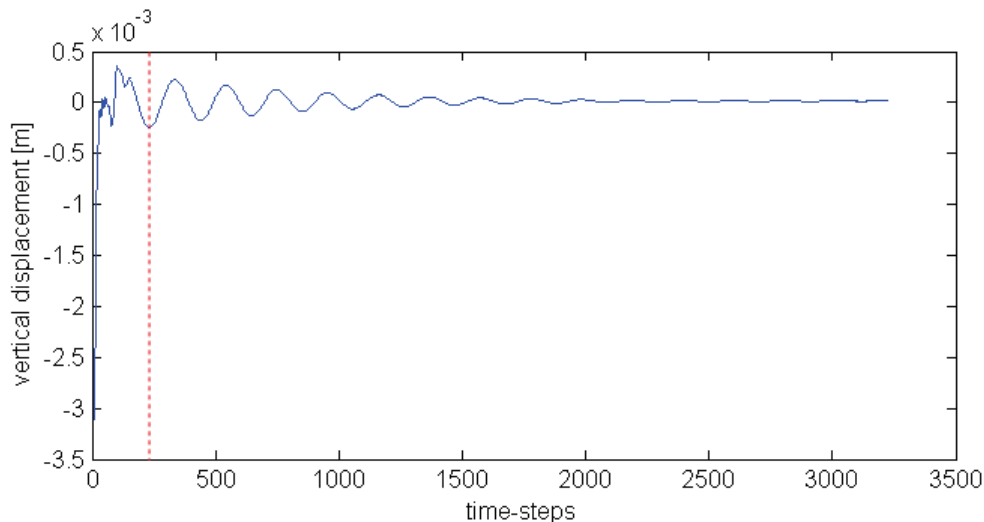


Figure 11.8 – Vertical displacement for the receptance analysis in the scenario 2.

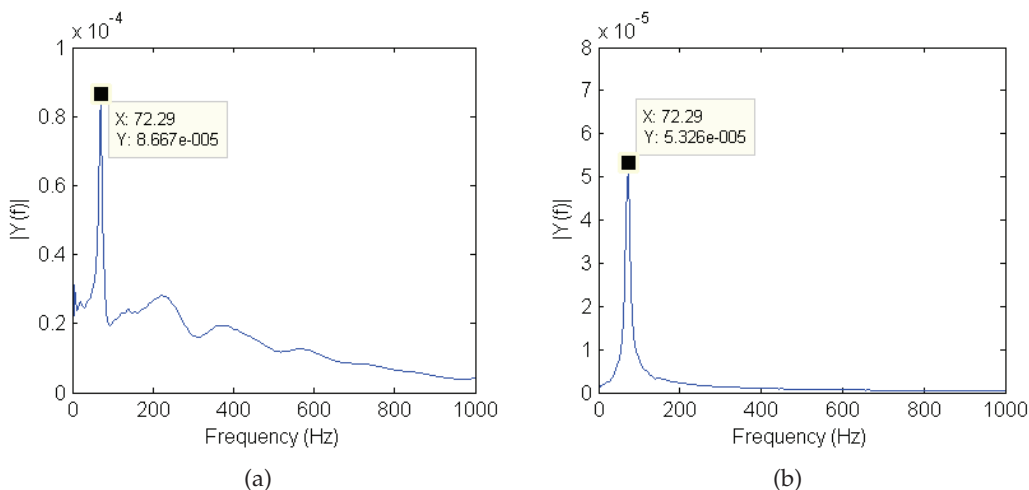


Figure 11.9 – Comparison between: (a) the receptance considering all time-steps and (b) the receptance considering stabilized part in the scenario 2.

11.3.3 Scenario 3

In the third scenario the vehicle adopted is the ALN668 locomotive. The parameters for the train model are those reported in table 8.1. The values adopted for the substructure are the x_0 shown in figure 9.1. The vertical displacement of excited point is shown in figure 11.10. The receptance analysis are shown in figure 11.11. Even in this case a receptance analysis of the vertical displacement after the cut-off of higher and smaller frequencies is shown in figure 11.9(b).

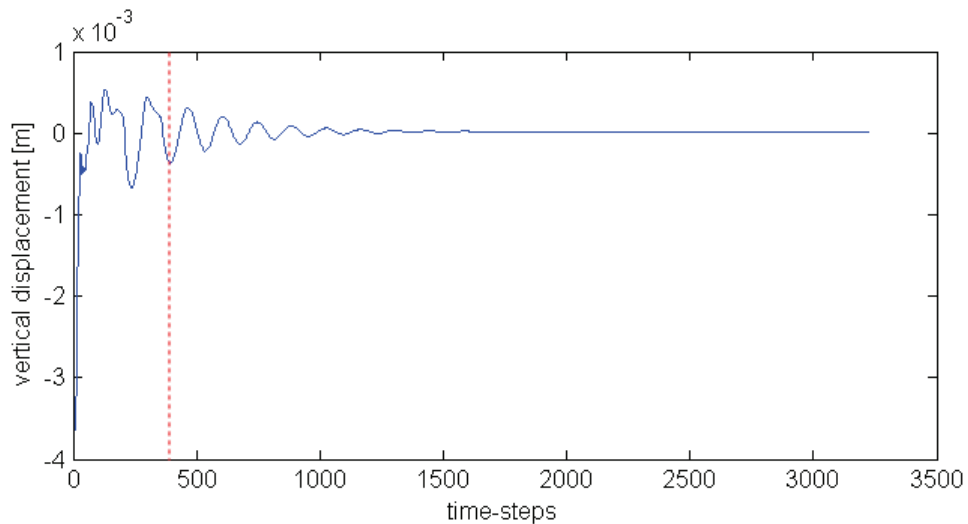


Figure 11.10 – Vertical displacement for the receptance analysis in the scenario 3.

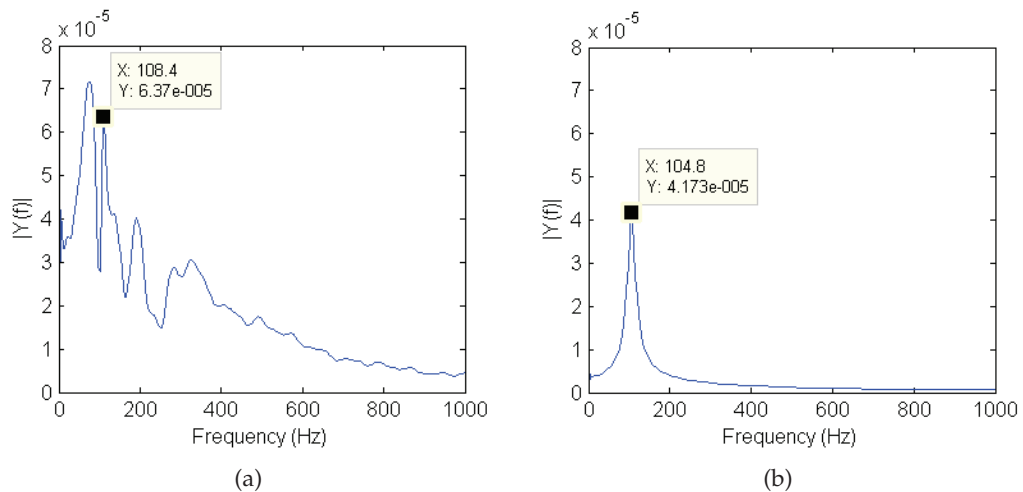


Figure 11.11 – Comparison between: (a) the receptance considering all time-steps and (b) the receptance considering stabilized part in the scenario 3.

11.3.4 Scenario 4

In the last scenario studied, all values adopted (for the vehicle and substructure) are those used in the paragraph 9. The vehicle used is the Manchester Benchmark type. The substructure parameters are the x_0 values of figure 9.1. The rail adopted is the 60E1 type. The vertical displacement of excited point is shown in figure 11.12. The receptance analysis are shown in figure 11.13. Even in this case a receptance analysis of the vertical displacement after the cut-off of the higher frequency is shown in figure 11.13(b).

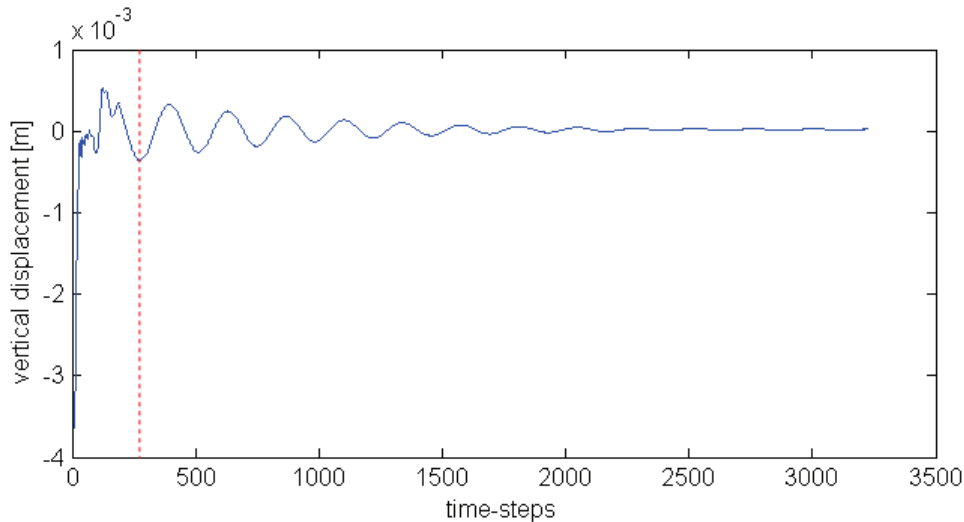


Figure 11.12 – Vertical displacement for the receptance analysis in the scenario 4.

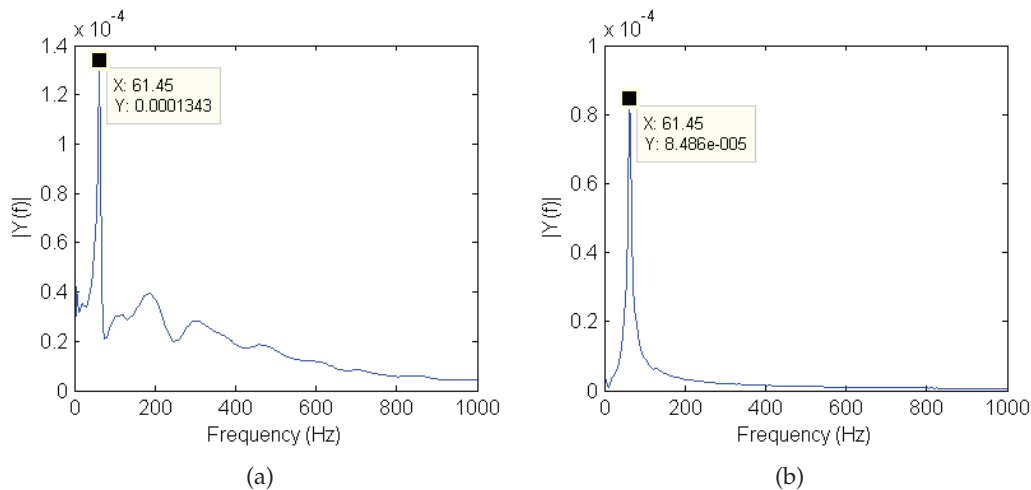


Figure 11.13 – Comparison between: (a) the receptance considering all time-steps and (b) the receptance considering stabilized part in the scenario 4.

11.4 CONCLUSIONS

The presence of the train on the track modifies substantially the response of system to excitation frequency. Looking the receptance of the track with no train shown in figure 7, three resonance frequencies appear in the intervals: 100 – 200 Hz, 400 – 500 Hz and 700 – 1000 Hz. Indeed, focusing on receptance of vehicle/track system (figures 11.7, 11.9, 11.11, 11.13), one singular frequency seems to be the only excitation with induces resonance of the system. Moreover its values is in range very lower (50 – 120 Hz). Consequentially it results suitable to carry out a study of receptance always on the coupled vehicle/track system to analyze the natural frequencies.

A NEW POSSIBLE EXPLANATION OF THE CRITICAL SPEED PHENOMENON

12.1 INTRODUCTION

Field observations and measurements [69] had indicated a so called "Critical Train Speed" in the range $100 - 300 \text{ km h}^{-1}$. At these conditions the moving of trains causes an increasing of vertical and lateral track vibrations. This "mysterious" critical condition is described as the resonance between the moving train and the Rayleigh wave traveling in the soil embankment (analogous to the "Mach" effect caused by flying objects breaking through the sound barrier) [43]. Some authors [76, 7] have affirmed that the problem is more complicated than a simply interaction with the Rayleigh wave in the ground. They have treated the rail as beams on homogeneous half space. Basing on this assumption, it has been found that track should have two critical speeds, one equal to the Rayleigh wave velocity of the ground, and other, fairly close, controlled by the bending stiffness and mass of the rail/embankment "beam" in addition to the ground properties [49]. Green's functions [43, 74, 75], wavelets [46], boundary and finite elements, even with the element net moving with the train [21], have been applied to try to predict track response to trains moving at speeds around the critical value [49]. Anyway a real explanation and a precise calculation of critical speed seems to rest an unresolved problem. Numerical models, and measurements show the amplification of contact force and displacement, but the physical explanations given to this phenomenon seem to be not satisfactory. In following paragraph a new approach and explanation is proposed.

12.2 THE PHENOMENON

The phenomenon of critical speed has been revealed during numerical simulation with the model presented in this work. The effect of critical speed to sleeper vertical displacement and contact force has been shown in paragraph 9.5. The dynamic contact force in function of time steps for different train speeds is shown in figures 12.1, 12.2, 12.3, 12.4 and 12.5. The values adopted are those obtained by the curve fitting method (table 7.1). In these simulations the corrugation has been fixed as a sinusoidal function with amplitude 0.025 mm and wavelength 5 mm.

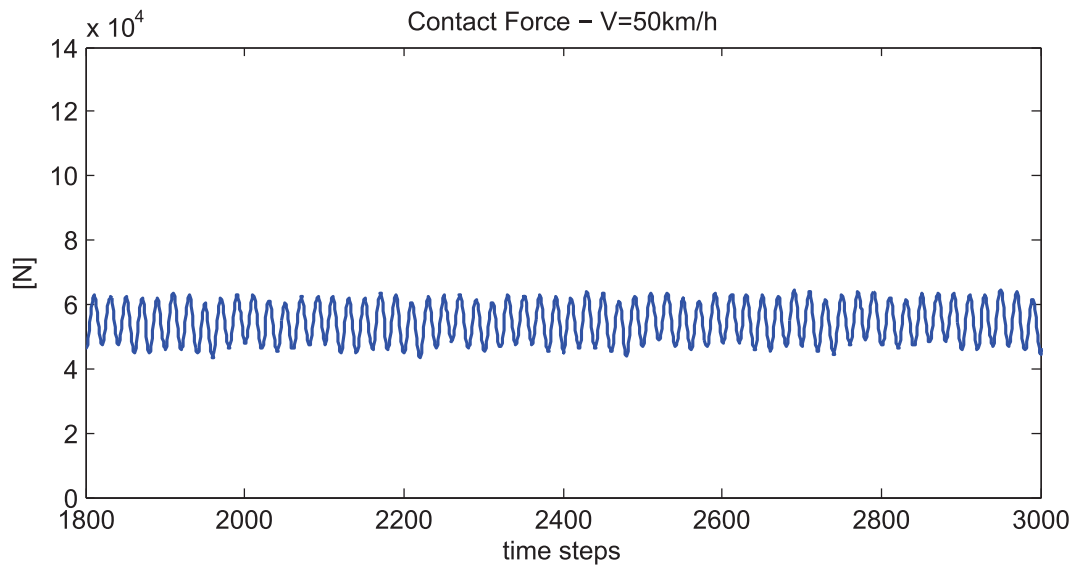


Figure 12.1 – Dynamic contact force in function of time at 50 km h^{-1}

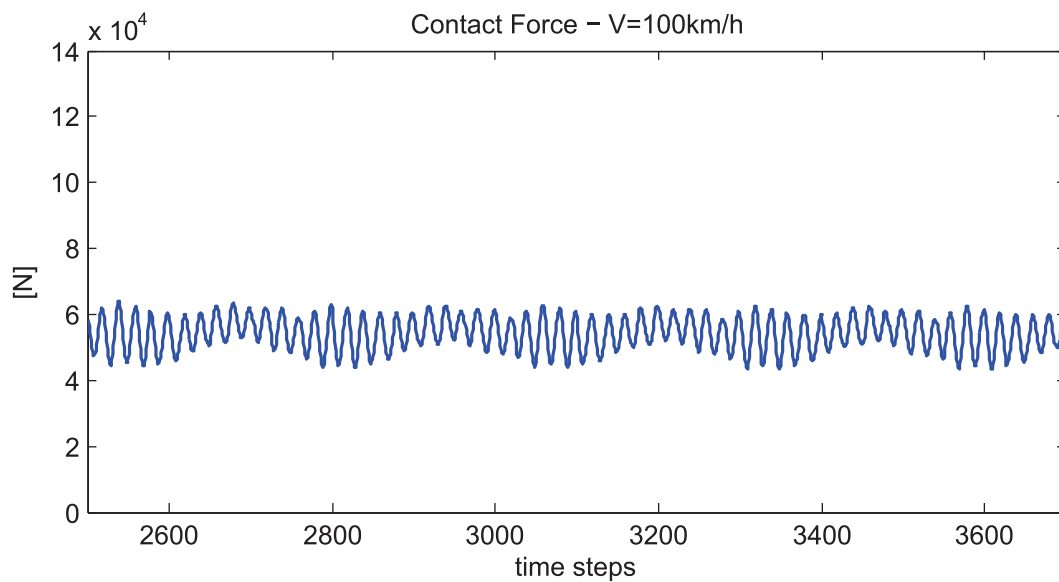


Figure 12.2 – Dynamic contact force in function of time at 100 km h^{-1}

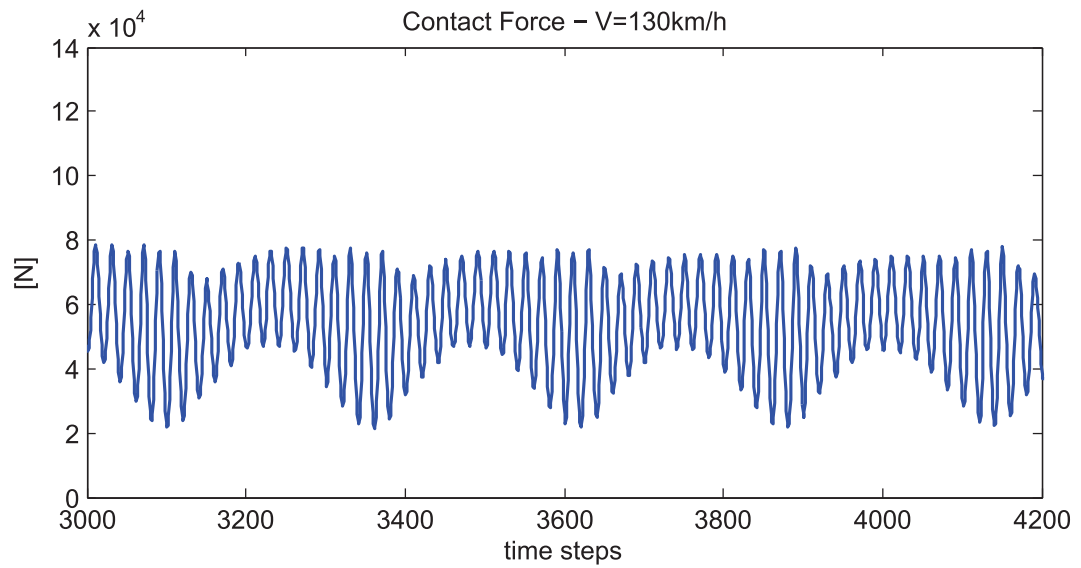


Figure 12.3 – Dynamic contact force in function of time at 130 km h^{-1}

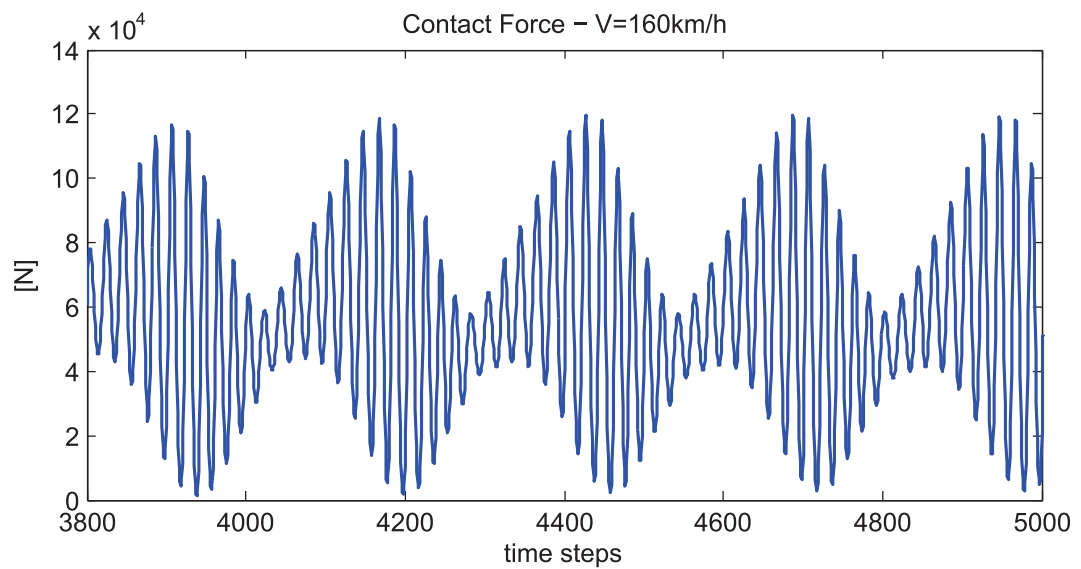


Figure 12.4 – Dynamic contact force in function of time at 160 km h^{-1}

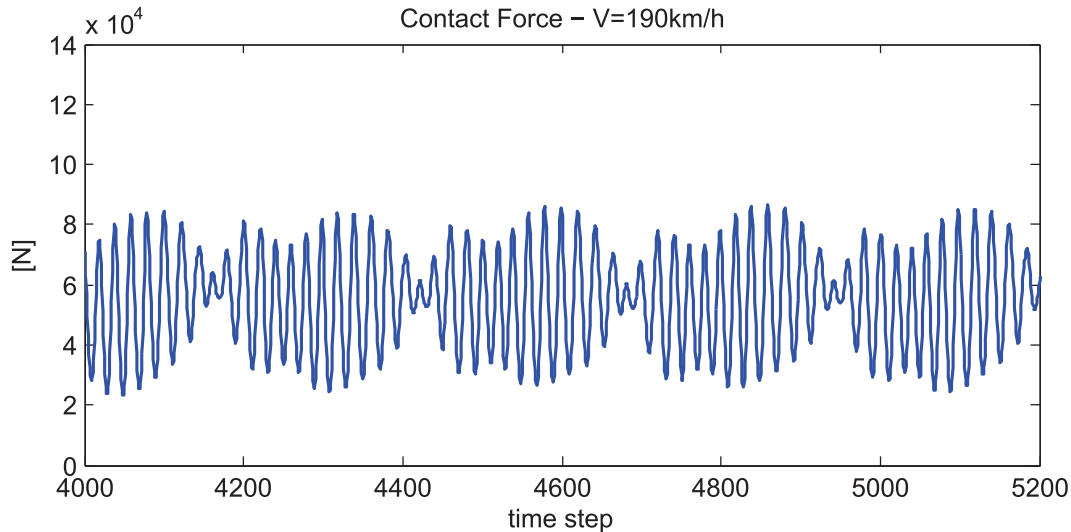
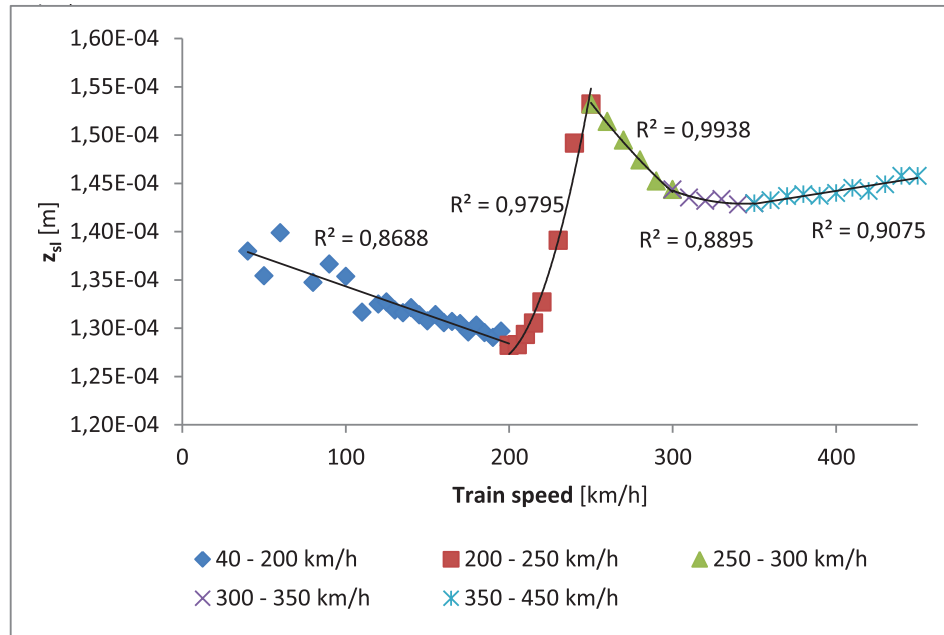


Figure 12.5 – Dynamic contact force in function of time at 190 km h^{-1}

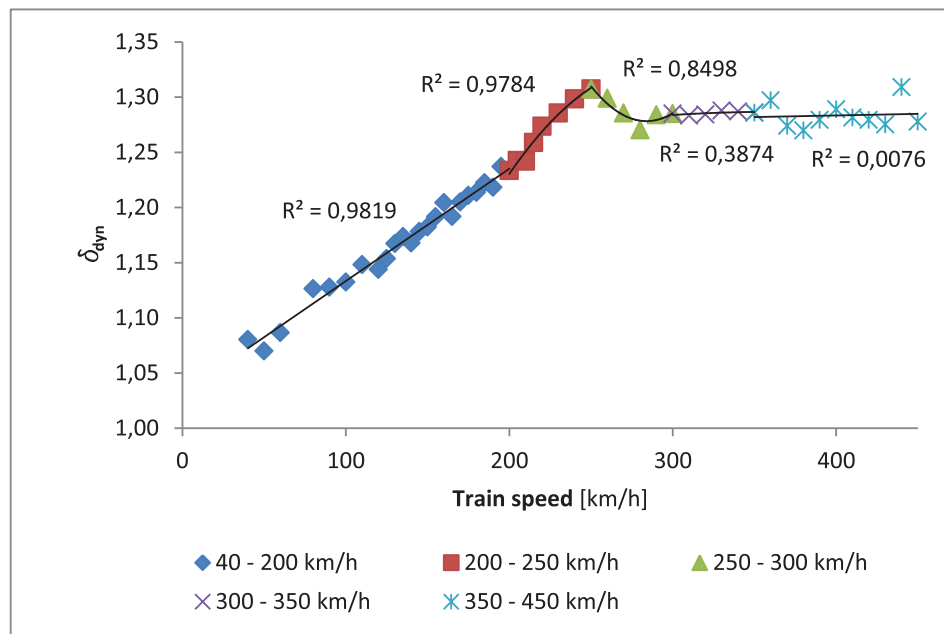
As it can be seen comparing figures, the dynamic effects increase up to 160 km^{-1} and then decrease again. The same phenomenon can be probably more evident looking the dynamic amplification factor and sleeper vertical displacement in figures 12.6, 12.7 and 12.8. The values adopted for the simulation are:

- figure 12.6: the same values adopted in scenario 3 (see paragraph 11.3.3);
- figure 12.7: the same values adopted in scenario 4 (see paragraph 11.3.4);
- figure 12.8: values evaluated by curve fitting (table 7.1) for the substructure and Manchester Benchmark [34] for the vehicle type (it will be called it scenario 5).

In figure 12.6 a critical speed is observed at 250 km h^{-1} in the first and case. In figure 12.7 and 12.8 the critical speed results lower: 145 km h^{-1} . The charts have been cut in five ranges with the same procedure explained in paragraph 9.6. It can be noticed that the critical speed range is $V_c \pm 25$ in the last two cases and $V_c \pm 50$ in the first one. Maybe this interval is larger with the increasing of critical speed.

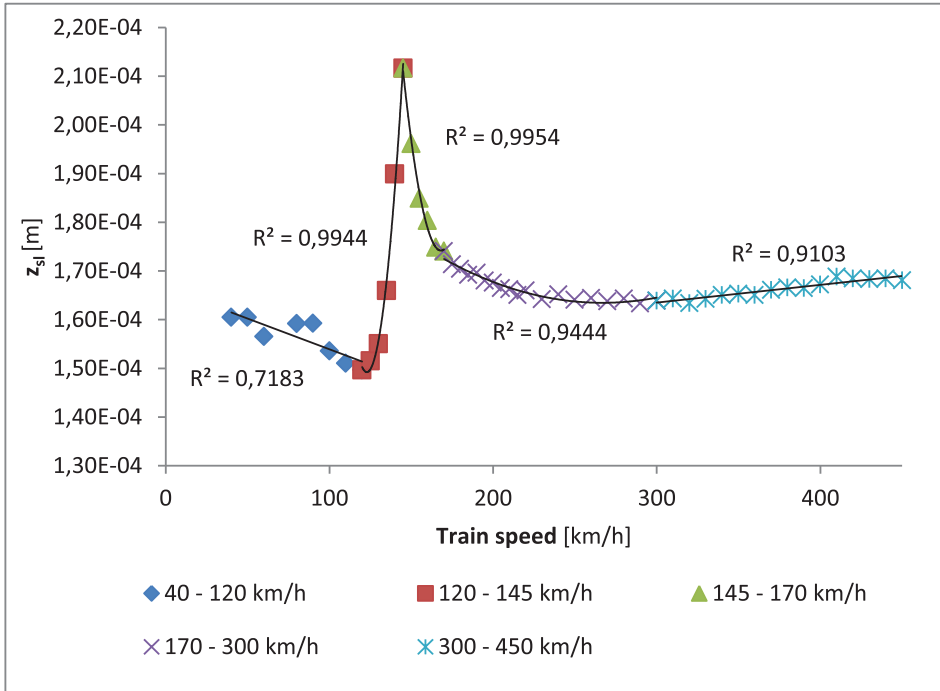


(a)

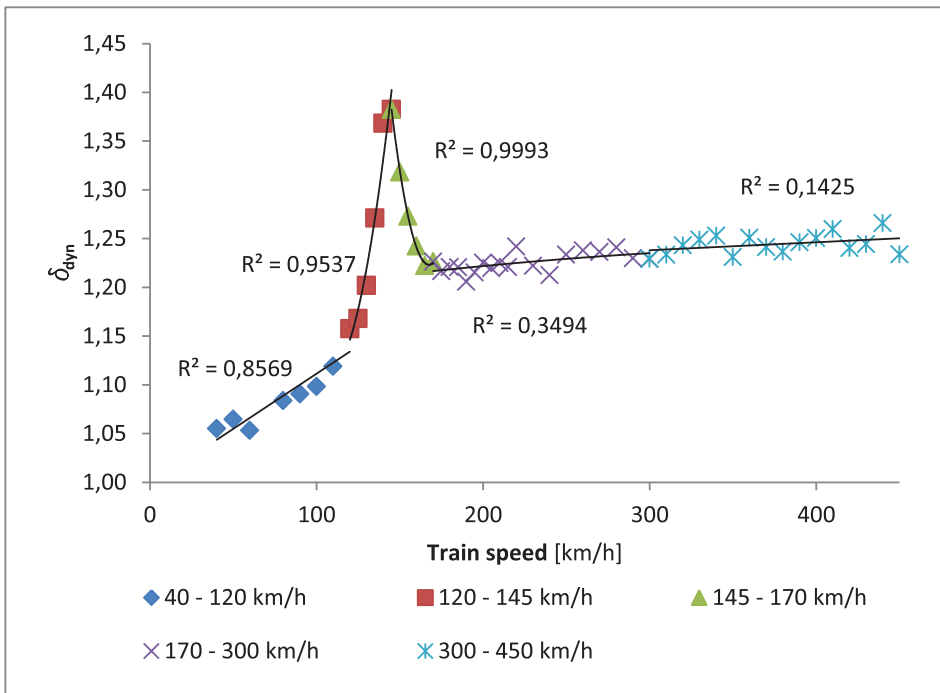


(b)

Figure 12.6 – Scenario 3: (a) sleeper vertical displacement and (b) dynamic amplification factor in function of train speed

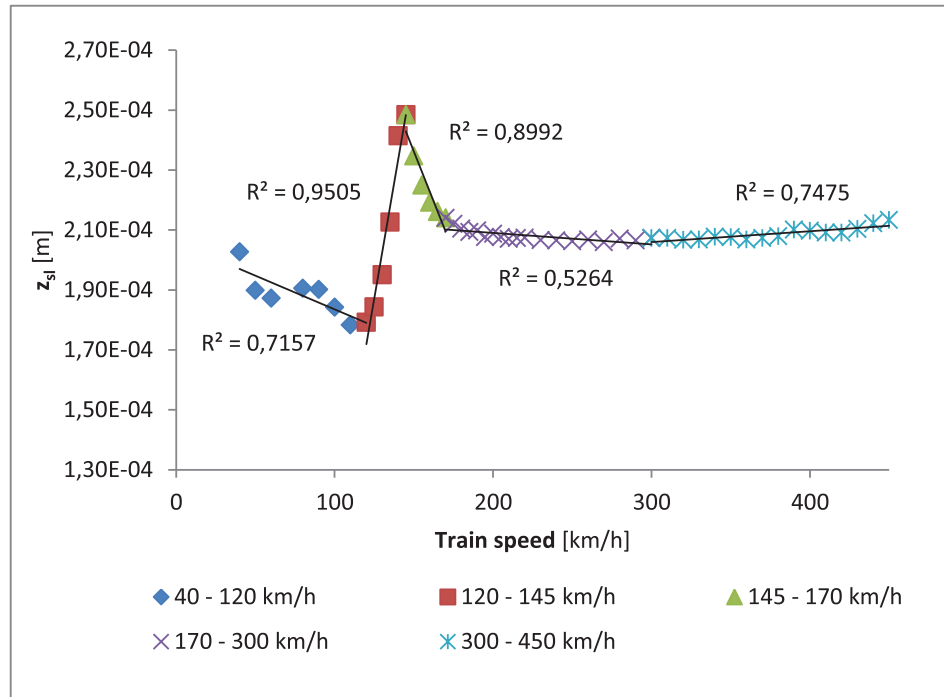


(a)

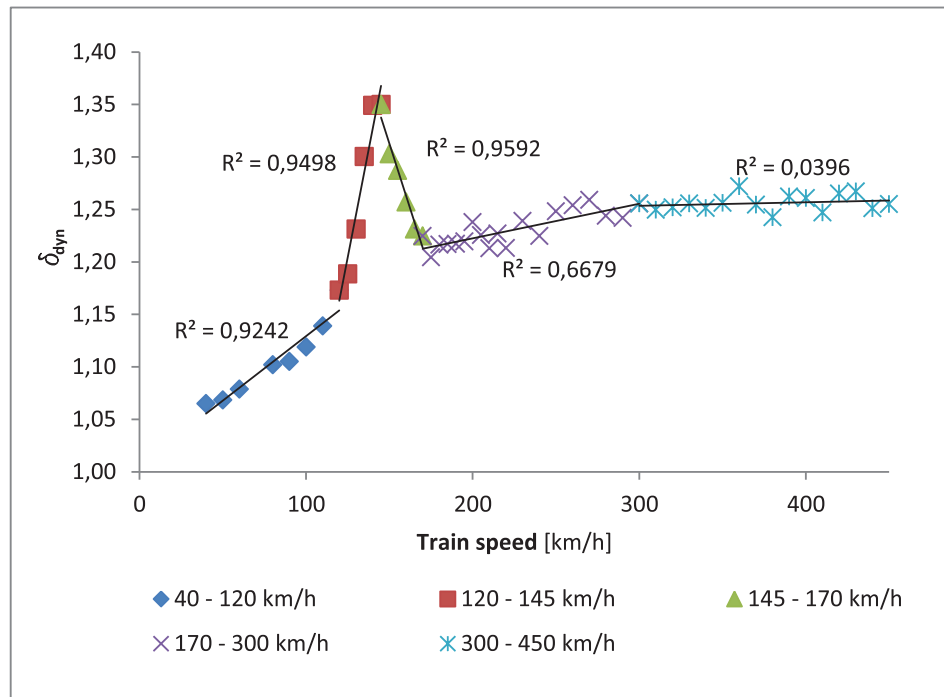


(b)

Figure 12.7 – Scenario 4 (a) Sleeper vertical displacement and (b) dynamic amplification factor in function of train speed



(a)



(b)

Figure 12.8 – Scenario 5: (a) sleeper vertical displacement and (b) dynamic amplification factor in function of train speed

12.2.1 A new explanation of the critical speed

The major source of excitation of the contact force is the sleeper passing frequency. In the three cases shown in last paragraph the sleeper base is 65 cm. Considering this length as the wavelength of the excitation function it can be convenient to compare

resonance frequencies and speed with the relationship:

$$V = 3.6 \cdot 0.65 \cdot f \text{ [km h}^{-1}\text{]}, \quad (12.1)$$

being f the frequencies expressed in Hz. This relation 12.1 connects the velocity of the wheel j with the sleeper passing frequency. Many authors have compared the natural frequencies determined by the analysis of receptance as seen in paragraph 7 with the train speed. Anyway as explained in paragraph 11 train masses and suspension play an important role during the contact with track, modifying its response. Then it results necessary to compare speeds with receptance analysis of the coupled structure, considering both systems: train and substructure. The comparison between receptances of coupled system and the vertical sleeper displacement in function of speed are shown in figures 12.9, 12.10 and 12.11. A surprising results has emerged. The perfect coincidence between critical speed and resonance frequency of the coupled system is shown. It follows that a critical speed cannot be connected uniquely to substructure properties but it is necessary to considerate always the coupled system.

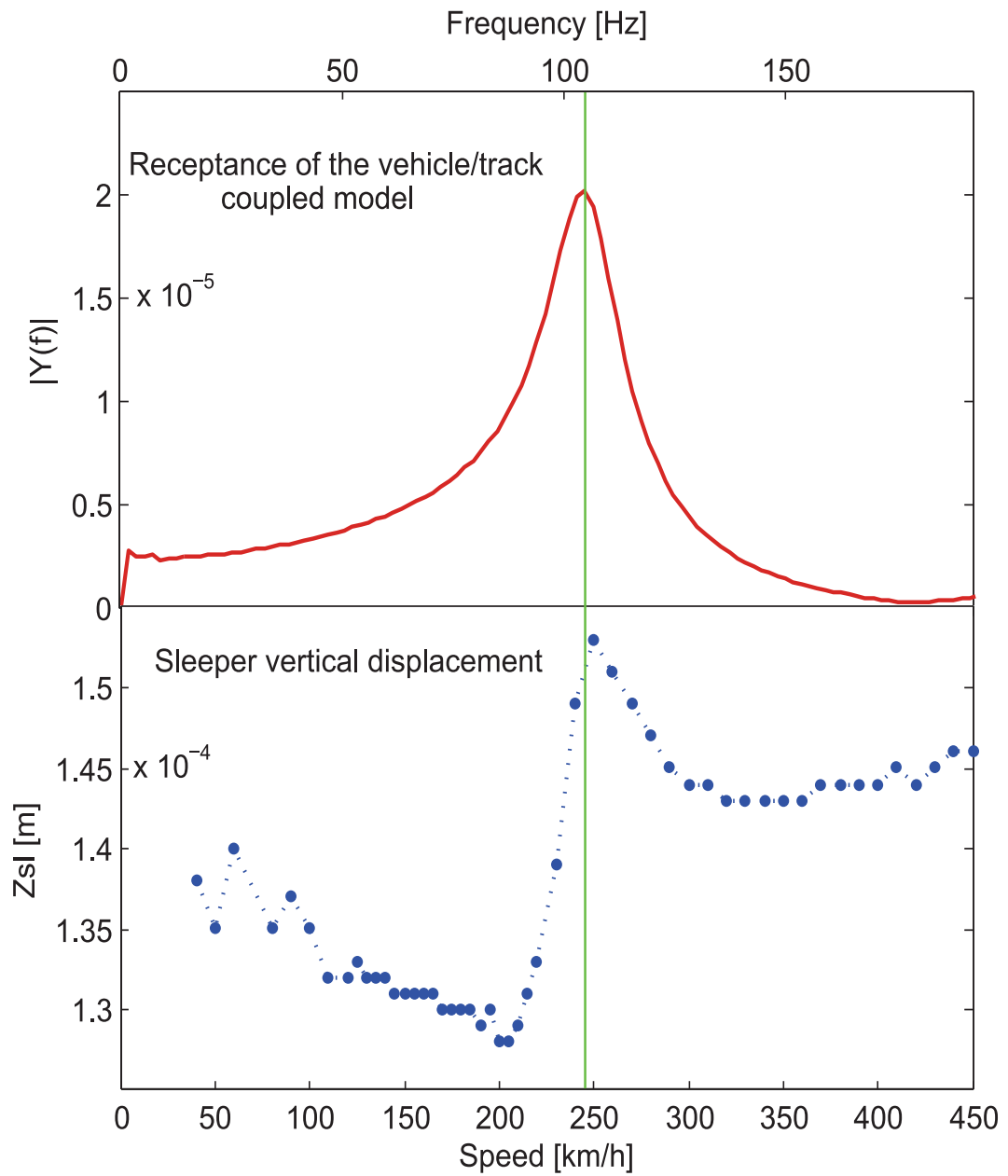


Figure 12.9 – Scenario 3: comparison between critical speed and resonance frequency

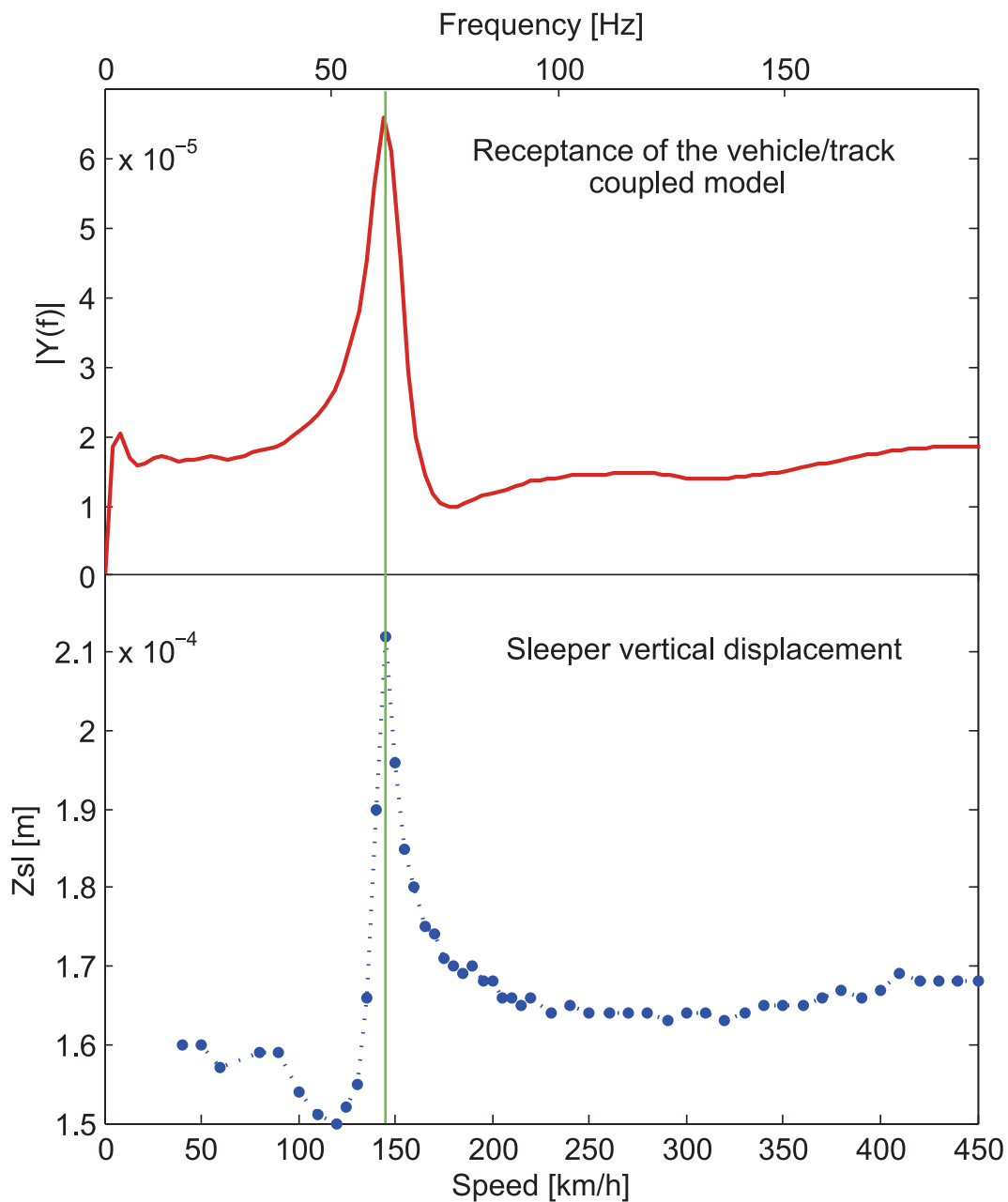


Figure 12.10 – Scenario 4: comparison between critical speed and resonance frequency

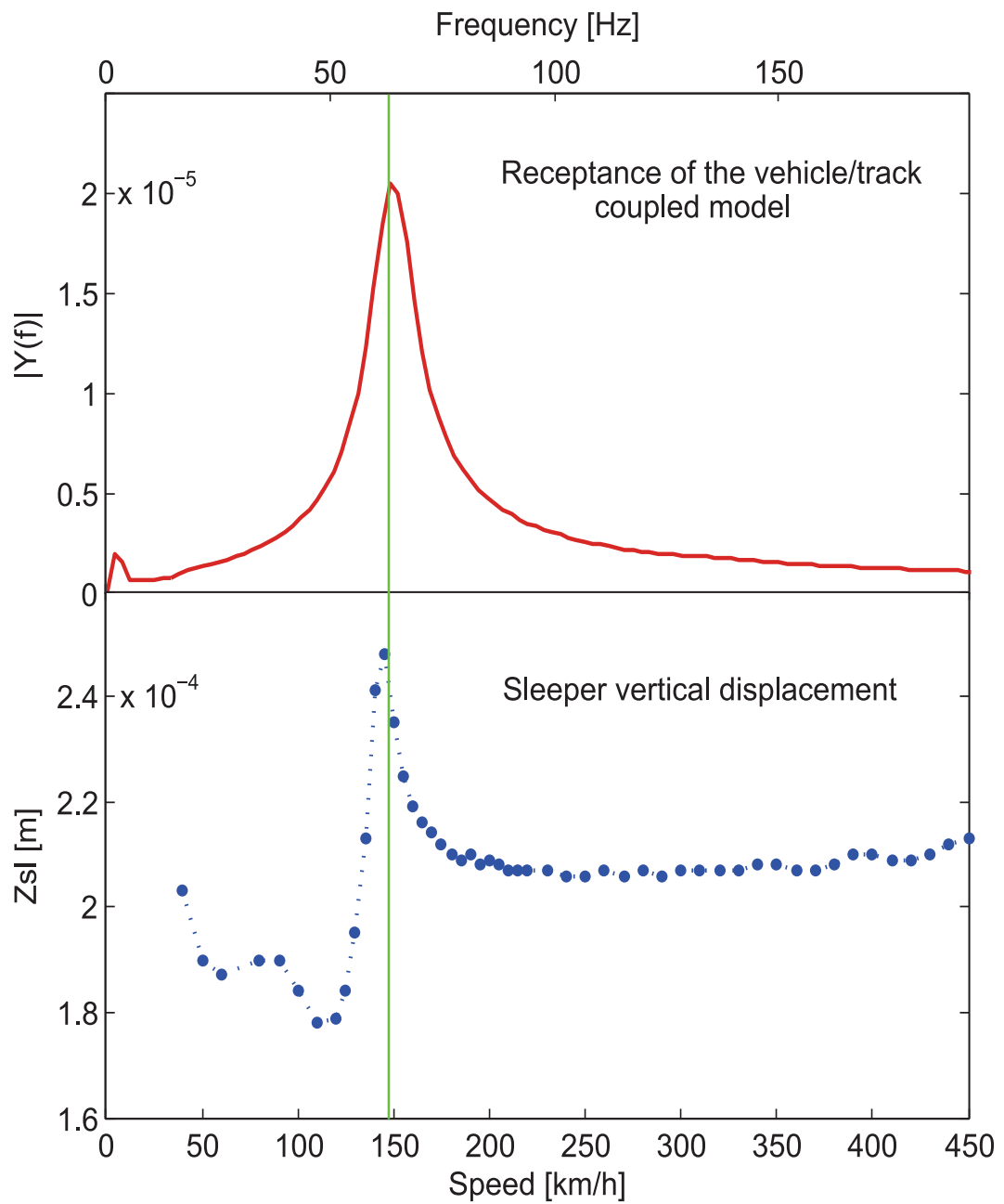


Figure 12.11 – Scenario 5: comparison between critical speed and resonance frequency

CONCLUSIONS AND PERSPECTIVES

The 2D model presented in this work allows to predict contact-forces and vibrations in both vehicle and track components. The validation shows how predictions fit well experimental data. The model of the rail support, here introduced, can be more accurate than past models especially to conduct modal analysis of contact force and vibrations. The connection-area model is strongly recommended to evaluate the track receptance. The connection-point model gives good solutions too, but it results widely incorrect in the pinned-pinned frequency range. In particular it has been found that the connection-point method overestimates the receptance at the pinned-pinned frequency by 402% in the case of midspan excitation. Additionally, in the case of on-sleeper excitation, the receptance is underestimated by the 149%. Varying track and vehicle parameters it has been noticed how the more relevant parameters characterizing the problem of wear are the train mass and the ballast modulus.

The Italian formulation to evaluate the railway toll related to ballast wear results improper. The method proposed in this work is related to the physical phenomenon allowing a more precise evaluation of costs. Moreover the relation between toll, speed and weight needs analysis which can be carried out only by numerical models as the one presented. So, it is recommended to use this software utility to evaluate cost in each different scenario (considering the type of train and railway line).

The analysis of natural frequencies cannot be conducted considering only the track system. When the train passes on the railway the response of system changes substantially modifying the natural frequencies. The influence of the vehicle consists on a drastic reduction of resonance frequency bringing it in the range 50 – 120 Hz.

This fact is directly connected to the phenomenon of train critical speed in the range 100 – 300 km h⁻¹. Indeed the “Mach” phenomenon related to Rayleigh waves, affects a range of speeds too much higher to explain the vibrations peaks measured at lower velocities. In this work an explanation of this phenomenon has been founded. The critical speed in the range 100–300 km,h⁻¹ can be evaluated comparing the sleeper passing frequency to the resonance frequency evaluated by the vehicle/track receptance analysis. The speed correspondent to the sleeper passing frequency, that excites the vehicle/track system at the resonance condition, is the critical value.

As perspectives, the influence of the wheelbase on the critical speed and on the ballast settlement should be studied. Indeed the sleeper passing frequency corresponds to the pass of the wheel axle on a sleeper. Maybe an effect of resonance could be found if the excitation frequency produced by the transit of boogie axis is an entire multiple of the resonance frequency of the vehicle/substructure system. A study could be conducted on the ratio between wheelbase and distance between sleeper too. What is more, the values adopted for the settlement function do not consider the different types of substructure so maybe the parameters of the function should change in function of track features. Furthermore the formulation to evaluate toll costs must be extended. Indeed, in this work, we have shown a method to evaluate the part of costs related to the ballast settlement, in future also the other components of substructure such as sleep-

ers, rail-pads and pantograph must be considered. The objective could be to propose a unique European toll function.

ANNEXES

A

A.1 THE ONE THIRD OCTAVE BAND

The octave band is defined as the frequency range between two frequencies whose ratio is exactly 2 as:

$$\frac{f_2}{f_1} = 2. \quad (\text{A.1})$$

where f_2 and f_1 are respectively the upper and the lower frequency limit of the band as shown in figure A.1. The proportion between band width and central frequency is a constant. In the case of octave band this constant is $\sqrt{2}$ as:

$$\frac{\Delta f}{f_c} = \frac{f_2 - f_1}{f_c} = \sqrt{2} \quad (\text{A.2})$$

A one-third octave band is defined as a frequency band whose upper band-edge frequency (f_3 for the first 1/3 octave band in figure A.1) is the lower band frequency (f_1) times the cube root of two as:

$$\begin{aligned} f_3 &= f_1 \sqrt[3]{2} \\ f_4 &= f_3 \sqrt[3]{2} \\ f_2 &= f_4 \sqrt[3]{2}. \end{aligned} \quad (\text{A.3})$$

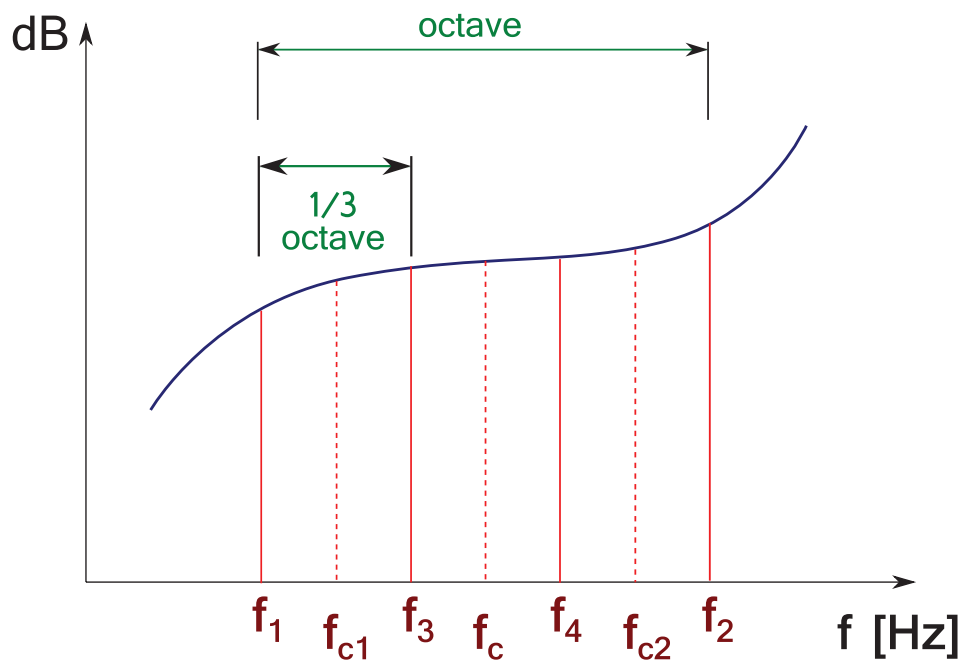


Figure A.1 – Octave band and 1/3 octave band frequencies.

A.2 BALLAST INTERVENTIONS TYPE

In this paragraph two different type of interventions for the ballast are described: the tamping and the stoneblowing. The tamping intervention is used to correct long wavelength. Figure A.2 shows the operating sequence of the tamping machine, where [11]:

- (A) the track and sleeper are in an arbitrary position before tamping begins;
- (B) the track and sleeper are raised by the machine to the target level. As a result, there is an empty space under the sleeper;
- (C) the tamping tines are inserted into the ballast on both sides of the sleeper. This step can cause ballast breakage;
- (D) the tamping tines squeeze the ballast into the empty space under the sleeper. Therefore, the correct position of the rail and sleeper is recovered. This might also cause ballast breakage;
- (E) the tamping tines are lifted from the ballast. They will then move on to tamp around the next sleeper.

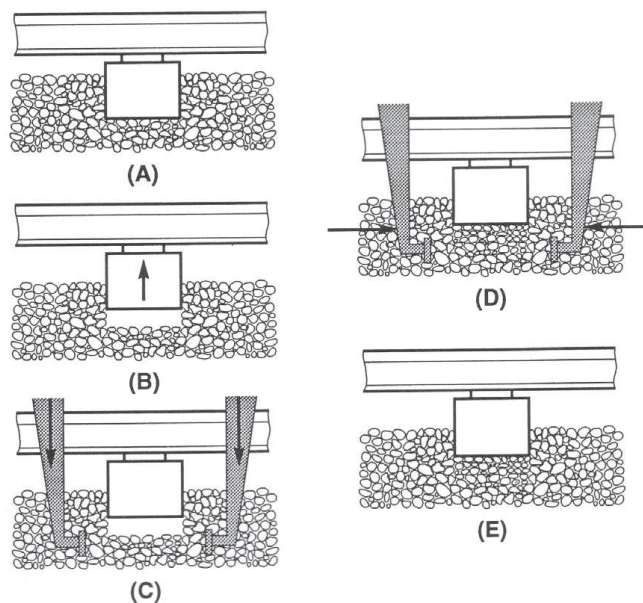


Figure A.2 – Tamping sequence [6]

For short wavelength geometric faults, the stoneblowing maintenance, that is less damaging for the ballast, is more suitable. The operating sequence of stoneblowing maintenance is shown in figure A.3, where:

- (A) the track and sleeper are in an arbitrary position before tamping begins;
- (B) the track and sleeper are raised by the machine to the target level. As a result, there is an empty space under the sleeper;
- (C) the stoneblowing tubes are inserted into the ballast layer;

- (D) a measured quantity of stone is blown by compressed air into the space between the sleeper and the ballast;
- (E) the tubes are withdrawn from the ballast layer;
- (F) the sleeper is lowered onto the top of the blown stone which will be compacted by subsequent traffic.

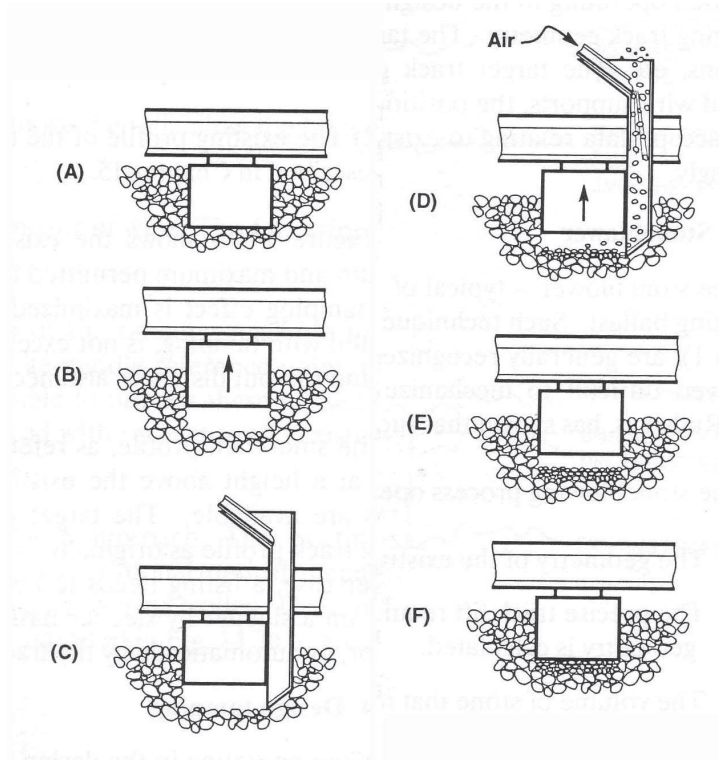


Figure A.3 – Stoneblowing sequence [6]

BIBLIOGRAPHY

- [1] <http://www.rfi.it>.
- [2] <http://www.ansaldobreda.it/>.
- [3] <http://www.heatpoint.nl>.
- [4] <http://www.railway-technology.com/>.
- [5] <http://www.lococarriage.org.uk/x2000.htm>.
- [6] *Track Geotechnology and Substructure Management*. 1994. London: Thomas Telford.
- [7] Dieterman H. A. and Metrikine A. V. Steady-state displacements of a beam on an elastic half-space due to a uniformly moving constant load. *European journal of mechanics. A. Solids*, 16(2):295 – 306, 1997. ISSN 0997-7538.
- [8] Malek Abdelkrim. *Analyse par le calcul des structures du comportement cyclique à long terme des infrastructures de transport*. PhD thesis, Ecole Des Ponts Paristech, Paris, 2001.
- [9] Malek Abdelkrim, Guy Bonnet, and Patrick de Buhan. A computational procedure for predicting the long term residual settlement of a platform induced by repeated traffic loading. *Computers & Geotechnics*, 30(6):463 – 476, 2003. ISSN 0266-352X. doi: 10.1016/S0266-352X(03)00010-7. URL <http://www.sciencedirect.com/science/article/pii/S0266352X03000107>.
- [10] D.R. Ahlbeck, H.C. Meacham, and R.H. Prause. The development of analytical models for railroad track dynamics. *Railroad Track Mechanics & Technology*, 1978. A.D. Kerr (Ed.).
- [11] Bhanitiz Aursudkij. *A Laboratory Study of Railway Ballast Behaviour under Traffic Loading and Tamping Maintenance*. PhD thesis, Nottingham, 2007.
- [12] JB Ayasse and H Chollet. Determination of the wheel rail contact patch in semi-hertzian conditions. *Vehicle System Dynamics*, 43(3):161–172, 2005. doi: 10.1080/00423110412331327193. URL <http://www.tandfonline.com/doi/abs/10.1080/00423110412331327193>.
- [13] émilien Azema, Farhang Radjaï, Robert Peyroux, and Gilles Saussine. Dynamique d’un milieu granulaire soumis à des vibrations horizontales - simulations numériques 3d. 2007. URL [hal:http://hal.archives-ouvertes.fr/hal-00170509/en/](http://hal.archives-ouvertes.fr/hal-00170509/en/).
- [14] V Bodin-Bourgoin, P Tamagny, K Sab, and P-É Gautier. Détermination expérimentale d’une loi de tassement du ballast des voies ferrées soumises à un chargement latéral. *Canadian Geotechnical Journal*, 43(10):1028–1041, 2006. doi: 10.1139/t06-080. URL <http://www.nrcresearchpress.com/doi/abs/10.1139/t06-080>.

- [15] A. Bracciali. Long roughness measurements - analysis and possible protocol. In *8th International Workshop on Railway Noise*, Buxton, UK, 2009. ISBN 9788890437007.
- [16] Yuanqiang Cai, Zhigang Cao, Honglei Sun, and Changjie Xu. Dynamic response of pavements on poroelastic half-space soil medium to a moving traffic load. *Computers & Geotechnics*, 36(1-2):52 – 60, 2009. ISSN 0266-352X. doi: 10.1016/j.compgeo.2008.03.007. URL <http://www.sciencedirect.com/science/article/pii/S0266352X08000426>.
- [17] Alberto Carpinteri. Esercitazioni di laboratorio con il software agli elementi finiti lusas.
- [18] Antonio D’Andrea, Giuseppe Loprencipe, and Elona Xhixha. Vibration induced by rail traffic: Evaluation of attenuation properties in a bituminous sub-ballast layer. *Procedia - Social and Behavioral Sciences*, 53(0):245 – 255, 2012. ISSN 1877-0428. doi: 10.1016/j.sbspro.2012.09.877. URL <http://www.sciencedirect.com/science/article/pii/S187704281204339X>. SIIV-5th International Congress - Sustainability of Road Infrastructures 2012.
- [19] Z. Dimitrovová and J.N. Varandas. Critical velocity of a load moving on a beam with a sudden change of foundation stiffness: Applications to high-speed trains. *Computers & Structures*, 87(19-20):1224 – 1232, 2009. ISSN 0045-7949. doi: 10.1016/j.compstruc.2008.12.005. URL <http://www.sciencedirect.com/science/article/pii/S004579490800268X>. Civil-Comp Special Issue.
- [20] Torbjörn Ekevid, M.X.D. Li, and N.E. Wiberg. Adaptive FEA of wave propagation induced by high-speed trains. *Computers & Structures*, 79(29-30):2693 – 2704, 2001. ISSN 0045-7949. doi: 10.1016/S0045-7949(01)00043-8. URL <http://www.sciencedirect.com/science/article/pii/S0045794901000438>.
- [21] C. Esveld and A.W.M. Kok. Post-doctoral course on high speed track. Technische Universitet Delf (1997).
- [22] M. Fermér and Jens C.O. Nielsen. Vertical interaction between train and track with soft and stiff rail pads – full-scale experiments and theory. volume 209, pages 39 – 47, 1995.
- [23] Riccardo Ferrara, Giovanni Leonardi, and Franck Jourdan. Numerical modelling of train induced vibrations. *Procedia - Social and Behavioral Sciences*, 53(0):155 – 165, 2012. ISSN 1877-0428. doi: 10.1016/j.sbspro.2012.09.869. URL <http://www.sciencedirect.com/science/article/pii/S1877042812043315>. SIIV-5th International Congress - Sustainability of Road Infrastructures 2012.
- [24] Riccardo Ferrara, Giovanni Leonardi, and Franck Jourdan. A contact-area model for rail-pads connections in 2-d simulations: sensitivity analysis of train induced vibrations. *Vehicle System Dynamics*, 2013. in press.
- [25] G. Di Mino, C. Di Liberto, and J. Nigrelli. A FEM model of rail track-ground system to calculate the ground borne vibrations: a case of rail track with wooden sleepers and k-fastenings at Castelvetro. In *Proceeding of Advanced Characterisation of Pavement and Soil Engineering Materials (2007)*, Athens, Greece, 2007. URL <http://hdl.handle.net/10447/34338>.

- [26] P. Galvin and J. Dominguez. Experimental and numerical analyses of vibrations induced by high-speed trains on the Cordoba-Malaga line. *Soil Dynamics and Earthquake Engineering*, 29(4):641 – 657, 2009. ISSN 0267-7261. doi: 10.1016/j.soildyn.2008.07.001. URL <http://www.sciencedirect.com/science/article/pii/S0267726108001231>.
- [27] Nathalie Guerin. *Approche expérimentale et numérique du comportement du ballast des voies ferrées*. PhD thesis, Ecole Des Ponts Paristech, Paris, 2010.
- [28] W.W. Guo, H. Xia, G. De Roeck, and K. Liu. Integral model for train-track-bridge interaction on the sesia viaduct: Dynamic simulation and critical assessment. *Computers & Structures*, 112-113(0):205 – 216, 2012. ISSN 0045-7949. doi: 10.1016/j.compstruc.2012.09.001. URL <http://www.sciencedirect.com/science/article/pii/S0045794912002118>.
- [29] Martin Hiensch, Jens C.O. Nielsen, and Edwin Verheijen. Rail corrugation in the netherlands - measurements and simulations. *Wear*, 253(12):140 – 149, 2002. ISSN 0043-1648. doi: 10.1016/S0043-1648(02)00093-5. URL <http://www.sciencedirect.com/science/article/pii/S0043164802000935>. CM2000 S.I.
- [30] J. Hillig. *Geotechnische Anforderungen an den Eisenbahnunterbau*, 47, Marz 1996. Eisenbahningenieur.
- [31] Hai Huang and Steven Chrismer. Discrete element modeling of ballast settlement under trains moving at critical speeds. *Construction and Building Materials*, 38(0):994 – 1000, 2013. ISSN 0950-0618. doi: 10.1016/j.conbuildmat.2012.09.007. URL <http://www.sciencedirect.com/science/article/pii/S0950061812006691>. 25th Anniversary Session for ACI 228 - Building on the Past for the Future of NDT of Concrete.
- [32] A. Igeland. Rail corrugation growth explained by interaction between track and bogie wheelsets. In *the Institution of Mechanical Engineers*, volume part F 210 (1), pages 11–20, 1996. doi: 10.1243/PIME_PROC_1996_210_322_02.
- [33] Buddhima Indraratna and Wadud Salim. Deformation and degradation mechanics of recycled ballast stabilised with geosynthetics. *Soils and Foundation - Japanese Geotechnical Society*, 43(4):35 – 46, August 2003.
- [34] Simon Iwnick. Manchester benchmarks for rail vehicle simulation. *Vehicle System Dynamics*, 30(3-4):295–313, 1998. doi: 10.1080/00423119808969454. URL <http://www.tandfonline.com/doi/abs/10.1080/00423119808969454>.
- [35] Jens C.O. Nielsen. High-frequency vertical wheel-rail contact forces – Validation of a prediction model by field testing. *Wear*, 265(9-10):1465 – 1471, 2008. ISSN 0043-1648. doi: 10.1016/j.wear.2008.02.038. URL <http://www.sciencedirect.com/science/article/pii/S0043164808001701>.
- [36] Anders Johansson and Jens C.O. Nielsen. Rail corrugation growth - influence of powered wheelsets with wheel tread irregularities. *Wear*, 262(11-12):1296 – 1307, 2007. ISSN 0043-1648. doi: 10.1016/j.wear.2007.01.004. URL <http://www.sciencedirect.com/science/article/pii/S0043164807001664>.
- [37] Jacques Julien. *Pratique de l'analyse de sensibilité: comment évaluer l'impact des entrées aléatoires sur la sortie d'un modèle mathématique*, chapter 71-III. IRMA, Lille, 2011.

- [38] Sakdirat Kaewunruen and Alex M Remennikov. State dependent properties of rail pads. Technical report, 2009. URL <http://search.informit.com.au/documentSummary;dn=721853660071296;res=IELENG>.
- [39] J. J. Kalker. Survey of wheel-rail rolling contact theory. *Vehicle System Dynamics*, 8(4):317–358, 1979. doi: 10.1080/00423117908968610. URL <http://www.tandfonline.com/doi/abs/10.1080/00423117908968610>.
- [40] Anders Karlström. An analytical model for ground vibrations from accelerating trains. *Journal of Sound and Vibration*, 293(3-5):587 – 598, 2006. ISSN 0022-460X. doi: 10.1016/j.jsv.2005.08.038. URL <http://www.sciencedirect.com/science/article/pii/S0022460X05007595>.
- [41] DaeSang Kim and SeongYong Park. Relationship between the subgrade reaction modulus and the strain modulus obtained using a plate loading test. In *9th World Congress on Railway Research*, Lille - France, May 2011.
- [42] KL. Knothe and S.L. Grassie. Modelling of railway track and vehicle/track interaction at high frequencies. *Vehicle System Dynamics*, 22(3-4):209–262, 1993. doi: 10.1080/00423119308969027. URL <http://www.tandfonline.com/doi/abs/10.1080/00423119308969027>.
- [43] Victor V. Krylov. Generation of ground vibrations by superfast trains. *Applied Acoustics*, 44(2):149 – 164, 1995. ISSN 0003-682X. doi: 10.1016/0003-682X(95)91370-I. URL <http://www.sciencedirect.com/science/article/pii/0003682X9591370I>.
- [44] G. Kumaran, Devdas Menon, and K. Krishnan Nair. Dynamic studies of railtrack sleepers in a track structure system. *Journal of Sound and Vibration*, 268(3):485 – 501, 2003. ISSN 0022-460X. doi: 10.1016/S0022-460X(02)01581-X. URL <http://www.sciencedirect.com/science/article/pii/S0022460X0201581X>.
- [45] X. Lei and N.A. Noda. Analyses of dynamic response of vehicle and track coupling system with random irregularity of track vertical profile. *Journal of Sound and Vibration*, 258(1):147 – 165, 2002. ISSN 0022-460X. doi: DOI:10.1006/jsvi.2002.5107. URL <http://www.sciencedirect.com/science/article/B6WM3-473FKDP-N/2/73c07bdb03b0b3805a89c9d03b5ef0fa>.
- [46] M. LIEB and B. SUDRET. A fast algorithm for soil dynamics calculation by wavelet decomposition. *Archive of Applied Mechanics*, 68:147 – 157, 1998.
- [47] F. Lu, D. Kennedy, F.W. Williams, and J.H. Lin. Symplectic analysis of vertical random vibration for coupled vehicle-track systems. *Journal of Sound and Vibration*, 317(1-2):236 – 249, 2008. ISSN 0022-460X. doi: 10.1016/j.jsv.2008.03.004. URL <http://www.sciencedirect.com/science/article/pii/S0022460X08002149>.
- [48] Margarida Machado, Pedro Moreira, Paulo Flores, and Hamid M. Lankarani. Compliant contact force models in multibody dynamics: Evolution of the hertz contact theory. *Mechanism and Machine Theory*, 53(0):99 – 121, 2012. ISSN 0094-114X. doi: 10.1016/j.mechmachtheory.2012.02.010. URL <http://www.sciencedirect.com/science/article/pii/S0094114X1200047X>.
- [49] C. Madshus and A.M. Kaynia. High-speed railway lines on soft ground: dynamic behaviour at critical train speed. *Journal of Sound and Vibration*, 231(3):689

- 701, 2000. ISSN 0022-460X. doi: 10.1006/jsvi.1999.2647. URL <http://www.sciencedirect.com/science/article/pii/S0022460X99926470>.
- [50] Leszek Majkut. Free and forced vibrations of timoshenko beams described by single difference equation. *Journal of theoretical and applied mechanics*, 47(1):193 – 210, 2009. ISSN 1429-2955. URL <http://www.ptmts.org.pl/article.xsl?vol=47&no=1&page=193>.
- [51] Traian Mazilu. Prediction of the interaction between a simple moving vehicle and an infinite periodically supported rail — green’s functions approach. *Vehicle System Dynamics*, 48(9):1021–1042, 2010. doi: 10.1080/00423110903248694. URL <http://www.tandfonline.com/doi/abs/10.1080/00423110903248694>.
- [52] Carolina Meier-Hirmer. Optimisation de la maintenance de la géométrie de la voie, april 2009. SNCF - Direction de l’infrastructure.
- [53] FC. De Nie. Undulation of railway embankments on soft sub-soil during passing of trains. In *2nd conference on soil mechanics and foundation*, volume II, pages 1–8, May 1948.
- [54] Jens C.O. Nielsen and A. Igeland. Vertical dynamic interaction between train and track influence of wheel and track imperfections. *Journal of Sound and Vibration*, 187(5):825 – 839, 1995. ISSN 0022-460X. doi: 10.1006/jsvi.1995.0566. URL <http://www.sciencedirect.com/science/article/pii/S0022460X85705664>.
- [55] J. O’Brien and D.C. Rizos. A 3d bem-fem methodology for simulation of high speed train induced vibrations. *Soil Dynamics and Earthquake Engineering*, 25(4):289 – 301, 2005. ISSN 0267-7261. doi: 10.1016/j.soildyn.2005.02.005. URL <http://www.sciencedirect.com/science/article/pii/S0267726105000175>.
- [56] Chiara Paderno. *Comportement du ballast sous l’action du bourrage et du trafic ferroviaire*. PhD thesis, ENAC, Lausanne, 2010. URL <http://library.epfl.ch/theses/?nr=4697>.
- [57] B. Picoux and D. Le Houédec. Diagnosis and prediction of vibration from railway trains. *Soil Dynamics and Earthquake Engineering*, 25(12):905 – 921, 2005. ISSN 0267-7261. doi: 10.1016/j.soildyn.2005.07.002. URL <http://www.sciencedirect.com/science/article/pii/S0267726105001272>.
- [58] J. Pombo, J. Ambrósio, M. Pereira, R. Verardi, C. Ariaudo, and N. Kuka. Influence of track conditions and wheel wear state on the loads imposed on the infrastructure by railway vehicles. *Computers & Structures*, 89(21-22):1882 – 1894, 2011. ISSN 0045-7949. doi: 10.1016/j.compstruc.2011.05.009. URL <http://www.sciencedirect.com/science/article/pii/S0045794911001519>. Civil-Comp.
- [59] Joao Carlos Elói Pombo and Jorge Alberto Cadete Ambrósio. A multibody methodology for railway dynamics applications. Technical report, Instituto Superior Técnico, Av. Rovisco Pais,1 1049-001 Lisboa, Portugal, 2004.
- [60] João Pombo, Jorge Ambrósio, and Miguel Silva. A new wheelrail contact model for railway dynamics. *Vehicle System Dynamics*, 45(2):165–189, 2007. doi: 10.1080/00423110600996017. URL <http://www.tandfonline.com/doi/abs/10.1080/00423110600996017>.

- [61] E. Rehfeld. *Untergrundbeschaffenheit*. 46:258?64, 1994. Eisenbahningenieur.
- [62] RFI. *Specification (technical standard)*, 2011.
- [63] L. Ricci, V.H. Nguyen, K. Sab, D. Duhamel, and L. Schmitt. Dynamic behaviour of ballasted railway tracks: A discrete/continuous approach. *Computers & Structures*, 83(28-30):2282 – 2292, 2005. ISSN 0045-7949. doi: 10.1016/j.compstruc.2005.03.035. URL <http://www.sciencedirect.com/science/article/pii/S004579490500252X>. A Selection of Papers from Civil-Comp 2003 and AICivil-Comp 2003.
- [64] Federico Rossi and Andrea Nicolini. A simple model to predict train-induced vibration: theoretical formulation and experimental validation. *Environmental Impact Assessment Review*, 23(3):305 – 322, 2003. ISSN 0195-9255. doi: 10.1016/S0195-9255(03)00005-2. URL <http://www.sciencedirect.com/science/article/pii/S0195925503000052>.
- [65] Pablo Salvador, Julia Real, Clara Zamorano, and Antonio Villanueva. A procedure for the evaluation of vibrations induced by the passing of a train and its application to real railway traffic. *Mathematical and Computer Modelling*, 53(1-2):42 – 54, 2011. ISSN 0895-7177. doi: 10.1016/j.mcm.2010.07.016. URL <http://www.sciencedirect.com/science/article/pii/S089571771000347X>.
- [66] Sato. Theoretical analyses on vibration of ballasted track. *QR of RTRI*, (29):30 – 32, 1988.
- [67] G. Saussine, C. Cholet, P.E. Gautier, F. Dubois, C. Bohatier, and J.J. Moreau. Modelling ballast behaviour under dynamic loading. part 1: A 2d polygonal discrete element method approach. *Computer Methods in Applied Mechanics and Engineering*, 195(19-22):2841 – 2859, 2006. ISSN 0045-7825. doi: 10.1016/j.cma.2005.07.006. URL <http://www.sciencedirect.com/science/article/pii/S0045782505002823>.
- [68] Gilles Saussine. *Contribution à la modélisation de granulats tridimensionnels: application au ballast*. PhD thesis, LMGC - Laboratoire de mécanique et génie civil, Montpellier, 2004.
- [69] M. Sunaga, E. Sekine, and T. Ito. Vibration behaviors of roadbed on soft grounds under train load. *Quart Rep Railway Tech Res Inst*, 31(1):29 – 35, 1990.
- [70] M. Sunaga, E. Sekine, and T. Ito. Vibration behaviors of roadbed on soft grounds under train load. *Quart Rep Railway Tech Res Inst*, 31(1):29?35, 1990.
- [71] M Tanabe, H Wakui, N Matsumoto, H Okuda, M Sogabe, and S Komiya. Computational model of a shinkansen train running on the railway structure and the industrial applications. *Journal of Materials Processing Technology*, 140(1-3):705 – 710, 2003. ISSN 0924-0136. doi: 10.1016/S0924-0136(03)00777-5. URL <http://www.sciencedirect.com/science/article/pii/S0924013603007775>. Proceedings of the 6th Asia Pacific Conference on materials Processing.
- [72] Bo Torstenfelt. *Finite Elements - An Introduction to Elasticity and Heat Transfer Application*.

- [73] A.V. Vostroukhov and A.V. Metrikine. Periodically supported beam on a visco-elastic layer as a model for dynamic analysis of a high-speed railway track. *International Journal of Solids and Structures*, 40(21):5723 – 5752, 2003. ISSN 0020-7683. doi: 10.1016/S0020-7683(03)00311-1. URL <http://www.sciencedirect.com/science/article/pii/S0020768303003111>.
- [74] Krylov V.V. Effects of track properties on ground vibrations generated by high-speed trains. *Acta Acustica united with Acustica*, 84(1):78 – 90, 1998.
- [75] Krylov V.V. Ground vibration boom from high-speed trains: prediction and reality. *Acoustics Bulletin*, 23(4):15 – 22, 1998.
- [76] A.R.M. Wolfert, H.A. Dieterman, and A.V. Metrikine. Passing through the “elastic wave barrier” by a load moving along a waveguide. *Journal of Sound and Vibration*, 203(4):597 – 606, 1997. ISSN 0022-460X. doi: 10.1006/jsvi.1996.0866. URL <http://www.sciencedirect.com/science/article/pii/S0022460X96908664>.
- [77] T.X. WU and D.J. THOMPSON. A hybrid model for the noise generation due to railway wheel flats. *Journal of Sound and Vibration*, 251(1):115 – 139, 2002. ISSN 0022-460X. doi: 10.1006/jsvi.2001.3980. URL <http://www.sciencedirect.com/science/article/pii/S0022460X0193980X>.
- [78] T.X. Wu and D.J. Thompson. An investigation into rail corrugation due to micro-slip under multiple wheel/rail interactions. *Wear*, 258(7-8):1115 – 1125, 2005. ISSN 0043-1648. doi: 10.1016/j.wear.2004.03.060. URL <http://www.sciencedirect.com/science/article/pii/S0043164804003217>. Contact Mechanics and Wear of Rail/Wheel Systems.
- [79] Y.L. Xu and Q.S. Ding. Interaction of railway vehicles with track in cross-winds. *Journal of Fluids and Structures*, 22(3):295 – 314, 2006. ISSN 0889-9746. doi: 10.1016/j.jfluidstructs.2005.11.003. URL <http://www.sciencedirect.com/science/article/pii/S0889974605002318>.
- [80] Y.Q. Sun and M. Dhanasekar. A dynamic model for the vertical interaction of the rail track and wagon system. *International Journal of Solids and Structures*, 39(5):1337 – 1359, 2002. ISSN 0020-7683. doi: DOI:10.1016/S0020-7683(01)00224-4. URL <http://www.sciencedirect.com/science/article/B6VJS-44CN0YR-3/2/f89204c2d15b2b5ec14792cfd0a07196>.
- [81] W. Zhai and Z. Cai. Dynamic interaction between a lumped mass vehicle and a discretely supported continuous rail track. *Computers & Structures*, 63(5):987 – 997, 1997. ISSN 0045-7949. doi: 10.1016/S0045-7949(96)00401-4. URL <http://www.sciencedirect.com/science/article/pii/S0045794996004014>.
- [82] W.M. Zhai, K.Y. Wang, and J.H. Lin. Modelling and experiment of railway ballast vibrations. *Journal of Sound and Vibration*, 270(4-5):673 – 683, 2004. ISSN 0022-460X. doi: 10.1016/S0022-460X(03)00186-X. URL <http://www.sciencedirect.com/science/article/pii/S0022460X0300186X>.
- [83] J. Zhang, Q. Gao, S.J. Tan, and W.X. Zhong. A precise integration method for solving coupled vehicle-track dynamics with nonlinear wheel-rail contact. *Journal of Sound and Vibration*, 331(21):4763 – 4773, 2012. ISSN 0022-460X. doi: 10.1016/j.jsv.2012.05.033. URL <http://www.sciencedirect.com/science/article/pii/S0022460X1200418X>.